DISSERTATION

# ENHANCED SURFACE FUNCTIONALITY VIA PLASMA MODIFICATION AND PLASMA DEPOSITION TECHNIQUES TO CREATE MORE BIOLOGICALLY RELEVANT MATERIALS

Submitted by

Jeffrey C. Shearer

Department of Chemistry

In partial fulfillment of the requirements

For the Degree of Doctor of Philosophy

Colorado State University

Fort Collins, Colorado

Summer 2013

Doctoral Committee:

Advisor: Ellen R. Fisher

Charles Henry
Grzegorz Szamel
Travis Bailey
Kristen Buchanan

ABSTRACT

ENHANCED SURFACE FUNCTIONALITY VIA PLASMA MODIFICATION AND DEPOSITION TECHNIQUES TO CREATE MORE BIOLOGICALLY RELEVANT MATERIALS

Functionalizing nanoparticles and other unusually shaped substrates to create more biologically relevant materials has become central to a wide range of research programs. One of the primary challenges in this field is creating highly functionalized surfaces without modifying the underlying bulk material. Traditional wet chemistry techniques utilize thin film depositions to functionalize nanomaterials with oxygen and nitrogen containing functional groups, such as –OH and $–NH_x$. These functional groups can serve to create surfaces that are amenable to cell adhesion or can act as reactive groups for further attachment of larger structures, such as macromolecules or antiviral agents. Additional layers, such as $SiO_2$, are often added between the nanomaterial and the functionalized coating to act as a barrier films, adhesion layers, and to increase overall hydrophilicity. However, some wet chemistry techniques can damage the bulk material during processing.

This dissertation examines the use of plasma processing as an alternative method for producing these highly functionalized surfaces on nanoparticles and polymeric scaffolds through the use of plasma modification and plasma enhanced chemical vapor deposition techniques. Specifically, this dissertation will focus on **(1)** plasma deposition of $SiO_2$ barrier films on nanoparticle substrates; **(2)** surface functionalization of amine and alcohol groups through (a) plasma co-polymerization and (b) plasma modification; and **(3)** the design and construction of plasma hardware to facilitate plasma processing of nanoparticles and polymeric scaffolds.

The body of work presented herein first examines the fabrication of composite nanoparticles by plasma processing. $SiO_xC_y$ and hexylamine films were coated onto $TiO_2$ nanoparticles to demonstrate enhanced water dispersion properties. Continuous wave and pulsed allyl alcohol plasmas were used to produce highly functionalized $Fe_2O_3$ supported nanoparticles. Specifically, film composition was correlated to gas-phase excited state species and the pulsing duty cycle to better understand the mechanisms of allyl alcohol deposition in our plasma systems.

While these studies specifically examined supported nanoparticle substrates, some applications might require the complete functionalization of the entire nanoparticle surface. To overcome this challenge, a rotating drum plasma reactor was designed as a method for functionalizing the surface of individual $Fe_2O_3$ nanoparticles. Specifically, data show how the rotating motion of the reactor is beneficial for increasing the alcohol surface functionality of the nanoparticles when treated with pulsed allyl alcohol plasmas.

Plasma copolymerization was used to deposit films rich in both oxygen and nitrogen containing functional groups using allyl alcohol and allyl amine plasma systems. Functional group retention and surface wettability was maximized under pulsed plasma conditions, and films produced under pulsed plasma conditions did not exhibit hydrophobic recovery or experience loss of nitrogen as the films aged.

Plasma surface modification with $N_2/H_2O$ and $NH_3/H_2O$, and plasma deposition with allyl alcohol and allyl amine, were used to increase the wettability of poly(caprolactone) scaffolds while simultaneously implanting functional groups onto the scaffold surface and into the scaffold core. While plasma deposition methods did not modify the internal core of the scaffold as much as modification methods, it afforded the ability to have higher water absorption

rates after a three week aging period. Additionally, cell viability studies were conducted with $N_2/H_2O$ plasma treated scaffolds and showed enhanced cell growth on plasma treated scaffolds over non plasma-treated scaffolds.

TABLE OF CONTENTS

LIST OF TABLES

LIST OF FIGURES

# CHAPTER 1

# INTRODUCTION

This chapter provides an overview of the fundamental chemistry of plasma deposition and plasma modification strategies as they relate to the production of biologically relevant surfaces. A discussion of how plasma parameters affect deposition mechanisms is followed by a detailed analysis of how pulsed plasma systems aid in functional group retention.

## 1.1 Motivation of Research

The fabrication of highly functionalized materials using industrially compatible techniques has become an extremely active area of research. These materials have a wide range of potential applications, including fuel cell fabrication, biological labeling, targeted drug delivery, and cell growth.[1-5] As it is difficult to find materials that meet all of the suitable requirements for a particular application, one strategy is to surface-modify materials with suitable bulk properties to improve their surface characteristics.[1] For example, biomedical impants can be surface modified with thin polymeric coatings to direct specific cellular responses.[6] Furthermore, oxygen and nitrogen containing functional groups have been shown to increase the wettability and cell adhesion properties of biocompatible polymers and other biologically relevant materials.[7-11]

Several methods have been employed to create thin, biologically relevant coatings, including chemical vapor deposition (CVD)[5], spray pyrolysis[6], and plasma-enhanced CVD (PECVD).[7] Plasma processing is a popular method for surface modification and thin film deposition because of its ability to create uniform, pinhole free films on uniquely shaped

materials through low temperature, solution-free processing. Moreover, an assortment of processing parameters can be readily adjusted to tailor the surface composition and deposition characteristics from a wide selection of starting materials. This flexibility makes plasma processing ideal for implanting specific functional groups onto the surface of materials through deposition and surface modification techniques.

Although plasma processing offers many advantages to biomaterial surface modification, it is well known for being highly sensitive to changes in processing conditions, such as gas flow rate, system pressure, substrate temperature, monomer selection, input power, and substrate type.[12-15] Although general characteristics for various types of plasmas have been well summarized in the literature,[12,14,15] elucidating specific characteristics (film composition, deposition rates, surface roughness, etc.) of these complex processes is not trivial and must be studied on a system-by-system basis. Thus, this dissertation will focus on the plasma processing of various surfaces as a method for enhancing surface functionality, thereby creating more biologically relevant materials.

## 1.2 Plasma Fundamentals

In general, plasmas are formed when an electric field is applied to a volume of gas, causing the acceleration of electrons and release of energy in the form of ionization, excitation, and other collision processes.[16] This results in a partially ionized gas consisting of charged and neutral particles including ions, neutrals, radicals, electrons, and photons.[14,15] These active gas-phase species can undergo a host of gas-phase and surface reactions to create highly functionalized surfaces.[1,14,15,17-21] Two categories of plasmas used in this dissertation. Capacitively-coupled plasmas (CCPs) are produced when the electric field is generated between

two parallel plate electrodes. Inductively-coupled plasmas (ICPs) are produced when passing an electrical current through a conductive coil located outside of the plasma reactor induces the electric field. Most of the plasmas described in this dissertation are ICPs produced by applying an electric field to a hollow glass reactor tube using an RF voltage power source, as described in Section 2.1.

### 1.2.1 Plasma Deposition

During plasma deposition (or plasma polymerization), reactive gas species (*i.e.,* ions, neutrals, radicals) can diffuse to a surface, where they can be adsorbed and diffuse across the surface and/or undergo surface reactions. Film formation occurs when nonvolatile species polymerize on the surface. Volatile products are typically desorbed and pumped out of the system.[14] In this dissertation, three primary plasma deposition systems are used to create functionalized surfaces: (1) hexamethyldisiloxane (HMDSO)/$O_2$, (2) allyl alcohol (allylOH), and (3) allyl amine (allylNH).

In HMDSO/$O_2$ plasmas, O atoms can react with hydrocarbon moieties that are produced during dissociation of the HMDSO precursor. The resultant CO molecules are stable enough to remain in the gas phase, and they are pumped out of the system and not incorporated into the film.[22] Thus, increasing concentrations of $O_2$ in the plasma gas feed decreases hydrocarbon incorporation in the deposited films, creating more $SiO_2$-like films.

Plasma treatment with allylOH typically focuses on the ability to deposit films that retain the structure of the allylOH monomer, thus depositing films with a high degree of alcohol functionality.[23-28] There are several mechanisms by which allylOH can plasma polymerize. Scheme 2.1 below depicts general polymerization mechanisms proposed by Watkins for the plasma polymerization of allyl alcohol.[24]

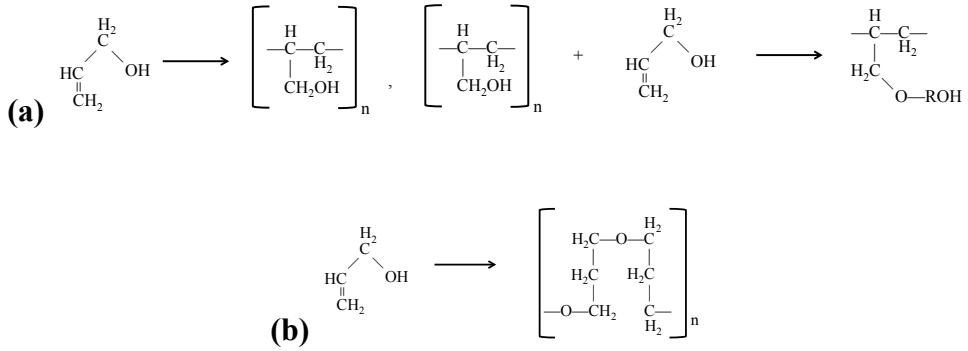

**Scheme 2.1**

Scheme 2.1a shows the formation of films that have a high concentration of –OH functional groups. In contrast, Scheme 2.1b depicts films high in ether functionality. Short et al. have reported more detailed mechanisms in the literature,[25,26] suggesting that ion-molecule reactions are the primary mechanism by which the general reactions in Scheme 2.1 occur.

As with allylOH plasma polymerization systems, allylNH deposition typically focuses on retaining as much of the amine structure from the allylNH monomer as possible,[27,29-31] producing the idealized film depicted below.

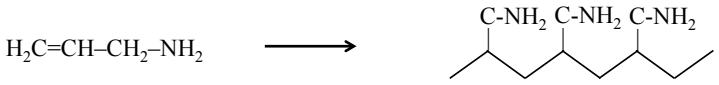

**Scheme 2.2**

However, allylNH undergoes virtually immediate oxidation upon exposure to the atmosphere, creating a film that also has alcohol functional groups. This phenomenon has been thoroughly described in the literature,[27,29,32] and is depicted in Scheme 2.3 below.

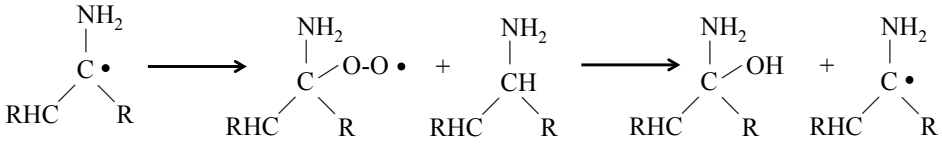

**Scheme 2.3**

It should be noted that this rapid oxidation causes variation in film compositions reported for allylNH films in the literature. As such, plasma polymerizing allylNH on novel materials must be studied as a function of the films' age as to elucidate contributions due to aging.

### 1.2.2 Plasma Surface Modification

The term plasma surface modification describes the ability to alter the properties of surfaces without the deposition of a thin film. Typically, plasma surface modification is characterized by the term surface activation; the energetic species contained within plasma collide with a surface, causing surface covalent bonds to break and surface radicals to form. The radicals on the surface can then react with active gas-phase plasma species to form functional groups at the surface.[15] For example, oxygen[15] and water vapor[33] plasmas can oxygenate surfaces and nitrogen and ammonia plasmas[34] can nitrogenate surfaces without inducing film formation. These processes can ultimately induce hydrophilicity, improve adhesion characteristics, and increase functional group density of the surface of the treated material.[15] Similar surface activation processes were used to graft N and O containing functional groups onto polymeric scaffold surfaces in Chapters 7 and 8.

## 1.3 Effects of Plasma Parameters

As alluded to in previous sections, the plasma parameters control the specific modification characteristics of the surface or the characteristics of the deposited films. Substrate temperature, system pressure, gas flow rates, reactor design, input power, and pulsing frequency are a few of a long list of parameters that can affect plasma processes. Various projects described in this dissertation evaluated the effects of substrate temperature, reactor design, feed

gas composition, substrate location, and plasma pulsing as optimization parameters for various plasma modification and polymerization systems.

One such parameter that is used in much of this dissertation is plasma pulsing. As such, it is necessary to detail how pulsing a plasma can have unique advantages in plasma processing. Typically, plasma processes are operated with the plasma ignited during the entire duration of the plasma treatment. This is referred to as operating in a continuous wave (CW) mode. In contrast, pulsed plasma processing occurs when the plasma is cycled "on" and "off" at a frequency defined as duty cycle (d.c.), where $\text{d.c. } (\%) = \frac{\text{time}_{on}}{\text{time}_{on} + \text{time}_{off}} \cdot 100$. One of the limitations of CW plasma is that films deposited in these plasmas can be highly crossed-linked with a lower degree of surface functionality.[13] However, biomaterial-related fields have an acute interest in highly-functionalized, less cross-linked films. Pulsed plasma can therefore be used to produce these biologically-relevant surfaces.

Some of the most widespread work done in this area has been by Yasuda and coworkers.[12,35] They introduced the variable W/FM, where W, F, and M are input power, monomer flow rate, and molecular mass, respectively. Lower values of W/FM tend to correlate to less monomer fragmentation during plasma processing, which arises from the direct dependence on input power. Therefore, by lowering the input power, one can achieve less monomer fragmentation is a given plasma system. Plasma pulsing can effectively achieve a lower input power due the equivalent average power $\langle P \rangle$ delivered to the system. $\langle P \rangle$ can be defined as d.c. multiplied by the peak power. From this equation, it can be deduced that lowering the plasma duty cycle lowers the effective amount of energy introduced to the plasma process, thereby reducing monomer fragmentation and increasing the functional groups in the

deposited film.[13] As such, pulsed plasma deposition was used extensively in this dissertation to enhance the functional groups deposited on biomaterial-relevant surfaces.

## 1.4 Overview of Research

This dissertation is focused on plasma deposition and modification strategies for more biologically relevant surfaces. This dissertation begins with the modification of $TiO_2$ nanoparticles to increase their suspension properties in water. Nanoparticles were coated with $SiO_xC_y$ and $SiO_2$. Emphasis is placed on the ability to conformally coat the nanoparticle substrates without compromising the original size and shape of the particles. To demonstrate the feasibility of this process being scaled to other systems, $TiO_2$ supported nanoparticle substrates were processed in hexylamine plasmas to create conformal, N-rich films. All particles were analyzed to evaluate the efficacy of plasma processing on the particles' suspension characteristics in water. Plasma treated particles stayed suspended in solution longer than untreated particles, with those coated with inorganic films falling out of solution at an increased rate compared to particles coated with more organic-like films. Furthermore, substrate temperature was evaluated as a mechanism for controlling film composition during deposition processes with HMDSO/$O_2$ plasmas.

Chapter 4 extends this deposition model to plasma polymerized (*pp*) allylOH films deposited onto $Fe_2O_3$ nanoparticles. Specifically, pulsed plasma systems were used to deposit thin films with a high retention of the alcohol functionality found in the parent monomer. Gas-phase studies correlated excited state gas species to the functional groups observed in the deposited films.

Although the supported nanoparticle substrates used in Chapters 3 and 4 are used across many industries, it is important to explore ways to functionalize individual nanoparticles. Chapter 5 examines a rotating drum plasma reactor system designed to individually coat nanoparticles. The reactor was used to deposit allylOH films onto free, unsupported $Fe_2O_3$ nanoparticles. Comparisons between rotating and nonrotating Si wafers, supported $Fe_2O_3$ nanoparticle substrates, and free nanoparticle substrates demonstrate that the rotating motion of the reactor produces films with identical properties as those deposited in static reactor systems. Furthermore, OH functional groups are implanted more effectively on free nanoparticles in the rotating reactor than in a static reactor. All samples were treated under CW and pulsed plasma conditions to demonstrate the efficacy of the reactor to perform under various operational modes.

Whereas Chapters 3, 4, and 5 discuss the single-monomer plasma polymerization of thin films, Chapter 6 discusses the co-polymerization of allylOH and allylNH. Plasma copolymerization has become more popular in recent years, coinciding with the growing need for biologically-relevant surfaces with multiple types of functional groups. [1,36] The co-polymerization of allylOH and allylNH yields thin films with various amounts of nitrogen- and oxygen-containing functional groups. To our knowledge, this copolymerization system has not been previously reported in the literature; therefore, fundamental surface analyses were performed to gain insight into how the mixing of these monomers affect film composition. Films were deposited using both CW and pulsed plasmas, and surface analysis was conducted longitudinally to monitor film aging.

In recent years, surface modification of polymeric scaffolds has become relevant in areas such as tissue engineering.[1,9,37,38] Chapters 7 and 8 discuss the functionalization of poly(ε-caprolactone) scaffolds under various plasma modification and plasma deposition systems.

Specifically, $N_2/H_2O$ plasmas were modified in a CCP translating electrode plasma reactor at the University of Bari. The amount of functional groups on the scaffold surface increased from untreated scaffolds, and nitrogen was incorporated throughout the scaffold network. Furthermore, the natively hydrophobic scaffolds became immediately wettable upon plasma treatment. Additionally, plasma treated scaffolds had enhanced human Saos-2 osteoblast cell growth over that of untreated scaffolds.

The scaffold modification studies from the University of Bari were extended to the plasma reactor systems at Colorado State. The rotating drum reactor was used to modify scaffolds in $NH_3/H_2O$ plasmas and deposit films onto scaffolds in allylOH/allylNH copolymerization systems. Scaffolds modified in $NH_3/H_2O$ plasmas were immediately wettable, and retained their absorption properties over a 1 month aging period. Scaffolds treated in allylOH/allylNH plasmas were slightly less wettable than those treated in $NH_3/H_2O$ plasmas, but retained higher absorption rates after they aged.

Clearly, plasma processing affords a wide array of research opportunities related to biomaterial processing. Chapter 9 summarizes this dissertation and suggests future areas of research that would complement this body of work. Overall, the work presented here profiles various methods for functionalizing the surface of biologically-relevant materials. An emphasis is placed on pulsed plasma depositions and the design of novel plasma instrumentation that affords the ability to treat the entire surface area of these materials. Aspects of this work have laid the groundwork for a new avenue of biomaterials-related projects.

REFERENCES


[1] T. Jacobs, R. Morent, N. Geyter, P. Dubruel, and C. Leys, Plasma Chem Plasma Process **32**, 1039 (2012).

[2] M. W. Hooker, K. S. Kano, and M. W. Stewart, IEEE Trans. Appl. Supercond. **17**, 1521 (n.d.).

[3] V. V. Kuznetsov, A. A. Kalinkina, and T. V. Pshenichkina, Russ J Electrochem **43**, 776 (2007).

[4] X. Cao, C. M. Li, H. Bao, Q. Bao, and H. Dong, Chem. Mater. **19**, 3773 (2007).

[5] L. Bokobza, Polymer **48**, 4907 (2007).

[6] P. Roach, D. Eglin, K. Rohde, and C. C. Perry, J Mater Sci: Mater Med **18**, 1263 (2007).

[7] N. Hasirci, T. Endogan, E. Vardar, A. Kiziltay, and V. Hasirci, Surf. Interface Anal. **42**, 486 (2010).

[8] Y. Wan, X. Qu, J. Lu, C. Zhu, L. Wan, J. Yang, J. Bei, and S. Wang, Biomaterials **25**, 4777 (2004).

[9] Y. WAN, C. TU, J. YANG, J. BEI, and S. WANG, Biomaterials **27**, 2699 (2006).

[10] M. T. Khorasani, H. Mirzadeh, and S. Irani, Radiation Physics and Chemistry **77**, 280 (2008).

[11] H. Park, J. W. Lee, K. E. Park, W. H. Park, and K. Y. Lee, Colloids and Surfaces B: Biointerfaces **77**, 90 (2010).

[12] H. Yasuda, *Plasma Polymerization* (Academic Press Inc., n.d.).

[13] R. B. Timmons and A. J. Griggs, in *Plasma Polymer Films*, edited by H. Biederman (Imperial College Press, 2004).

[14] D. W. Hess and D. B. Graves, *Chemical Vapor Deposition: Principles and Applications* (Academic Press Inc., San Diego, 1993).

[15] A. Grill, *Cold Plasmas in Materials Fabrication: From Fundamentals to Applications* (IEEE Press, 1994).

[16] A. Belkind, Vacuum Technology & Coatings 80 (2007).

[17] C.-M. Chan, T.-M. Ko, and H. Hiraoka, Surface Science Reports **24**, 1 (1996).

[18] C. F. F. A. C. J. P, 1 (2002).

[19] E. R. Fisher, Plasma Processes Polym. **1**, 13 (2004).

[20] J. Zhang and E. R. Fisher, J. Phys. Chem. B **108**, 9821 (2004).

[21] D. Liu, I. T. Martin, J. Zhou, and E. R. Fisher, Pure Appl. Chem. **78**, 1187 (2006).

[22] D. S. Wavhal, J. Zhang, M. L. Steen, and E. R. Fisher, Plasma Processes Polym. **3**, 276 (2006).

[23] V. Kearns, A. Mistry, S. Mason, Y. Krishna, C. Sheridan, R. Short, and R. L. Williams, J Mater Sci: Mater Med **23**, 2013 (2012).

[24] L. Watkins, A. Bismarck, A. F. Lee, D. Wilson, and K. Wilson, Applied Surface Science **252**, 8203 (2006).

[25] L. O'Toole and R. D. Short, J. Chem. Soc., Faraday Trans. **93**, 1141 (1997).

[26] L. O'Toole, C. A. Mayhew, and R. D. Short, J. Chem. Soc., Faraday Trans. **93**, 1961 (1997).

[27] J. Friedrich, Plasma Processes Polym. **8**, 783 (2011).

[28] J. Friedrich, R. Mix, G. Kühn, I. Retzko, A. Schönhals, and W. Unger, Composite Interfaces **10**, 173 (2003).

[29] A. J. Beck, S. Candan, R. M. France, F. R. Jones, and R. D. Short, Plasmas and

Polymers **3**, 97 (1998).
[30] E. Gallino, S. Massey, M. Tatoulian, and D. Mantovani, Surface & Coatings Technology **205**, 2461 (2010).
[31] N. Moreau, O. Feron, B. Gallez, B. Masereel, C. Michiels, T. Vander Borght, F. Rossi, and S. Lucas, Surface & Coatings Technology **205**, S462 (2011).
[32] J.-C. Ruiz, A. St-Georges-Robillard, C. Thérésy, S. Lerouge, and M. R. Wertheimer, Plasma Processes Polym. **7**, 737 (2010).
[33] M. L. Steen, A. C. Jordan, and E. R. Fisher, Journal of Membrane Science **204**, 341 (2002).
[34] K. R. Kull, M. L. Steen, and E. R. Fisher, Journal of Membrane Science **246**, 203 (2005).
[35] H. Yasuda and T. Hirotsu, Journal of Polymer Science: Polymer Chemistry Edition **16**, 229 (1978).
[36] A. J. Beck, J. D. Whittle, N. A. Bullett, P. Eves, S. Mac Neil, S. L. McArthur, and A. G. Shard, Plasma Processes Polym. **2**, 641 (2005).
[37] F. Intranuovo, E. Sardella, R. Gristina, M. Nardulli, L. White, D. Howard, K. M. Shakesheff, M. R. Alexander, and P. Favia, Surface & Coatings Technology **205**, S548 (2011).
[38] E. D. Yildirim, R. Besunder, D. Pappas, F. Allen, S. Güçeri, and W. Sun, Biofabrication **2**, 014109 (2010).

# CHAPTER 2

# EXPERIMENTAL METHODS

This chapter provides a description of the materials, methods, and instrumentation necessary to perform the experiments and subsequent gas-phase and surface analyses described in this dissertation. A basic description of the plasma reactor used in many of these experiments is described in Section 2.1, with modifications and design evolutions of this basic model detailed in Chapter 5. Section 2.2 discusses methods of surface and gas-phase characterization, as well as UV/vis analyses associated with the experiments in Chapter 3. Section 2.3 describes the different analyses for the biological studies in Chapter 7.

## 2.1 General Information

### 2.1.1. Reactor Design

The plasma deposition and surface activating processes described in Chapters 3, 4, and 6 were performed in a 40 cm tubular glass inductively coupled plasma (ICP) reactor, illustrated in Fig. 2.1 and described previously.[1,2] Unless otherwise indicated, samples were placed on a substrate holder oriented parallel to the gas flow on the center axis on the reactor. Samples were placed in the coil region of the reactor, or at alternate locations downstream of the plasma coil. Where applicable, heating of substrates was achieved using a ceramic substrate heater resistively heated with a 2-10 A, 12 V current supply coupled to a variable transformer. Substrate temperatures ($T_S$) were monitored using a K-type thermocouple wire (Ni80/Cr20) coupled with an Omega digital thermometer. $T_S$ values ranged from ~300 K (no heating of the substrate) to 500 K. Gases were mixed in a home-built gas manifold system and introduced to the reactor

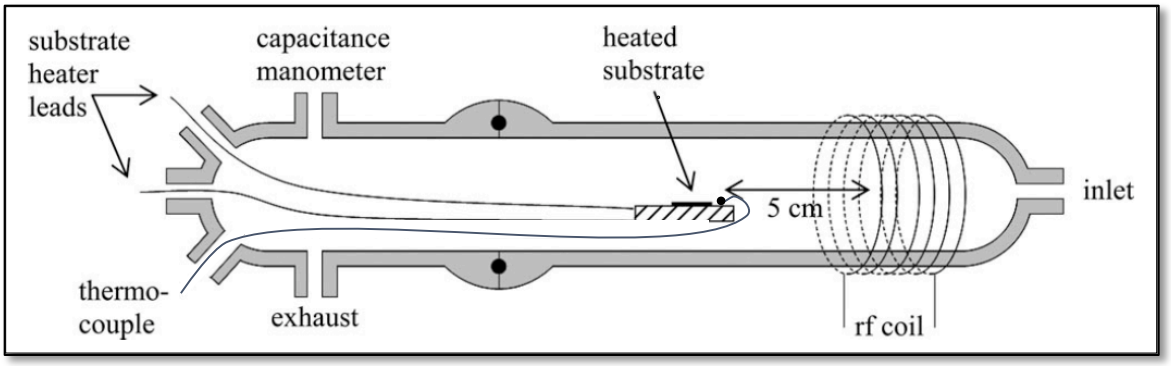


**Figure 2.1** Schematic of the ICP apparatus used for the plasma deposition and modification studies described in Chapters 3, 4, and 6.

through an inlet port located upstream of the plasma coil. MKS mass flow controllers and Nupro bellows sealed metering valves regulated the flow of gas precursors and vapor from liquid precursors, respectively. The total system pressure and partial pressures of each monomer gas were measured with an MKS Baratron capacitance manometer. Plasma ignition occurred when 13.56 MHz of RF power (*P*) was supplied to a nickel-plated copper coil. Gas-phase plasma species were removed from the system by a mechanical rotary pump with a liquid-$N_2$ cold trap.

The plasma modification studies in Chapter 7 were conducted with a capacitively coupled plasma (CCP) reactor, Figure 2.2, consisting of a borosilicate glass chamber 30 mm in diameter and 118 cm long. The plasma discharge was initiated with three external, capacitively-coupled copper band ring-electrodes connected to a 13.56 MHz radio frequency (rf) power source (RFX600, Advanced Energy). The impedance of the circuit was matched manually using a home built matching network. The electrodes were on a translatable carriage that traversed the length of the glass reactor such that experiments could be performed in either a static (not moving) or translating mode. Sensors on either end of the electrode track were triggered by a sensor on the center electrode, reversing the direction of the electrode trolley, resulting in a smooth, continuous movement of the plasma discharge during translating electrode experiments. The position of the sensors could be adjusted to change the distance traveled by the electrodes. Samples were placed in a custom polyethylene sample holder, Figure 2.3, oriented such that the gas flow was parallel with the top of the samples.

### 2.1.2 Precursor and Sample Preparation

Liquid precursors were placed in a Pyrex side-arm vacuum flask and underwent at least three freeze-pump-thaw cycles to remove dissolved gases prior to use. The liquid precursors used in these studies were hexamethyldisiloxane (HMDSO, Fluka, 99.5%), hexylamine

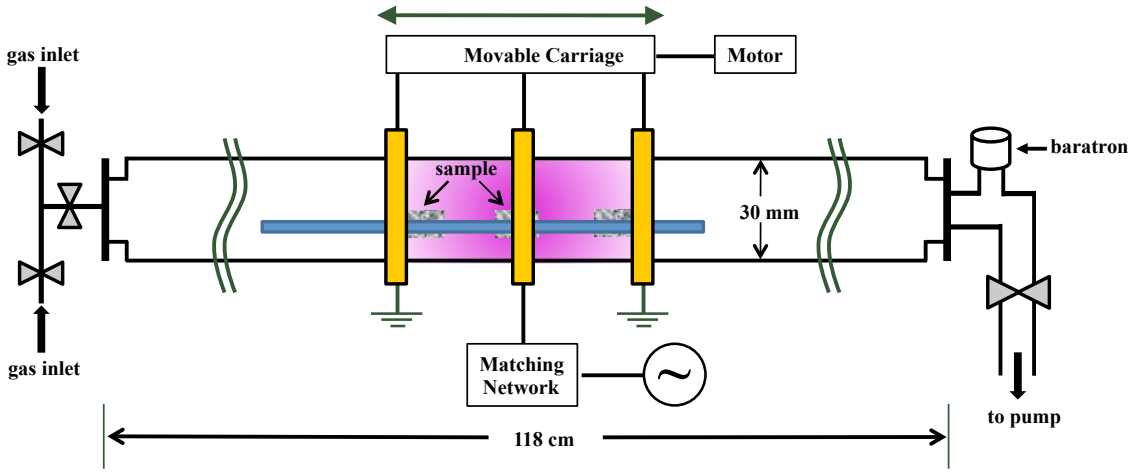


**Figure 2.2** Schematic of the CCP apparatus used for plasma modification studies described in Chapter 7.

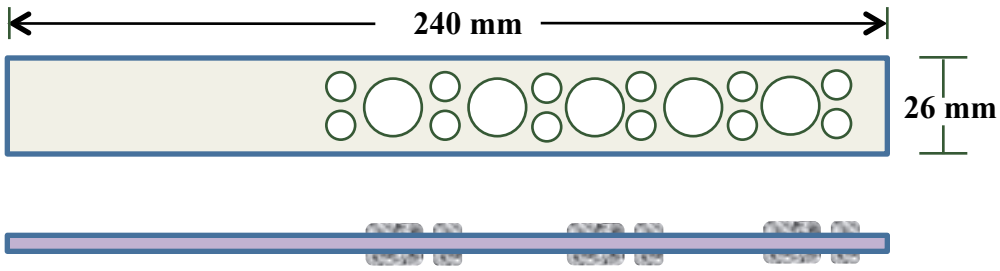


**Figure 2.3** Schematic of the sample holder used for plasma modification studies described in Chapter 7.

(HexAm, Acros, 99%), allyl alcohol (allylOH, Sigma-Aldrich, ≥99%), allylamine (allylNH, Sigma-Aldrich, 98%), and deionized $H_2O$ (18 MΩ cm). Gaseous precursors used throughout this dissertation were $O_2$ (Airgas, 99.5%), Ar (Airgas, 99.9%), and $N_2$ (Airgas, 99.5% and Air Liquide, 99.99%). The pressure of all monomer gases were allowed to stabilize for at least 10 min before plasma ignition.

*Preparation of np substrates.* $TiO_2$ (anatase, 5 nm) and $Fe_2O_3$ nps (≤ 50 nm) were coated onto Si wafers to create supported np substrates. The nps were suspended in methanol to saturation, spread onto the wafers, and allowed to dry overnight at ambient laboratory conditions. Free np substrates were used as-received from the supplier.

*Preparation of polymeric scaffolds.* Poly(ε-caprolactone) (PCL; $\mathcal{M}$ = 65 kDa) scaffolds were fabricated using a solvent casting/particulate leaching technique described previously[3] and detailed in *Appendix A*. Briefly, PCL pellets were dissolved in $CHCl_3$ (20/80 w/w, Sigma Aldrich) and allowed to sit in a sealed container for 2-4 h, forming a viscous, homogeneous solution. To create the scaffolds, NaCl (99%, Sigma Aldrich) was used as the porogen and was incorporated into the PCL solution (5/95 w/w PCL/NaCl). The granular mixture was hand-pressed uniformly into the wells of custom made Teflon® molds. The wells were either 10 or 20 mm in diameter and either 3 or 4 mm deep. The molded constructs were allowed to air dry for 1 h at room temperature and subsequently immersed in ethanol for 3 h to allow phase separation and solvent evaporation. Upon removal from the ethanol, the molds were immersed in DI water overnight to begin the leaching process. The individual samples were removed from the mold and immersed in fresh DI water for an additional 36-48 h to leach any remaining salt. During this period the water was replaced 2-3 times per day. Upon completion of the leaching period, the scaffolds were removed from the water and allowed to dry in air at room temperature for

several days before use or were vacuum dried overnight in the plasma reactor to speed the drying process.

## 2.2 Surface and Gas-phase Characterization Methods

*X-ray photoelectron spectroscopy (XPS).* In Chapters 3-6 and Chapter 8, the surface composition of plasma treated samples was determined using XPS and was performed on a Physical Electronics PE5800 ESCA/AES system for. Spectra were collected using a monochromatic Al $K_\alpha$ X-ray source (1486.6 eV), hemispherical analyzer, and multichannel detector. Electron (16-24 eV) and Ar neutralizers were used for charge neutralization. Unless otherwise indicated, the spectra for films described in Chapters 3-6 and Chapter 8 were charge corrected by setting the hydrocarbon component C–C to 284.6 eV and 285.0 eV, respectively. Films deposited using HexAm plasmas were charge corrected using the $TiO_2$ component at 458.8 eV. High-resolution XPS spectra were analyzed using XPSPEAK 4.1 software (Raymund Kwok, UK Surface Analysis Forum). Curve fitting was achieved using Gaussian functions with each full width at half maximum (FWHM) of each peak being ~2.0 eV. Curve fitting for the various high-resolution XPS spectra discussed in this dissertation are outlined within individual chapters as it applies to the materials analyzed. The photoelectron take-off angle was 45°, which corresponds to a sampling depth of ~40–45 Å.

XPS data in Chapter 7 were collected at the University of Bari with a Theta Probe Thermo VG scientific instrument (monochromatic Al $K_\alpha$ X-ray source; 1486.6eV; take-off angle 45°, 300 μm spot size). Samples were neutralized with an Ar flood gun (Model822-06 FG; 1 eV; $10^{-7}$ mbar). Binding energies were charge corrected by setting the $C_{1s}$ aliphatic carbon signal to 285.0 eV. $C_{1s}$ peak fitting was performed using Thermo Scientific Avantage Data System

software. High resolution data fitting of PCL scaffolds is described in detail and was based on XPS fitting procedures outlined in multiple literature resources.[3-5] XPS analysis of the scaffold cross-section was performed after freeze-fracturing with liquid $N_2$.

*Scanning Electron Microscopy (SEM)*. A JEOL, JSM-6500F field emission scanning electron microscope was used to analyze the surface morphology of untreated and plasma treated samples. An accelerating voltages of 3.0-15.0 kV and working distance of 10 mm were used for all analyses unless otherwise indicated. Samples in Chapters 3-5 were sputtered with 5-20 nm of gold to reduce sample charging. Samples in Chapters 7-8 were imaged without addition of anti-charging agents.

*Fourier-transform infrared spectroscopy (FTIR)*. Analysis of functional groups was performed with a Thermo Scientific Nicolet 6700 FTIR with a Harrick Scientific Products VariGATR grazing angle attenuated total reflectance accessory. Spectra were collected with a resolution of 4 $cm^{-1}$ and averaged over 32 or 64 scans. Plasma conditions were adjusted such that the relative thickness of the deposited films was uniform.

*Contact angle goniometry*. The water contact angle (WCA) of plasma treated surfaces was measured as a gauge of the surface hydrophilicity. Measurements in Chapters 4, 6, and 8 were performed using either a Krüss DSA 10 or a DSA 30 contact angle goniometer. Deionized water (18 MΩ cm) with drop volumes of 2 or 4 $\mu$L were used to measure the WCA on multiple samples to account for differences in surface uniformity. When possible, the WCA for three distinct locations on each sample was measured. Video capture was utilized to evaluate how water drops spread across solid samples and absorbed into porous samples as a function of time.

WCA measurements in Chapter 7 were performed with a KSV CAM 200 system to evaluate the change in WCA of the scaffolds following plasma modification. Two samples from

each set of parameters were utilized for WCA measurements. For each sample, five readings were measured at different positions on the scaffold and averaged. For each scaffold reading, 400 frames were captured by the camera at intervals of 6 ms. The WCA and volume of the drop were measured and calculated by the instrument's software. Due to the adsorption of the water droplet by the plasma-treated scaffolds, the kinetics of absorption was measured in terms of rate of change in volume (V) of the water drop ($\Delta V/\Delta t$) and change in WCA ($\Delta WCA/\Delta t$). Fitting the WCA and volume data with a third order polynomial, Figure 2.4, allowed us to extract WCA values at $t = 0$ (Fig. 2.4a) and the water absorption rate of the samples (Fig. 2.4b). We chose here to report the WCA at $t = 0$ because this time point is the best representation of interactions at the surface (i.e. interactions dependent on surface functionality), whereas WCA at $t > 0$ contains contributions from the way the drop absorbs through porous scaffold networks. Due to instrument limitations, absorption rates in Chapter 8 were calculated by measuring the length of time it took for a 4 μL drop to completely absorb within the scaffold (with $t_0$ assigned to the moment the drop touched the scaffold surface).

*Variable angle spectroscopy ellipsometry (VASE) and profilometry.* The deposition rates for films produced in Chapter 3 were analyzed using a Bruker Dektak IID profilometer. Samples were masked during deposition to produce a step and the step height was measured as a function of plasma deposition time to calculate an average deposition rate. The thickness of films produced in Chapters 4 and 5 were measured using a Woollam M-2000 model DI ellipsometer and analyzed using WVASE software. The film thickness for films discussed in Chapter 6 were measured with a Bruker DektakXT profilometer and analyzed using Bruker Vision64 Update 5 software.

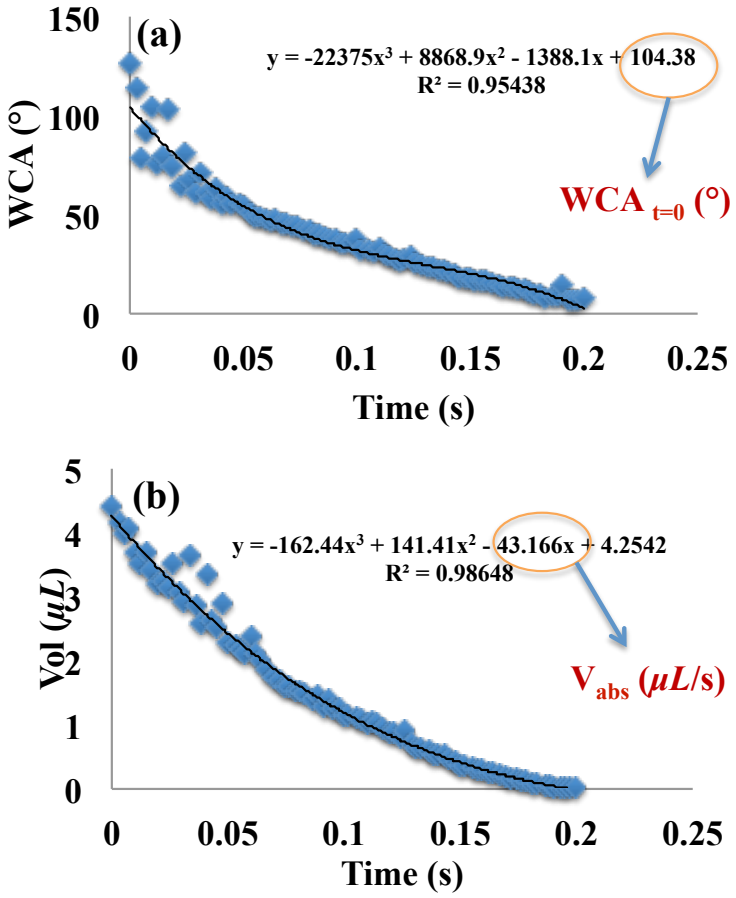


**Figure 2.4** Water contact angle (Fig. 2.4a) and water drop volume (Fig. 2.4b) as a function of time. The equation shown is for a line of best fit, and is used to produce data shown in Fig. 7.2 and 7.3.

*Actinometric optical emission spectroscopy (AOES)*. The plasma reactor setup described in Fig 2.1 can easily be adapted for a multitude of *in-situ* plasma diagnostics. The characterization of gas-phase species was performed with an Avantes AvaSpec multichannel spectrometer comprising four fiber optic gratings and four charge-coupled array detectors with a combined wavelength range of 187 to 1016 nm with ~0.1 nm resolution. The majority of the spectra shown were collected by averaging ten accumulations at integration times of 10-100 ms. AOES determines the density of gas-phase species relative to that of an internal standard (Ar),[6] which is added to the plasma gas feed in concentrations ≤ 5% of the total system pressure. Specific details of the AOES apparatus setup are similar to those reported previously.[7]

*Ultraviolet/visible spectroscopy (UV/vis)*. The stability and dispersion of untreated and treated nanoparticles discussed in Chapter 3 were examined using a 2000 Varian Cary-500 UV–vis-NIR spectrophotometer. Samples for dispersion analysis were prepared by scraping the nanoparticles off the microslide substrates and creating a 0.035 % (w/v) suspension of nanoparticles in deionized (DI) water. Nanoparticle suspensions were sonicated for 10 min prior to acquiring the first spectrum to ensure homogeneous dispersion. Spectra were acquired immediately after sonication and at subsequent 2 h intervals over a period of 8 h. Between measurements, the solutions were allowed to rest under ambient laboratory conditions.

## 2.3 Biological Analyses

Cell splitting protocols and detailed procedures for many of the biological analyses described in Chapter 7 are outlined in *Appendix B*. In brief, native and plasma-treated scaffolds were treated with Saos-2 osteoblasts ($5.0 \times 10^4$ cells/scaffold) and allowed to culture for 18, 42, and 114 h.

*MTT colorimetric assay*. Cell viability was determined by measuring the cell mitochondrial activity using the MTT colorimetric assay. After incubation, scaffolds were treated with a tetrazolium dye, which is reduced to formazen crystals by mitochondria within living cells. The concentration of the formazen crystals is a measure of cell viability, and thus was measured with UV/vis spectroscopy ($\lambda$ = 570 nm) to determine if the cells on the scaffolds were alive.

*Fluorescence microscopy*. Cell morphology and clustering characteristics were analyzed with an Axiomat epifluorescence microscope (Zeiss, Germany). Prior to analysis, cells were fixed in a 4% formaldehyde/PBS solution and permeabilized with PBS containing 0.1% Triton X-100. Scaffolds were then incubated with Alexa Fluor488 phalloidin to allow for imaging of the cytoskeleton.

REFERENCES


[1] C. I. Butoi, N. M. Mackie, L. J. Gamble, D. G. Castner, J. Barnd, A. M. Miller, and E. R. Fisher, Chem. Mater. **12**, 2014 (2000).

[2] K. Bogart, N. F. Dalleska, G. R. Bogart, and E. R. Fisher, Journal of Vacuum Science & Technology a: Vacuum, Surfaces, and Films **13**, 476 (1995).

[3] F. Intranuovo, E. Sardella, R. Gristina, M. Nardulli, L. White, D. Howard, K. M. Shakesheff, M. R. Alexander, and P. Favia, Surface & Coatings Technology **205**, S548 (2011).

[4] C. Yen, H. He, Z. Fei, X. Zhang, L. J. Lee, and W. S. W. Ho, International Journal of Polymeric Materials **59**, 923 (2010).

[5] E. D. Yildirim, R. Besunder, D. Pappas, F. Allen, S. Güçeri, and W. Sun, Biofabrication **2**, 014109 (2010).

[6] N. Fuller, M. V. Malyshev, V. M. Donnelly, and I. P. Herman, Plasma Sources Science and Technology **9**, 116 (2000).

[7] K. J. Trevino and E. R. Fisher, Plasma Processes Polym. **6**, 180 (2009).

# CHAPTER 3

# COMPOSITE $SiO_2/TiO_2$ AND AMINE POLYMER/$TiO_2$ SUPPORTED NANOMATERIALS

This chapter contains data from a full paper published in *Applied Surface Science* and written by Jeffrey C. Shearer, Mary J. Fisher, D. Hoogeland, and Ellen R. Fisher. This work expanded upon the Master's thesis of M.J. Fisher and continued preliminary work started by D. Hoogeland, an undergraduate coworker. FTIR and TEM data were provided by M.J. Fisher. The studies examine plasma enhanced chemical vapor deposition of $SiO_2$ and amine-polymer films onto supported $TiO_2$ substrates. Deposition parameters were optimized to give various film types, and the nanoparticles were analyzed for changes in size and morphology. Nanoparticles were suspended in water to gain insight into how the thin films affected the dispersion properties of the materials.

## 3.1 Introduction

The formation of composite materials using industrially compatible techniques is a burgeoning area of research across many disciplines. Composite materials have an array of potential applications including use as fuel cells, biological labels, mechanical reinforcement, and accelerator magnets.[1-4] Concomitantly, the need for high surface area materials has also accelerated research into smaller dimension materials in the past few decades. $TiO_2$ nanoparticles are high on the list of nanoscale materials widely used in a range of applications.[5-7] The development of composite $TiO_2$ nanoparticles could create a class of nanoscale materials with unique properties. More importantly, synthesis methods that alter only the surface properties of nano-

particles would result in the retention of the desirable mechanical and physical properties of $TiO_2$, while affording improved surface properties for specific applications. For example, George, Weimer, and coworkers have pioneered the use of atomic layer deposition (ALD) to conformally coat metal oxide nanoparticles with very thin films of $TiO_2$ and ZnO. ALD methods, however, are currently limited to a relatively small number of film chemistries. Thus, development of new methodologies for creation of nanocomposites could provide lower cost and higher performance materials.

Another promising method for production of nanoscale composite materials involves low-temperature plasmas via film deposition, plasma sputtering, or surface modification. As noted in Section 2.1, plasmas offer several advantages in materials synthesis, most notably that the properties and formation of materials can be controlled using a range of plasma system variables and that a wide range of film chemistries are available. For example, the placement of a substrate relative to the intense region of a plasma can allow for species to have more time to react with the surface or may limit the type of gas species reacting with the substrate, thereby creating very different types of films at different locations.[8-9] The amount and waveform of the applied rf power ($P$) can also significantly affect film composition; pulsing the applied power, as opposed to supplying power continuously can limit substrate damage and typically produces a less cross linked material.[10-13] Additional parameters that affect film chemistry include feed gas type and ratio, substrate temperature ($T_S$) and total system pressure.

Recent studies have attempted to produce $TiO_2$ composite nanoscale materials through a variety of plasma-based techniques. Zhu et al. used plasma-enhanced chemical vapor deposition (PECVD) methods to coat $TiO_2$ nanoparticles with polyacrylic acid and explored the effects of the coating on dispersion of the treated nanoparticles in glycol.[14] The treated nanoparticles ex-

hibited improved dispersion over that of the untreated, suggesting the performance of the material was enhanced by the coating. Timmons and coworkers used PECVD to coat $TiO_2$ nanoparticles with tetrametyltin (TMT) and perfloropropylene oxide to produce thin oxide layers of TMT and partially fluorinated oxide films.[15] The PECVD-coated $TiO_2$ nanoparticles exhibited a higher oxidation rate for acid orange dye than untreated materials. Another plasma-based method for modification of $TiO_2$ nanoparticles entailed the use of plasma sputtering of $TiO_2$ and polymer targets to produce $TiO_2$/hydrocarbon composites.[16] Film properties such as material wettability, inclusion size and surface roughness were found to depend strongly on sputtering parameters such as sputter voltage and $TiO_2$/hydrocarbon ratios.

The Fisher labs have explored a variety of PECVD methods for creation of different types of materials,[8-10,17] as well as development of novel methods for coating or modifying extant structures, including nanotubes, membranes, and fibers.[18-20] For example, Malkov et al. used PECVD to produce micropatterned substrates from a variety of hydrocarbon monomers, including hexylamine (HexAm), acrylic acid, N-vinyl-2-pyrrolidinone, N-vinylformamide, and allylamine for applications in cellular attachment studies.[9,18] These studies showed plasma polymerized materials can direct the growth of different cell types on surfaces. We have also demonstrated the efficacy of plasma deposition and plasma surface modification for the production of composite materials including polypyrrole-coated gold nanotubes, nonwoven polyethylene fibers, and microporous polymer membranes.[19,20]

One material that has been used for coating nanostructures is $SiO_2$, as silica is soluble in aqueous solutions and can improve a variety of other surface properties such as biocompatibility and biodegradation.[21,22] Hexamethydisiloxane (HMDSO) is perhaps the most extensively used $SiO_2$ film precursor,[23-31] although a variety of alkoxysilane/$O_2$ and alkoxysilane/$N_2O$ plasmas

have been used to deposit $SiO_2$-like films.[29, 32-34] With all alkoxysilanes, increasing the oxidant in the gas feed significantly enhances the $SiO_2$ character of the deposited films, with films deposited at low oxidant concentrations having film compositions best characterized as the more organic polymer-like SiOxCyHz.[29] Other parameters such as *P* and total system pressure also affect film properties, with higher *P* and pressures tending to produce higher quality $SiO_2$ films (i.e. lower carbon and SiOH content). More recently Kersten and coworkers deposited $SiO_x$ layers on powders using a dielectric barrier discharge (DBD).[35] FTIR data for deposited films indicate a small decrease in the hydrocarbon content of the deposited films with increasing oxygen in the feed. Their XPS data supported the trend of creating a more inorganic-like film using high oxidant concentration.

Here, we have used continuous wave HMDSO/$O_2$ and pulsed HexAm plasmas to coat commercial $TiO_2$ nanoparticles. Coating and analyzing nanoparticles that are secured to substrates is useful because many applications such as photovoltaic devices (solar cells) utilize nanoparticles that are attached to substrates.[36-38] In this context, only the exposed surfaces would have need of conformal coating. Thus, in this work, we use the term ‘‘conformal’’ to indicate a coating that has preserved the overall morphology of the underlying (or original) substrate, which in this case comprises a multilayer of nanoparticles.

With both deposition systems, the $TiO_2$ nanoparticles were conformally coated and the resulting materials were characterized using Fourier-transform infrared spectroscopy (FTIR), X-ray photoelectron spectroscopy (XPS), and scanning electron microscopy (SEM). The two systems provide a wide range of film compositions to explore from the very inorganic-like $SiO_2$ films deposited at high oxidant concentrations in the HMDSO plasma, to silicion-based polymer networks in HMDSO plasmas with low oxidant levels, to the amine-containing polymeric mate-

rials created in the HexAm plasmas. The influence of film composition on the dispersion of the nanoparticles in deionized water was explored.

## 3.2 Results and Discussion

**3.2.1. $SiO_2$ Films.** One key element to successful coating technologies is the ability to conformally coat unusually-shaped substrates. With nanoscale materials, this is especially important as any processing step may significantly alter the morphology of the material to be coated. Figure 3.1 shows two SEM images of uncoated nanoparticles. In Fig. 3.1a, the as-received nanoparticles were adhered to Cu tape prior to SEM analysis. In Fig. 3.1b, the as-received $TiO_2$ nanoparticles underwent the suspension in methanol and spreading step described above, prior to SEM analysis. As can be seen from these two images, the preparation step we use to get the nanoparticles into the plasma for coating did not appreciably change the morphology of the material. The major difference between the two images arises primarily from the density of the nanoparticles on the underlying substrate. In both cases, however, the commercial material agglomerates somewhat into nanoparticle clusters when placed on a flat substrate.

The morphology of HMDSO/$O_2$ plasma-treated $TiO_2$ nanoparticles was also examined using SEM. Figure 3.2 shows SEM images of $TiO_2$ nanoparticles on 300 K substrates treated for 10 min in plasmas with $P$ = 50 W. With both the 100% HMDSO and the 50% HMDSO plasma treatments, the $SiO_xC_yH_z$ film appears to have fully coated the nanomaterial with an extremely thick layer, resulting in an apparent coagulation of the nanoparticle clusters. This is consistent with previous results from our laboratory in which high deposition rates of 500-2500 Å/min were observed for these conditions using Si wafers as substrates.[29] Note also that the deposition rate peaked at 50% $O_2$, decreasing to a minimum at the highest $O_2$ dilution (90%). This is consistent

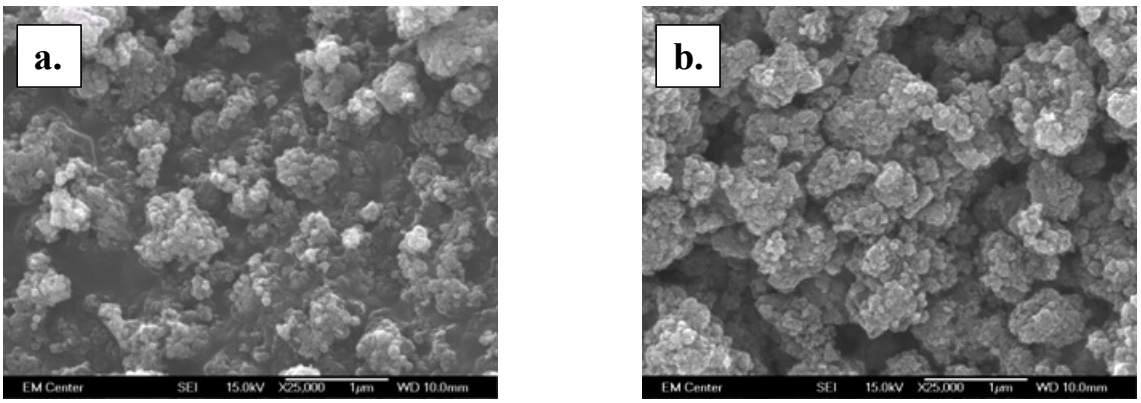


**Figure 3.1** SEM images of uncoated $TiO_2$ nanoparticles (a) adhered to Cu tape for analysis; and (b) on a Si wafer using the suspension in methanol and spreading technique described in Section 2.1.2.

with the apparently thicker coating observed in Fig. 3.2b for the 50% HMDSO (50% $O_2$) plasma. The images shown in Figs. 3.2c and 3.2d clearly indicate that a thinner coating is deposited as the underlying morphology of the nanoparticle clusters is clearly visible. Indeed, the SEM image of nanoparticles coated with a 10% HMDSO plasma looks virtually identical to that of the uncoated material (Fig. 3.1b). This is in good agreement with data from depositions on flat substrates that yielded a deposition rate of ~50–100 Å/min for these conditions.[29] Also, XPS spectra do not contain signal for the underlying nanoparticles (i.e. no signal from Ti), which indicates a film thickness of at least 100 nm, given the sampling depth of XPS.[9] This clearly suggests that not only is our PECVD process a viable route to conformal coatings, but that the use of high oxidant concentration plasmas may yield a higher quality composite material.

Figure 3.3 contains SEM images of nanoparticles coated in 10% and 50% HMDSO plasmas with $T_S$ = 400 K and 500 K. For both feed gas compositions, the coatings produced at the higher $T_S$ clearly reveal the underlying nanoparticles' morphology. At the lower substrate temperature, more of a blanket-like coating can be seen, especially for the 50% HMDSO system, Fig. 3.3c. Interestingly, examining the images for the 50% HMDSO system at 300 K (Fig. 3.2b), 400 K, and 500 K, it appears that the deposition rate increases slightly with $T_S$, and then decreases at the highest temperature, Fig. 3.3d. Unfortunately, we were unable to accurately and directly measure the film deposition rates on $TiO_2$ nanoparticles. This observation is, however, consistent with previous results from our laboratory for $SiO_2$ deposition rates on flat substrates, which were found to be the lowest at elevated $T_S$ for several siloxane precursors.[17,34] The observation of a more blanket-like coating suggests that an elevated $T_S$ may not be suitable for achieving the best conformality with these materials.

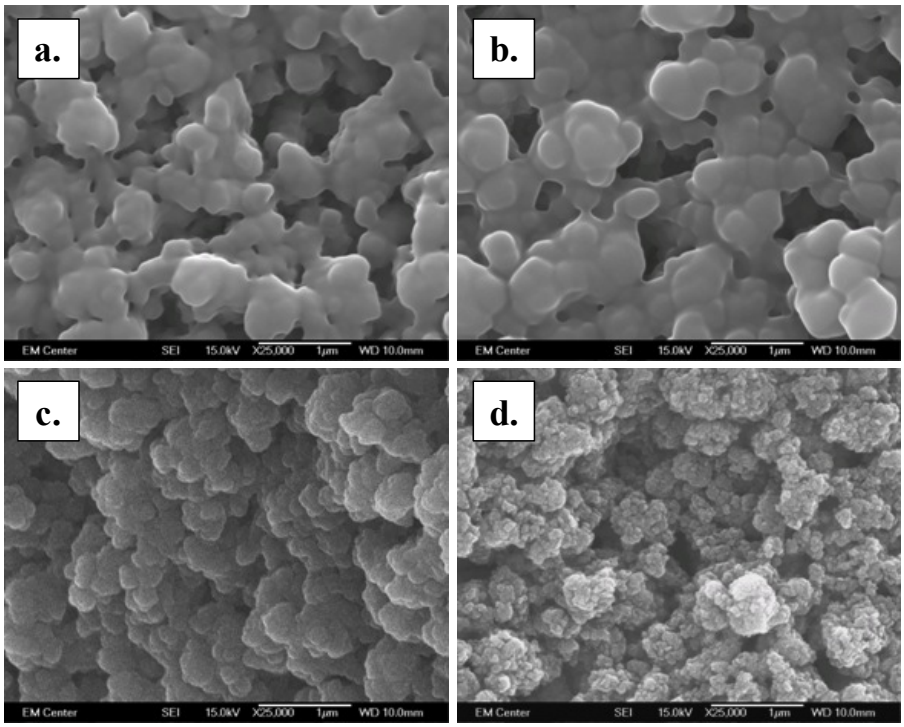


**Figure 3.2** SEM images of $TiO_2$ nanoparticles treated with CW HMDSO/$O_2$ plasmas with (a) 100%, (b) 50%, (c) 20%, and (d) 10% HMDSO in the feed. Deposition parameters were $P$ = 50 W, deposition time = 10 min, reactor pressure of 400 mTorr, and $T_S$ = 300 K. Substrates were placed ~8 cm downstream of the coil region of the plasma.

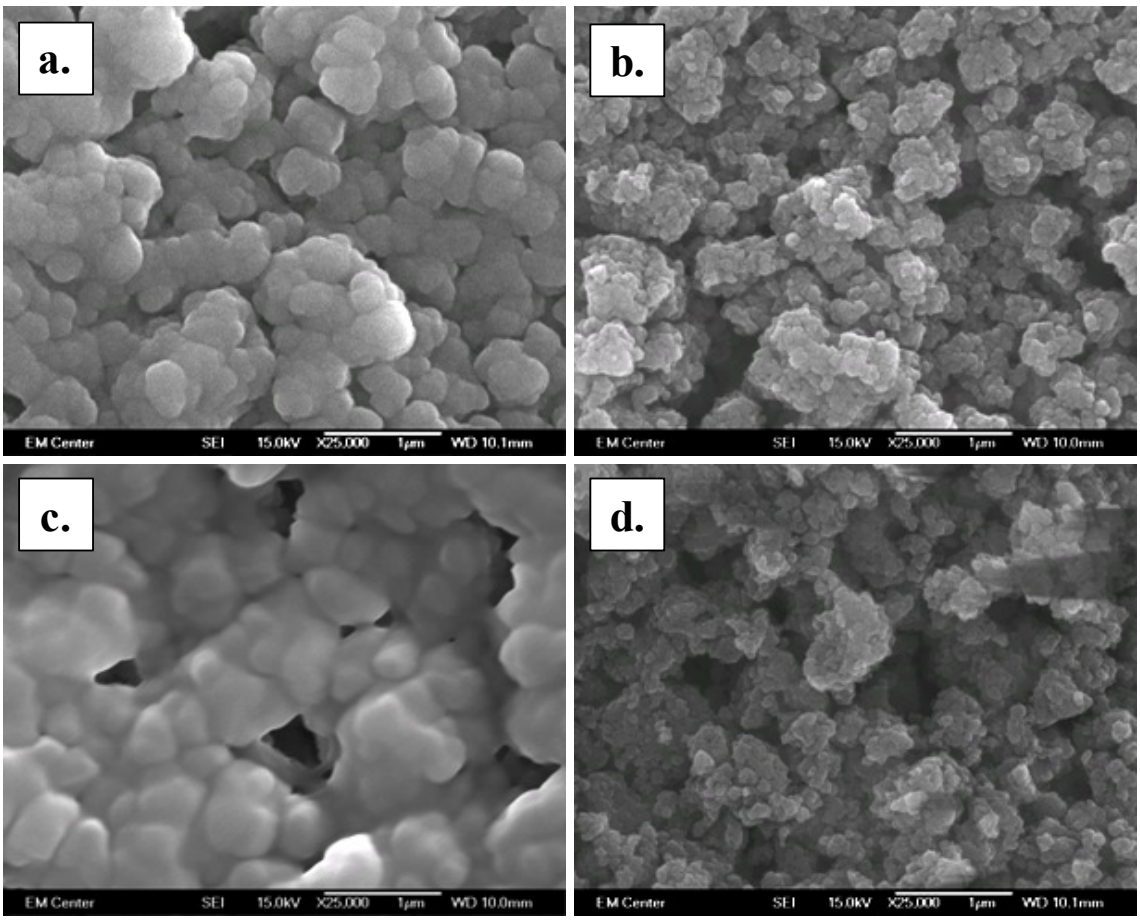


**Figure 3.3** SEM images of $TiO_2$ nanoparticles treated with CW HMDSO/$O_2$ plasmas with (a) 10% HMDSO, $T_S$ = 400 K; (b) 10% HMDSO, $T_S$ = 500 K; (c) 50% HMDSO, $T_S$ = 400 K; and (d) 10% HMDSO $T_S$ = 500 K. Deposition parameters were $P$ = 50 W, deposition time = 10 min, reactor pressure of 400 mTorr. Substrates were placed ~8 cm downstream of the coil region of the plasma.

In addition to coating morphology, film composition was determined using both FTIR and XPS analyses. Figure 3.4 contains FTIR data for $SiO_2$ films produced using 100%, 50%, 20%, and 10% HMDSO plasmas. Although the dominant feature in all spectra is the absorbance band at 1080 $cm^{-1}$, the Si-O-Si/Si-O-C asymmetric stretch, the FTIR spectra illustrate that increasing oxygen content in the gas feed significantly changes film composition. For example, the absorbance band at ~3330 $cm^{-1}$, attributed to the OH stretch in free SiOH, increases slightly with increased $O_2$ in the gas feed, as do the SiOH stretching bands at 960 and 799 $cm^{-1}$. In contrast, the $CH_x$ stretching vibrations at ~2990 $cm^{-1}$ decrease dramatically with increased $O_2$, as do the absorbance bands at ~1200 $cm^{-1}$ and ~1300 $cm^{-1}$ [$Si(CH_3)_x$]. Notably, the Si-O-Si band at ~595 $cm^{-1}$ shifts slightly with different $O_2$ concentrations and increases with increased $O_2$ in the feed. The primary Si-O-Si absorbance band at 1080 $cm^{-1}$ also narrows with increasing $O_2$ in the feed, indicating a more stoichiometric $SiO_2$ is being formed. It has also been observed that with high oxidant concentrations, less hydrocarbon is present in the film because of oxidation reactions occurring in the gas phase as well as at the surface.[17,29,32,34] This supports the observation that the substrate does not significantly influence the resulting film chemistry.

Table 3.1 lists XPS elemental composition data for the as-received $TiO_2$ nanoparticles and for the $SiO_2$-coated $TiO_2$ nanoparticles produced using room temperature substrates and at elevated $T_S$. For the as-received $TiO_2$ nanoparticles, there is a substantial amount of carbon observed in the XPS data. This likely arises from the suspension in methanol method we are using, but some contribution from adventitious carbon is also possible. For coated nanoparticles, there is relatively little Ti present in the elemental composition under any of the film deposition conditions. Thus, the films have completely coated the underlying particles, as visually determined by the SEM data. This is especially relevant for the 10% HMDSO system because the deposition

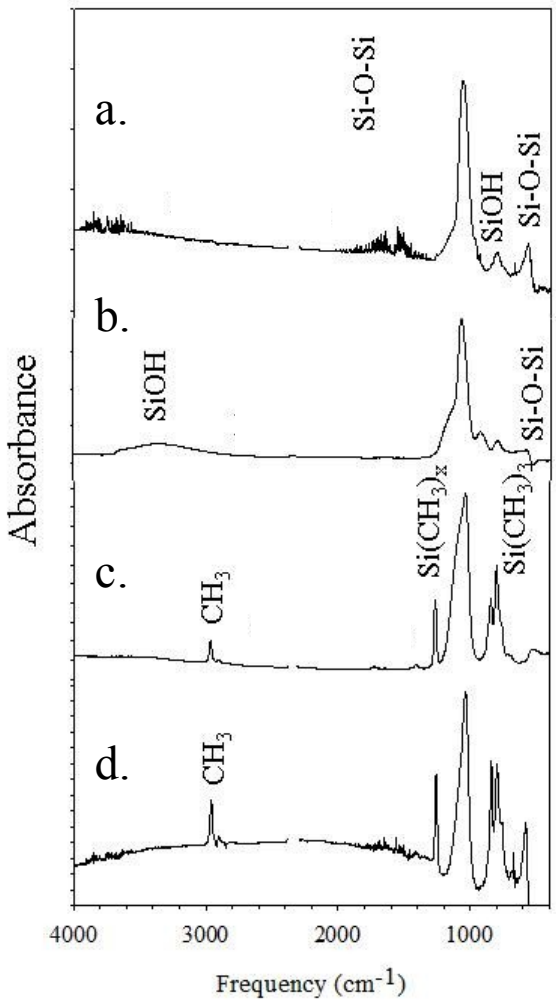


**Figure 3.4.** FTIR spectra of films deposited on $TiO_2$ nanoparticles from HMDSO/$O_2$ plasmas with (a) 10%, (b) 20%, (c) 50%, and (d) 100% HMDSO. Deposition parameters were *P* = 50 W, deposition time = 10 min, reactor pressure of 400 mTorr. Substrates were placed ~8 cm downstream of the coil region of the plasma.

**Table 3.1** XPS atomic concentrations for deposited films ($P$ =50 W).[a]

| $T_S$(K) | HMDSO/$O_2$ | Si(%) | O(%) | C(%) | Ti(%) |
|---|---|---|---|---|---|
| -- | Untreated[b] | -- | 51.7 ± 4.1 | 21.4 ± 4.7 | 25.0 ± 1.8 |
| 300 ± 10 | 100/0 | 25.0 ± 0.7 | 25.4 ± 2.0 | 47.3 ± 1.2 | 2.3 ± 0.7 |
| 300 ± 10 | 50/50 | 24.2 ± 2.2 | 37.4 ± 2.4 | 36.7 ± 2.5 | 4.7 ± 0.1 |
| 300 ± 10 | 20/80 | 28.4 ± 0.7 | 51.6 ± 1.4 | 20.0 ± 1.3 | --- |
| 300 ± 10 | 10/90 | 29.8 ± 0.5 | 66.6 ± 0.6 | 3.4 ± 0.6 | 0.3 ± 0.2 |
| 400 ± 10 | 50/50 | 23.2 ± 1.9 | 36.4 ± 1.3 | 38.3 ± 0.7 | 2.1 ± 1.3 |
| 500 ± 10 | 50/50 | 24.6 ± 3.3 | 41.1 ± 1.6 | 34.3 ± 4.2 | --- |
| 400 ± 10 | 10/90 | 26.8 ± 2.1 | 70.1 ± 2.5 | 2.7 ± 1.0 | 0.5 ± 0.4 |
| 500 ± 10 | 10/90 | 26.8 ± 0.5 | 67.4 ± 0.9 | 6.1 ± 0.6 | --- |

[a]Values obtained from high resolution XPS spectra of $SiO_2$ films deposited on $TiO_2$ nanoparticles using a 10 min deposition time for all experiments. Errors are the standard deviation of the mean of 3 measurements on a minimum of 2 samples. [b]These measurements were made on the as-received $TiO_2$ nanoparticles.

rate is low and the coating is at least 100 nm in thickness. These results again compare favorably with previous work on conformal coverage of unusually-shaped substrates.[19] Note however, that the conditions that give rise to the larger Ti concentrations in the XPS data also produce films with a more blanket-like coating as observed by SEM. Thus, the higher levels of titanium observed in the XPS data are likely the result of not having as conformal a coating under these conditions.

The Si concentration in the films appears to be relatively unaffected by the oxidant content of the feed gas or by $T_S$. In contrast, however, the percent C in the films produced on room temperature $TiO_2$ substrates, decreased significantly with increasing oxidant concentration, accompanied by a concomitant rise in the O content. Again, these results are strongly correlated to the results obtained for depositions on flat substrates.[29] For both the 50% and 10% HMDSO systems, the film content does not change appreciably with $T_S$. Figure 3.5 shows charge-corrected high-resolution XPS $Si_{2p}$ spectra for films deposited onto $TiO_2$ nanoparticles with different $O_2$ dilutions in the plasma ($P$ = 50 W, $T_S$ = 300 K, deposition time of 10 min). The $Si_{2p}$ peak shifts to higher binding energy for films produced with higher oxidant concentrations, indicating the oxidant influences the nature of the $SiO_2$ network deposited onto the nanoparticles. The shift to higher binding energies indicates that a more $SiO_2$-like film is formed.

The nature of the deposited films can be further explored by deconstructing the $Si_{2p}$ peak to determine the contributions from different $SiO_x$ moieties. Alexander et al. proposed four different environments for silicon atoms in $SiO_x$ networks, abbreviated as $Si(–O)_1$, $Si(–O)_2$, $Si(–O)_3$, and $Si(–O)_4$ with binding energies at 101.5, 102.1, 102.8, and 103.4 eV, respectively, where the $Si(–O)_4$ designation indicates a tetrahedral $SiO_2$ network.[40] Note the $Si(–O)_1$ and $Si(–O)_2$ peaks overlap the Si-C binding environment in the XPS

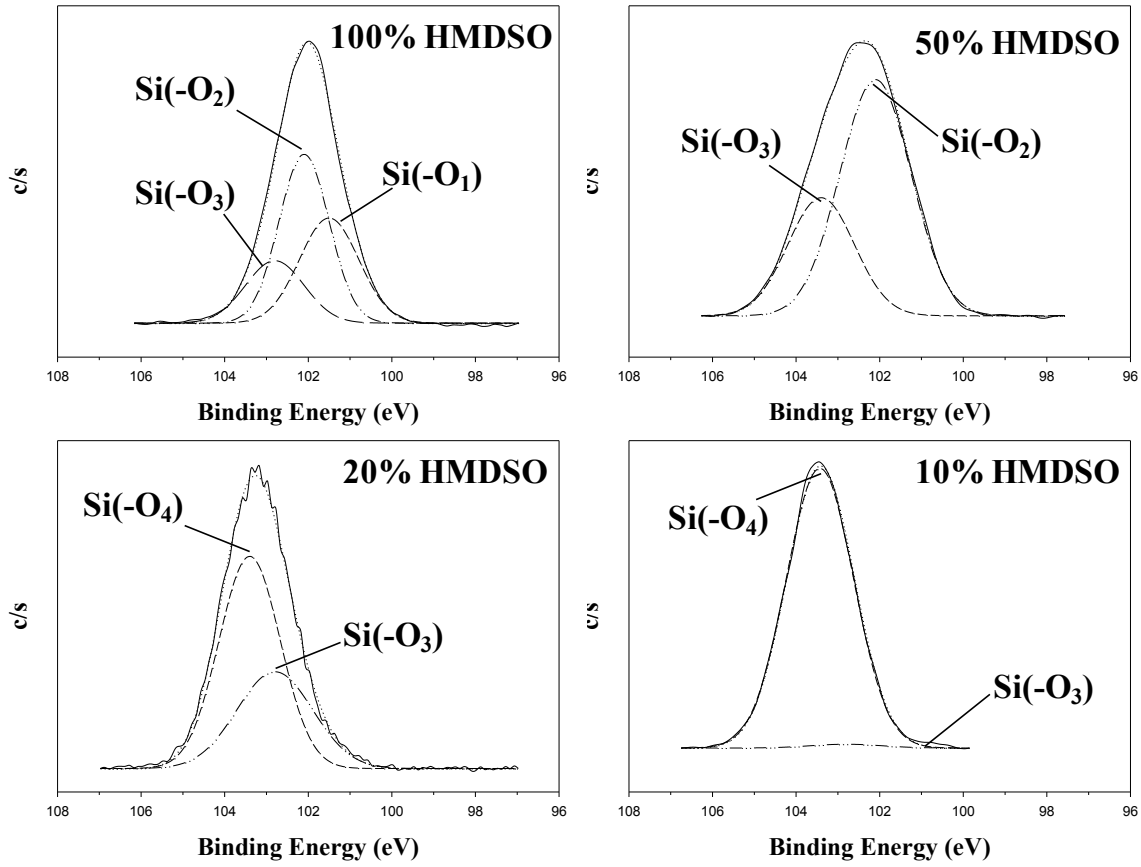


**Figure 3.5** XPS $Si_{2p}$ high-resolution spectra for films deposited from plasmas with a deposition time of 10 minutes, $T_S$ = 300 K, and $P$ = 50 W with the specific HMDSO content in the feed shown (100, 50, 20 and 10%).

spectra[33,34], thereby making it difficult to completely deconstruct the $Si_{2p}$ spectrum into Si-O and Si-C components. Although many of our films contain substantial quantities of carbon, we believe the Si is predominantly bonded to oxygen and that the carbon is present as Si-O-C, given the nature of the precursor. This is substantiated by the high resolution $C_{1s}$ spectra which indicate the presence of O-C/O=C moieties. Thus, for these films we assign Si-O to these peaks. In films with a very low percentage of carbon, but a small component peak in this area of the spectrum, we attribute the peak to Si-C. This is discussed more below. The more $Si(–O)_4$ present in a film suggests a more inorganic-like film, whereas more $Si(–O)_1$ and $Si(–O)_2$ suggests a more organic-like film. At higher $O_2$ concentrations, the film composition changed from more organic-like (high carbon content) to more inorganic-like (more stoichiometric $SiO_2$).

Films deposited from 100% HMDSO plasmas contain three $Si(–O)_x$ (x = 1-3) constituents, with $Si(–O)_1$ and $Si(–O)_2$ as the majority components. This composition suggests lower fragmentation of the monomer in the gas-phase of the plasma and higher incorporation of Si-C, given that the $Si(–O)_1$ and $Si(–O)_2$ peaks overlap with Si-C. Films deposited from 50% HMDSO plasmas contain $Si(–O)_2$ and $Si(–O)_3$, suggesting more fragmenting of the monomer, and less Si-C incorporation, consistent with the elemental composition data in Table 3.1. In contrast, films from 20% and 10% HMDSO plasmas only contain $Si(–O)_3$ and $Si(–O)_4$ components. The film from the 10% HMDSO plasma contains 98.6% $Si(–O)_4$, suggesting an almost complete conversion to a tetrahedral $SiO_2$ environment. Overall, this demonstrates that higher $O_2$ dilution produces a more inorganic-like film on the $TiO_2$ nanoparticles, consistent with previous results using these plasma systems.[29] Thus, the chemistry occurring on the nanoparticles is the same as that on flat Si and $ZrO_x$ wafers, and is highly dependent on gas feed composition.

High-resolution $Si_{2p}$ spectra of $SiO_2$ coated $TiO_2$ nanoparticles at $T_s$ = 400 and 500 K ($P$ = 50 W, deposition time = 10 min), Figure 3.6, reveal that film composition is also strongly dependent on substrate temperature. At $T_s$ = 400 K, the films produced from 10% HMDSO plasmas contain component peaks at 101.8 and 103.4 eV, corresponding to $Si(–O)_1$/Si-C and $Si(–O)_4$ environments, respectively. We believe the lower binding energy peak in this material is likely attributable to Si-C, rather than SiO species given the elemental composition data in Table 1 and the observation that at room temperature, the films are primarily composed of $Si(–O)_4$. Moreover, comparison of the spectra in Figs. 3.6a and 3.6b with their respective atomic compositions from Table 1 reveals that the carbon concentration approximately doubles, as does the component peak in the spectra. These data strongly suggest a correlation between this peak and the carbon content in these two films. In contrast, films produced from the 50% HMDSO plasma at $T_s$ = 400 K contain $Si(–O)_x$, (x = 1-3) components, with $Si(–O)_1$ and $Si(–O)_2$ being the majority components (~40.8% and ~45.7%, respectively). Note that this film composition is somewhat different from that observed for films deposited at room temperature, Figure 3.5b, but still suggests a change in film composition toward a more inorganic-like material at elevated $T_S$.

The XPS $Si_{2p}$ spectra for films produced at $T_S$ = 500 K from both 50% and 10% HMDSO plasmas contain peaks at 103.3 eV, suggesting the films are almost completely $SiO_2$, this agrees well with previous results from our laboratory for $SiO_2$ films deposited
from other alkoxysilane plasmas, which showed high $SiO_2$ content films were produced at elevated $T_S$.[17] Films produced from 10% HMDSO plasmas at $T_S$ = 500 K contain component peaks at 101.7 and 103.4 eV, corresponding to $Si(–O)_1$/Si-C and $Si(–O)_4$ environments, respectively. The film produced from the 50% HMDSO plasma at $T_s$ = 500 K contain component peaks at 102.1 and 103.4 eV, which correspond to $Si(–O)_2$ and $Si(–O)_4$ components, respectively. The

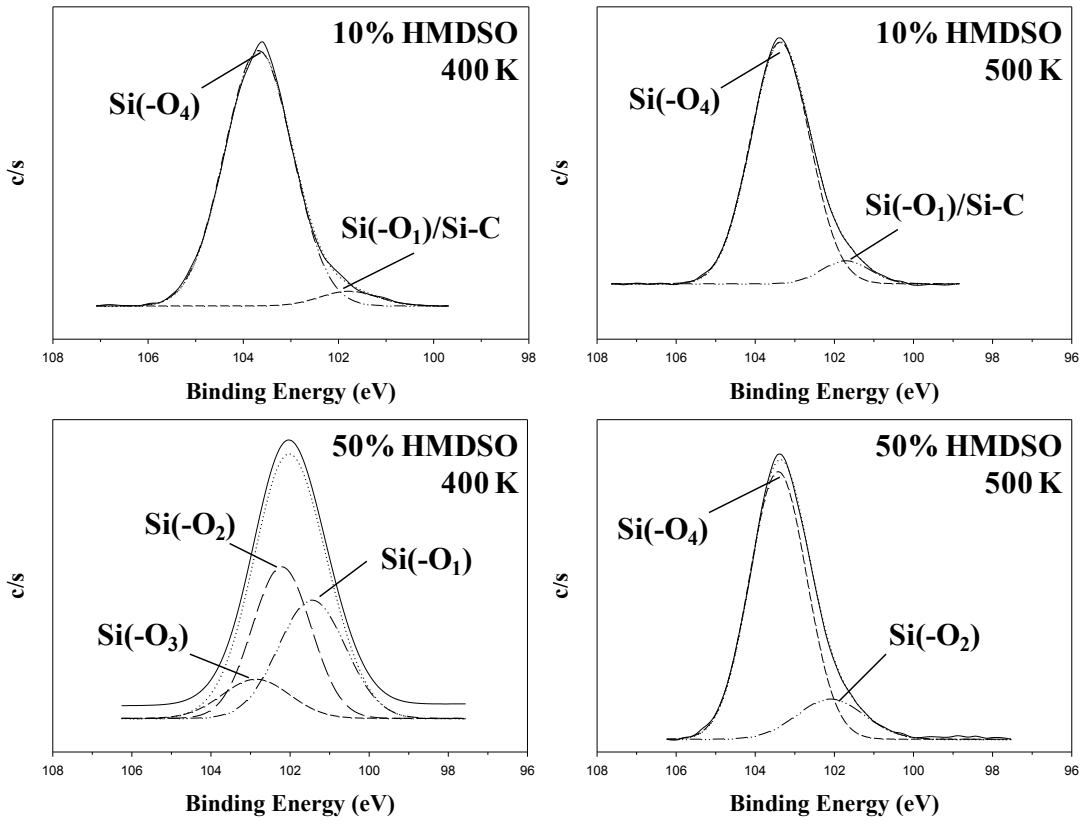


**Figure 3.6** XPS $Si_{2p}$ high-resolution spectra for films deposited from plasmas with a deposition time of 10 minutes and $P$ = 50 W with the specific HMDSO content in the feed shown (100, 50, 20 and 10%) and $T_S$ = 400 or 500 K.

$Si(–O)_2$ peak could also contain some Si-C, consistent with the film composition of the material deposited at 400 K, Table 3.1. Films produced from the 50% HMDSO plasma contain less $Si(–O)_4$ (85.0%) than those produced from 10% HMDSO plasmas (92.7%). This is not unexpected as the films produced in a 50% HMDSO plasma with $T_s$ = 300 K are highly organic in nature. Nonetheless, the elevated $T_S$ does serve to increase the inorganic nature of the deposited film.

As one additional note, the Figure 3.6 data clearly demonstrate that $T_S$ influences the film character. It appears, however, that changes caused by different feed gas composition are more dramatic than those resulting from a change in $T_S$. Previous work in our laboratories[19,32,34] indicated that the mechanism for PECVD of $SiO_2$ films involves fragmentation of the precursor molecule, adsorption to the substrate surface followed by diffusion, and then desorption. With higher oxygen concentrations, there are more O atoms that can react with adsorbed precursor fragments, decreasing the hydrocarbon content in the film, thereby forming more $SiO_2$-like coating on this new substrate, $TiO_2$. Thus, our data suggest that gas-phase mechanisms are more dominant in controlling the film composition than surface chemistry (i.e. diffusion of species).

As noted in Section 3.1, dispersion of $TiO_2$ composite nanoparticles can reveal whether a specific coating has significantly changed the surface properties of the nanoparticles, and thereby their interactions with other molecules, including solvent species. The use of plasmas to tailor the organic or inorganic nature of the film deposited onto $TiO_2$ nanoparticles allows for control over the surface properties of the composite nanoparticles produced. UV-vis spectroscopy can be employed to examine the dispersion properties of nanoparticles. Figure 3.7 shows UV-vis spectra for uncoated and $SiO_2$-coated (10% HMDSO plasma) $TiO_2$ nanoparticles dispersed in DI water, measured at 2 h intervals for 8 h. The spectra are characterized by a broad absorption

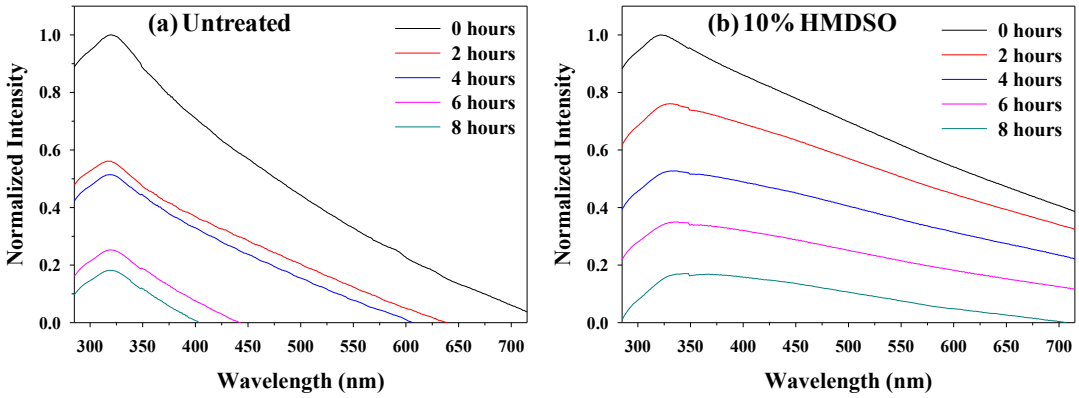


**Figure 3.7** UV-vis absorbance spectra for (a) untreated and (b) 10% HMDSO plasma-treated $TiO_2$ nanoparticles dispersed in DI water as a function of time from 0-8 h after sonication.

band centered at ~325 nm, and the maximum absorbance of this peak for both sets of data decrease over time.

To more directly compare these data for different nanoparticle samples, we have used the change in the maximum of the absorbance peak at ~325 nm to better quantify changes in dispersion of the nanoparticles. Plotted in Figure 3.8 are changes in the absorbance maximum [$\Delta_{abs}(\text{from } t_0) = A_{max}(t_0) - A_{max}(t_x)$, where $A_{max}(t_0)$ = the maximum absorbance at $t_0$ and $A_{max}(t_x)$ = the maximum absorbance at $t_x$, where x = 2, 4, 6, or 8 h] for uncoated and coated particles using 10%, 50%, and 100% HMDSO plasmas. For the coated materials, $\Delta_{abs}(\text{from } t_0)$ increases more slowly than that for the uncoated particles. Indeed, these data were fit with a linear regression and the slopes of these fits were found to be 0.115 ± 0.036, 0.0997 ± 0.0034, 0.0277 ± 0.0008, and 0.0248 ± 0.0069, for untreated and plasma-treated nanoparticles using 10, 50, and 100% HMDSO plasmas, respectively. The considerably larger error in the slope of the data for the untreated nanoparticles arises largely from the increase in error as the solutions age. A smaller increase in the rate of change in absorbance is indicative of a smaller decrease in the dispersion of the nanoparticles over time. In other words, the nanoparticles coated with the more inorganic-like material stay suspended in solution longer than the uncoated nanoparticles as well as the particles coated with films having more $SiO_2$-like character. The rates of change in the absorption for nanoparticles coated with the 50% and 100% HMDSO plasmas are very similar, which is consistent with the similarities in the film compositions produced from these two systems, Table 3.1. Thus, these data show the ability to stay suspended in solution is closely associated with surface chemistry, as expected.

Notably, our results from the UV-vis studies are somewhat counter-intuitive as one might expect the more organic-like materials to be less dispersed in DI water. However, given that the

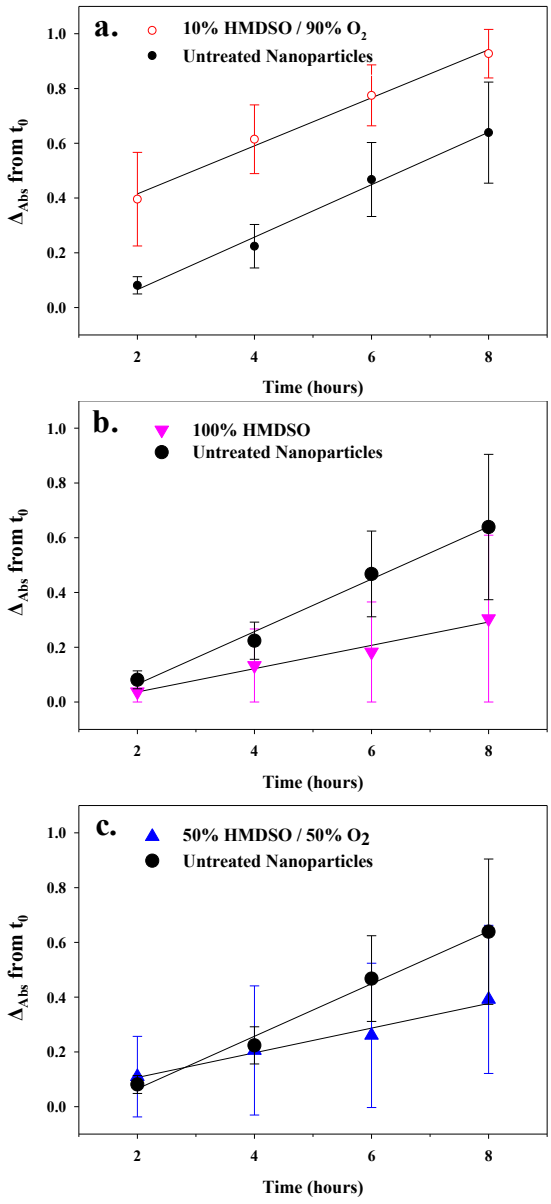


**Figure 3.8** Absorbance change from $t_0$ of the maximum absorption peak in the UV-vis spectrum for nanoparticles suspended in $H_2O$ as a function of time after sonication. Data are shown for untreated nanoparticles (each panel) and for nanoparticles coated using (a) 10%, (b) 50%, and (c) 100% HMDSO plasmas.

XPS compositional data suggest there is considerable C=O/C-O character to these films and that there may also be some Si-OH present, the materials are likely to be fairly hydrophobic in nature. Indeed, we have measured relatively low static water contact angles on both flat surfaces and substrates with nanoparticles deposited on them. Interestingly, recent reports of PECVD coating of Cu nanoparticles, polylactic acid grafting of $TiO_2$, and fluoroalkyl-coated ZnO nanocomposites also suggests that a range of polymeric coatings can assist in dispersion of metal or metal oxide nanoparticles in a variety of solvents and that the dispersion properties of the composite materials do not necessarily conform to expected properties.[41-43] Notably, a recent report on the creation of Bragg reflectors from nanoparticle suspensions suggests that the ability to create stable nanoparticle suspensions could significantly improve production of photonic crystals.[44]

**3.2.2. Hexylamine Films.** To examine the creation of a nitrogen-containing polymer coating on the $TiO_2$ nanoparticles, we used a pulsed HexAm plasma ($P$ = 50 W, 10% d.c., and 30 min deposition time) to create an organic polymeric material with amine functionality.[9] High-resolution XPS spectra reveal the film's composition to be 57.0 ± 1.4% C, 25.0 ± 2.3% O, 10.2 ± 1.2% Ti, and 7.4 ± 0.5% N. The higher level of Ti in the XPS analysis relative to that observed with the $SiO_2$ deposition systems is indicative of the much lower deposition rate in the HexAm system (≤350 Å/min for flat substrates)[9]. Figure 3.9 shows the charge-corrected $C_{1s}$ spectrum for HexAm films deposited on $TiO_2$ nanoparticles. As noted above, for these materials we used the $TiO_2$ Ti 2p peak (458.8 eV) as the reference peak.[37] Thus, the $C_{1s}$ peak is slightly shifted from that of the films deposited using the HMDSO plasmas, as evidenced by the deconstruction of this peak, which reveals three components at 284.4, 285.5, and 287.2 eV. The peak at 284.4 eV was assigned to C-C/C-H (hydrocarbon), whereas the component at 285.5 eV contains contributions from C-N that may include primary, secondary, or tertiary amine groups; C=N (imine groups);

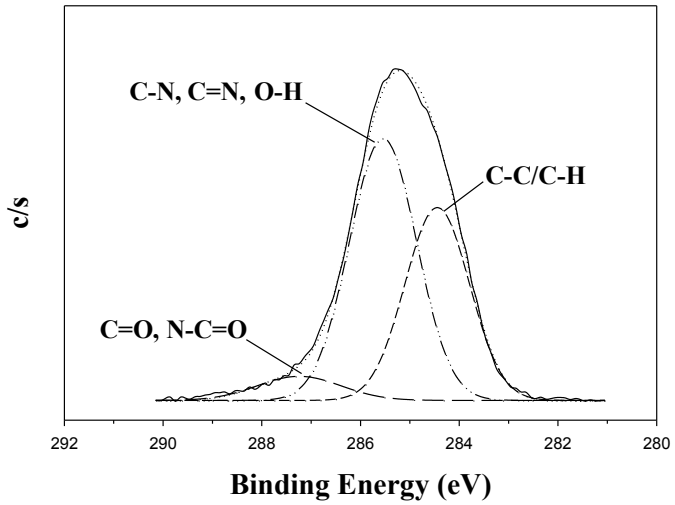


**Figure 3.9** XPS $C_{1s}$ high resolution spectra for films deposited from pulsed HexAm plasmas with a peak applied rf power of 150 W, 10% duty cycle and 30 min deposition time.

and C-O. The component peak at 287.2 eV corresponds to C=O (carbonyl) and N-C=O (amide). A peak for Ti-C was not observed. These data are consistent with data for plasma-polymerized HexAm films deposited on flat substrates previously reported.[9] Similar to the results in the HMDSO systems, the lack of dependence of film composition on substrate type or morphology indicates that the chemistry occurring during HexAm film depositions is controlled primarily by gas-phase reactions and not surface interactions.

Figure 3.10 shows SEM images of untreated (Fig. 3.10a) and HexAm plasma-treated (Fig. 3.10b) $TiO_2$ nanoparticles. It is evident that, similar to the HMDSO systems, the HexAm films conformally coat the nanoparticles and do not cause significant morphological changes to the nanoparticles. The presence of Ti in the compositional analysis of the film is indicative of deposition of a very thin layer as expected given the relatively low deposition rate in this system. The use of HexAm to deposit a coating on the $TiO_2$ nanoparticles demonstrates, however, that our PECVD process is viable for deposition of films with a variety of compositions. These results clearly demonstrate that the underlying substrate does not strongly influence film chemistry in either the $SiO_2$ or HexAm deposition systems.

A transmission electron microscope (TEM) image of $TiO_2$ nanoparticles coated in a HexAm plasma is shown in Figure 3.11. This supports the conformal nature of the HexAm treated nanoparticles that was observed in the SEM images. TEM images of $TiO_2/SiO_2$ composite nanoparticles were also obtained but were ambiguous because of the similarities of the two materials and instrument limitations.

The performance of the HexAm/$TiO_2$ composite nanoparticles was tested in the same manner as the $SiO_2$ coated nanoparticles. Figure 3.12 shows changes in the absorbance maximum for uncoated and HexAm plasma-treated $TiO_2$ nanoparticles. The slope of the

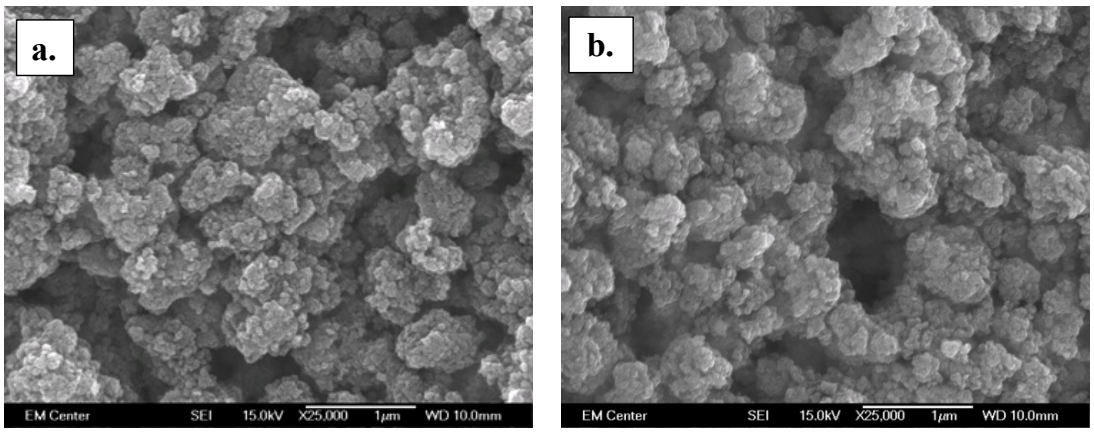


**Figure 3.10** SEM images of (a) uncoated $TiO_2$ nanoparticles on a Si wafer and (b) $TiO_2$ nanoparticles plasma treated using a pulsed HexAm plasma (10% d.c.), with the conditions given in Figure 3.9.

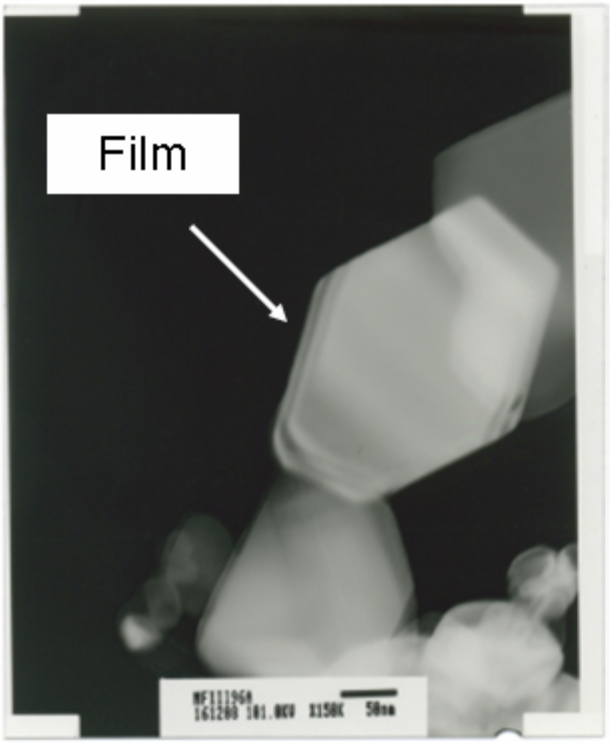


**Figure 3.11** TEM image of $TiO_2$ nanoparticles plasma treated using a pulsed HexAm (10% d.c.), with conditions given in Figure 3.9.

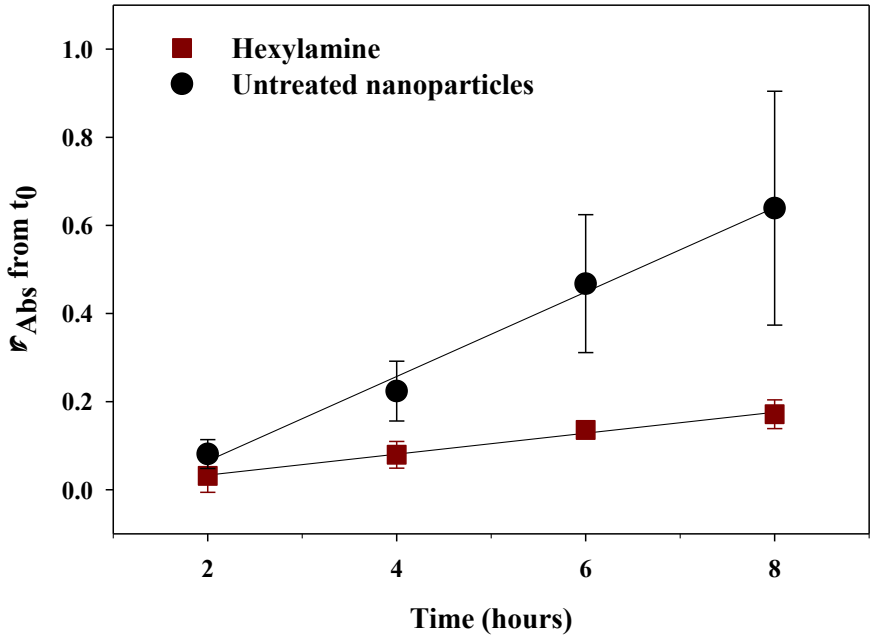


**Figure 3.12** Absorbance change from $t_0$ of the maximum absorption peak in the UV-vis spectrum for nanoparticles dispersed in $H_2O$ as a function of time after sonication. Data are shown for untreated nanoparticles and for nanoparticles coated using a pulsed HexAm plasma with the conditions given in Figure 3.9.

plasma-polymerized HexAm coated nanoparticles is 0.0223 ± 0.0019, considerably less than that for the untreated nanoparticles, and very similar to those measured for the 100% and 50% HMDSO plasma-treated nanoparticles. Again, this indicates that the nanoparticles coated with a coating having high organic content stay dispersed in solution longer than untreated nanoparticles. This further demonstrates how PECVD coatings can alter the properties of the underlying material, and potentially improve the performance of these materials in a variety of applications requiring the suspension of these particles.

### 3.3 Summary

Films deposited on $TiO_2$ nanoparticles are similar to those deposited previously on flat Si substrates for both the HMDSO/$O_2$ plasmas and the HexAm system. The data presented here demonstrate that a variety of films can be produced using different monomers and that nanoparticles can be conformally coated, regardless of the deposition system. Feed gas composition can be used to control film composition. The parameters used to tailor the composition of the film when using HMDSO as a precursor were oxidant concentration and substrate temperature. With increased oxidant addition to the gas feed, more $SiO_2$-like films were produced. Similarly, elevated $T_S$ experiments produced films with more inorganic-like nature. Suspension of the $TiO_2$ nanoparticles in DI water showed that the composite nanomaterials all stayed dispersed in solution for longer periods of time, regardless of the coating. Notably, films with more organic-like coating stayed suspended longer than those with a more inorganic nature.

REFERENCES


[1] L. Bokobza, Polymer. **48**, 4907 (2007).
[2] X. Cao, C. M. Li, H. Bao, Q. Bao and H. Dong, Chem. Mater. **19**, 3773 (2007).
[3] V. V. Kuznetsov, A. A. Kalinkina and T. V. Pshenichkina, J. Electrochem. **43**, 776 (2007)
[4] M. W. Hooker, K. S. Kano and M. W. Stewart, IEEE Trans. Appl. Superconduct. **17**, 1521(2007).
[5] B. Cho, T. W. Kim, M. Choe, G. Wang, S. Song and T. Lee, Org. Electronics. **10**, 473 (2009).
[6] Y. Kotoku, J. Kato, G. Akashi, Y. Hirai and K. Ishihara, Laser Phys. Lett. **6**, 388, (2009).
[7] K. T. Thurn, E. M. B. Brown, A. Wu, S. Vogt, B. Lai, J. Maser, T. Paunesku and G. E. Woloschak, Nanoscale Res. Lett. **2**, 430 (2007).
[8] C. I. Butoi, N. M. Mackie, L. J. Gamble, D. G. Castner, J. Barnd, A. M. Miller and E. R. Fisher, Chem. Mater. **12**, 2014 (2000).
[9] G. S. Malkov, I. T. Martin, W. B. Schwisow, J. P. Chandler, B. T. Wickes, L. J. Gamble, D. G. Castner and E. R. Fisher, Plasma Process. Polym. **5**, 129 (2008).
[10] N. M. Mackie, N. F. Dalleska, D. G. Castner and E. R. Fisher, Chem. Mater. **9**, 349 (1997).
[11] N. M. Mackie, D. G. Castner and E. R. Fisher, Langmuir. **14,** 1227 (1998).
[12] P. R. McCurdy, J. M. Truitt and E. R. Fisher, J. Vac. Sci. Technol. A **17**, 2475 (1999).
[13] P. R. McCurdy, J. M. Truitt and E. R. Fisher, J. Electrochem. Soc. **145**, 3271, (1998).
[14] F. Zhu, E. S.-W. Kong, J. Zhang and Y. Zhang, Chem. Phys. Lett. **423**, 270 (2006).
[15] J. Cho, F. S. Denes and R. B. Timmons, Chem. Mater. **18**, 2989 (2006).
[16] M. Drabik, J. Hanus, J. Kousal, A. Choukourov, H. Biederman, D. Slavinska, A. Macko-va and J. Pesicka, Plasma Process. Polym. **4**, 654 (2007).
[17] K. H. A. Bogart, S. K. Ramirez, L. A. Gonzales, G. R. Bogart and E. R. Fisher, J. Vac. Sci. Technol. A **16**, 3175 (1998).
[18] M. Godek, G. S. Malkov, E. R. Fisher and D. Grainger, Plasma Process. Polym. **3**, 485 (2006).
[19] M. L. Steen, W. C. Flory, N. E. Capps and E. R. Fisher, Chem. Mater. **13**, 2749 (2001).
[20] J. Zhou and E. R. Fisher, J. Nanosci. Nanotechnol **4**, 539 (2004).
[21] A. Teleki, M. Suter, P. R. Kidambi, O. Ergeneman, F. Krumeich, B. J. Nelson and S. E. Pratsinis, Chem. Mater. **21**, 2094 (2009).
[22] D. K. Yi, S. S. Lee, G. C. Papaefthymiou and J. Y. Ying, Chem. Mater. 18, 614 (2006).
[23] E. Angelini, R. d'Agostino, F. Fracassi, S. Grassini and F. Rosalbino, Surf. Interface Anal. **34**, 155 (2002).
[24] B. Borer, A. Sonnenfeld and P. R. von Rohr, Surf. Coat. Technol. **201**, 1757 (2006).
[25] P. Bruno, G. Cicala, F. Corsi, A. Dragone and A. M. Losacco, Sensors Act. B **100**, 126 (2004).
[26] M. Creatore, Y. Barrell, J. Benedikt and M. C. M. van de Sanden, Plasma Sources Sci. Technol. **15**, 421 (2006).
[27] D. Magni, C. Deschenaux, C. Hollenstein, A. Creatore and P. Fayet, J. Phys. D.: Appl. Phys. **34**, 87 (2001).

[28] M. Simor, A. Fiala, D. Kovacik, P. Hlidek, A. Wypkema and R. Kuipers, Surf. Coat. Technol. **210**, 7802 (2007).
[29] D. S. Wavhal, J. Zhang, M. L. Steen and E. R. Fisher, Plasma Process. Polym. **3**, 276 (2006).
[30] L. Zajickova, V. Bursikova, Z. Kucerova, J. Franclova, P. Stahel, V. Perina and A. Mackova, J. Phys. Chem. Solids **68**, 1255 (2007).
[31] L. Zajickova, V. Bursikova, Z. Kucerova, D. Franta, P. Dvorak, R. Smid, V. Perina and A. Mackova, Plasma Sources Sci. Technol. **16**, S123 (2007).
[32] K. H. A. Bogart, N. F. Dalleska, G. R. Bogart and E. R. Fisher, J. Vac. Sci. Technol. A **13**, 476 (1995).
[33] K. L. Williams and E. R. Fisher, J. Vac. Sci. Technol. A **21**, 1688 (2003).
[34] J. Zhang, D. S. Wavhal and E. R. Fisher, J. Vac. Sci. Technol. A **22**, 201 (2004).
[35] M. Hahnel, V. Bruser, H. Kersten, Plasma Process. Polym. **4**, 629 (2007).
[36] D.J.V. Pulsipher, E.R. Fisher, Surf. Coat. Technol. **203**, 2236 (2009).
[37] L. Ge, M.X. Xu, H.B. Fang, Thin Solid Films **515**, 3414 (2007).
[38] H. Lindstrom, A. Holmberg, E. Magnusson, L. Malmqvist, A. Hagfeldt, J. Photochem. Photobiol. A **145**, 107 (2001).
[39] P.R. McCurdy, L.J. Sturgess, S. Kohli, E.R. Fisher, Appl. Surf. Sci. **233**, 69 (2004).
[40] J.F. Moulder, W.F. Stickle, P.E. Sobol, K.D. Bomben, *Handbook of X-ray Photoelectron Spectroscopy*, Physical Electronics, Inc., Eden Prairie, MN, 1995.
[41] R. Lahoz, J.P. Espinos, G.F. de la Fuente, A.R. Gonzalez-Elipe, Surf. Coat. Technol. **202**, 1486 (2008).
[42] S. Mahl, M. Neumann, V. Schlett, A. Baalmann, Surf. Interface Anal. **26**, 204 (1998).
[43] I.T. Martin, B. Dressen, M. Boggs, Y. Liu, C.S. Henry, E.R. Fisher, Plasma Process. Polym. **4**, 414 (2007).
[44] M.L. Steen, L. Hymas, E.D. Havey, N.E. Capps, D.G. Castner, E.R. Fisher, J. Membr. Sci. **188**, 97 (2001).
[45] M.R. Alexandar, R.D. Short, F.R. Jones, W. Michaeli, C.J. Blomfield, Appl. Surf. Sci. **137**, 179 (1999).
[46] J. Tavares, E.J. Swanson, S. Coulombe, Plasma Process. Polym. 5 (2008)
[47] K. Sasazawa, Y. Hirayama, H. Sawada, Polym. Int. **58**, 177 (2009).
[48] Y.-B. Luo, X.-L. Wang, D.-Y. Xu, Y.-Z. Wang, Appl. Surf. Sci. **255**, 6795 (2009).
[49] D.P. Puzzo, L.D. Bonifacio, J. Oreopoulos, C.M. Yip, I. Manners, G.A. Ozin, J. Mater. Chem. **19**, 3500 (2009).

# CHAPTER 4

# ENHANCING SURFACE FUCTIONALITY OF SUPPORTED $Fe_2O_3$ NANOPARTICLES USING PULSED PLASMA DEPOSITION OF ALLYL ALCOHOL

This chapter details work published in an invited letter in *Nanoscience and Nanotechnology Letters* written by Jeffrey C. Shearer and Ellen R. Fisher. The studies focus on maximizing surface –OH functionality on supported $Fe_2O_3$ through the use of pulsed plasmas. A variety of surface analysis techniques are used to show that lower duty cycle plasmas produced thin films with a higher concentration of –OH functional groups than films produced under continuous wave plasma conditions.

## 4.1 Introduction

The use of composite magnetic nanomaterials in biological applications (i.e. site specific drug delivery,[1] MRI contrast agents[2]) has grown rapidly in recent years.[3] Using nanoparticles in biomedical applications presents several challenges including concerns regarding the potential toxicity of nanoparticles in both biological systems and the environment.[4] A potential solution to this issue is creation of a barrier film on the nanoparticle surface. Additionally, for nanoparticles to be the most effective in the widest range of potential applications, a critical need exists for the ability to specifically adjust particle surface chemistry.[5] Indeed, nanoparticle interactions with their environment (e.g. a biological system) are directly tied to the type of chemistry that can occur at the nanoparticle surface.[6] Thus, optimal nanoparticle performance can be realized by tai-

loring surface functionality and properties such as wetting (hydrophilicity), protein and drug attachment, and surface energy.[7, 8]

Plasma processing for the production of biocompatible nanomaterials and tailoring of surface properties provides an alternative to traditional wet chemical surface modification strategies that could damage or destroy nanostructured materials.[3] Use of pulsed plasma power for plasma polymerization schemes provides additional protection from substrate damage and has been shown to increase monomer retention in the deposited films.[9-14] Moreover, plasma polymerization offers virtually no limitations on monomer selection, does not require high substrate temperatures, and can involve almost any type and size of substrate. Indeed, we have successfully modified a range of different types of substrates, including membranes,[15, 16] fibers,[17, 18] nanowires,[19, 20] particles,[21] and microfluidic channels.[22] With the appropriate monomer selection and plasma parameters, an array of different functionalities can be imparted to a surface, including amine ($–NH_2$),[23, 24] alcohol (–OH),[25] and carboxylic acid (–COOH)[23, 26] groups. Implantation of hydroxyl groups is of particular interest especially for biological applications as water solubilization is an important step for use under physiological conditions.[27]

One monomer that effectively implants OH functionality, especially under pulsed plasma conditions, is allyl alcohol (allylOH).[28] The plasma environment can fragment allylOH into radicals (primary species for deposition) without the need for monomer or substrate heating.[29] Moreover, selection of conditions that retain more of the parent monomer can be utilized to produce OH-rich plasma polymerized allylOH films (*pp*-allylOH). Deposition of *pp*-allylOH can occur in both continuous wave (CW) and pulsed plasmas. Operating in a CW mode typically generates a high-energy, high density plasma environment that results in significant monomer fragmentation and produces films with a high degree of crosslinking. Because the plasma is only

on for a portion of the total pulse cycle, pulsed plasma environments can effectively mimic the low-power conditions needed for retention of the monomer species. Small molecular weight monomers can become activated without destroying their chemical functionality. Because polymerization occurs in both the "on" and "off" times, radical species can exist in the "off" time and largely contribute to retaining the monomer functionality during deposition.[9, 30-35]

O'Toole and Short have provided comprehensive studies of allylOH plasmas to help elucidate formation mechanisms of deposited films.[36, 37] Their reaction schemes suggest that cationic allylOH oligomers formed via electron impact reactions are the primary source for the deposition of OH-rich films. Fahmy and coworkers[25] explored pulsed allylOH plasma systems and reported a decrease in OH functionality with increasing plasma d.c., based on X-ray photoelectron spectroscopy (XPS) and Fourier transform infrared spectroscopy (FTIR) data. Likewise, Timmons and coworkers used pulsed allylOH plasmas to produce gas separation membranes with high OH content.[12] To date, however, deposition of *pp*-allylOH films onto nanoparticle surfaces has not been explored. Here, we have used pulsed allylOH plasmas to create OH-rich films on $Fe_2O_3$ nanoparticles. In addition, we provide insight into film formation and gas-phase mechanisms for the deposition of *pp*-allylOH films.

**4.2 Results and Discussion**

Unless otherwise indicated, depositions in this chapter were performed with a total system pressure of 70 mTorr, applied rf power of 50 W and deposition time of 10 minutes. For pulsed plasma depositions, the plasma power was pulsed with d.c. = 2-100%, with 100% d.c. indicating CW plasma conditions.

All analyses were performed on *pp*-allylOH coated $Fe_2O_3$ nanoparticles unless otherwise indicated. Average deposition rates for *pp*-allylOH films were measured using variable angle spectroscopic ellipsometry (VASE, J.A. Woolam Co., Inc.). Samples used for deposition rate measurements comprised *pp*-allylOH films deposited on Si wafers and yielded values of ~9 nm/min for 10% d.c. allylOH plasmas and ~15 nm/min for CW allylOH plasmas. For nanoparticle substrates, determinations of deposition rate were made from scanning electron microscopy (SEM) images and were not appreciably different from the deposition rates measured on Si wafers using VASE.

Key elements to successfully functionalizing the surface of $Fe_2O_3$ nanoparticles for specific applications are the precise control of film composition and the ability to conformally coat unusually shaped particles such that their general size and shape are maintained. Figure 1a shows an XPS survey spectrum and associated SEM image for an untreated $Fe_2O_3$ nanoparticle substrate. As can be seen from XPS and SEM, the preparation of the nanoparticles (i.e. suspension and coating on a Si wafer) does not appreciably change the morphology of the particles nor does it change the surface composition of the particles, as the primary signals observed arise from Fe and O, with a small contribution from adventitious carbon.

XPS compositional data reveal an increasing O/C ratio with decreasing d.c., Figure 4.1b. Films deposited in CW plasmas have an O/C ratio of $0.17 \pm 0.0003$. To maximize the functional group density on the nanoparticle surface, a stoichiometrically equivalent number of O atoms needs to be in the film as there are in the monomer (i.e. O/C = 0.34 for allylOH). The XPS data show that an extremely low d.c. plasma (2%) produces films with an O/C ratio stoichiometrically equivalent to the allylOH monomer, $0.34 \pm 0.0004$. Optimization studies in our lab have shown that 5 cm downstream from the plasma coil region is ideal for matching this ratio. Thus, all data

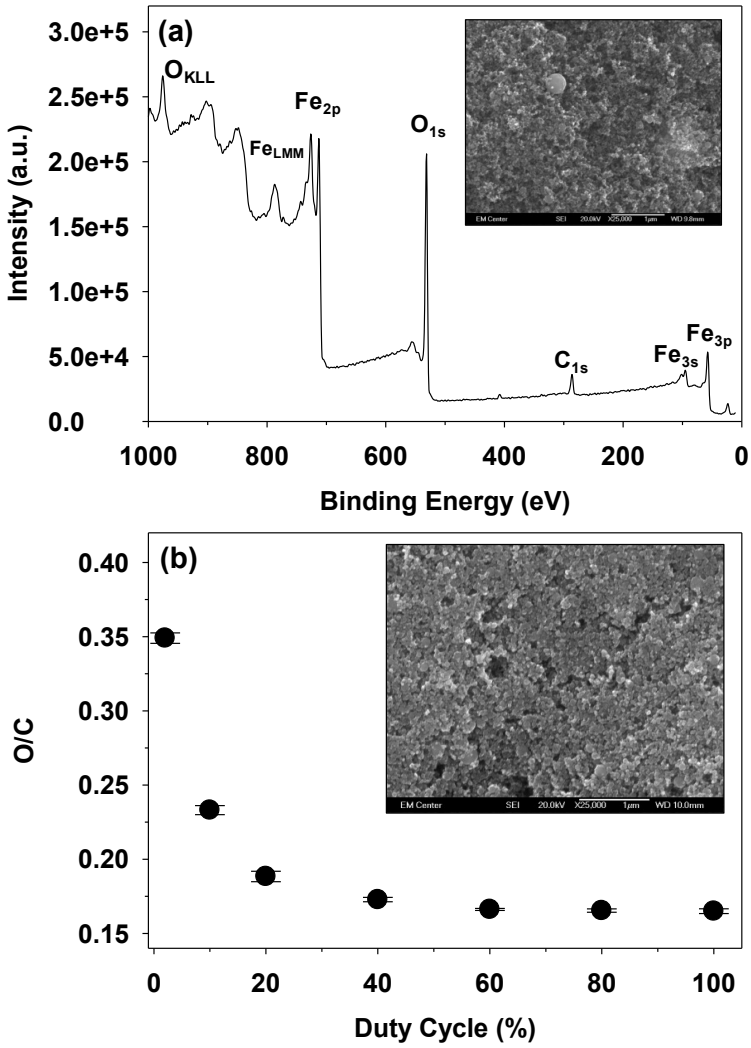


**Figure 4.1.** (a) XPS survey spectrum of untreated, as-purchased, $Fe_2O_3$ nanoparticles. The inset contains an SEM image (scale = 1 μm) of the $Fe_2O_3$ nanoparticle substrate prepared as described in the text. (b) O/C ratio of *pp*-allylOH films calculated from XPS compositional data as a function of duty cycle. The inset is an SEM image (scale = 1 μm) for $Fe_2O_3$ nanoparticles coated using a 10% d.c. allylOH plasma. This image is representative of results for particles coated under all d.c. conditions.

reported here were for substrates placed in this location. Furthermore, deposition of *pp*-allylOH from all pulsed plasmas does not appreciably change the size or shape of the underlying nanoparticles (Fig. 4.1b inset), which is key to their viability in biological applications.

High-resolution $C_{1s}$ XPS spectra for *pp*-allylOH coated $Fe_2O_3$ nanoparticles are shown in Figure 4.2 for depositions utilizing different duty cycles. Deconvolution of each $C_{1s}$ spectrum reveals that the primary binding environment ($\gtrsim$ 70 %) for all films deposited in allylOH plasmas is C-C/C-H (B.E. = 284.6 eV), with smaller contributions from C-O(-R) and O-C(-R)-O (B.E. = 286.3 and 288.2 eV, respectively) environments. Decreasing the plasma d.c. from CW to 10% causes shifts in the relative intensities of $C_{1s}$ binding environments as contributions from oxygen-containing moieties dramatically increase, consistent with the O/C ratio data shown in Figure 4.1b. Specifically, as more oxygen is incorporated into the deposited film, the contributions from C-O(-R) and O-C(-R)-O binding environments increase. For films deposited under CW conditions, the C-O(-R) and O-C(-R)-O moieties represent ~22% of the total $C_{1s}$ binding-environments, whereas these binding environments comprise ~ 30% of the $C_{1s}$ spectra for films deposited in a 10% d.c. plasma.

To further evaluate the functional group contributions in the deposited films, complementary FTIR data were collected for *pp*-allylOH films deposited on Si substrates at different d.c., Figure 4.3. These spectra are similar to those reported recently by Fahmy et al. for films deposited in pulsed allylOH plasmas.[25] Spectra for all three films exhibit features characteristic of the allylOH monomer, including C=O and C-O stretches at ~1650 $cm^{-1}$ and ~1050 $cm^{-1}$, respectively, and C-$H_x$ wag and OH deformation bands at ~1450 and ~1370 $cm^{-1}$.[41] Notably, as the d.c. decreases, the C=O and C-O absorption peaks increase, suggesting additional oxygen moieties are incorporated at lower d.c., consistent with the XPS data. Two of the prominent features in

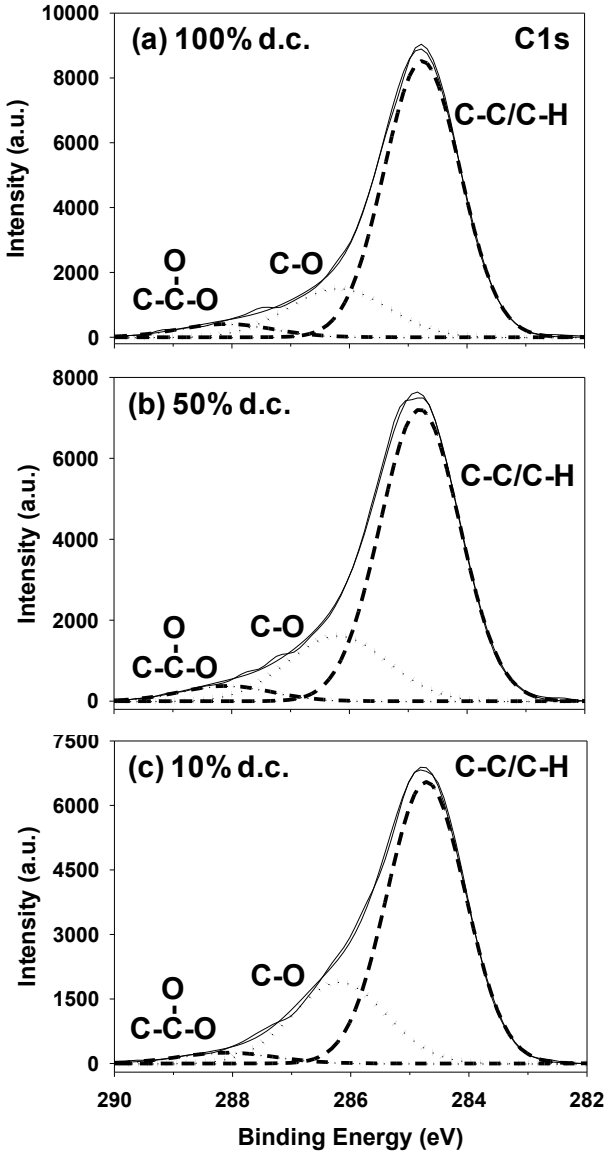


**Figure 4.2.** High-resolution $C_{1s}$ XPS spectra of *pp*-allylOH coated $Fe_2O_3$ nanoparticles produced using (a) 100%, (b) 50%, and (c) 10% d.c. plasmas.

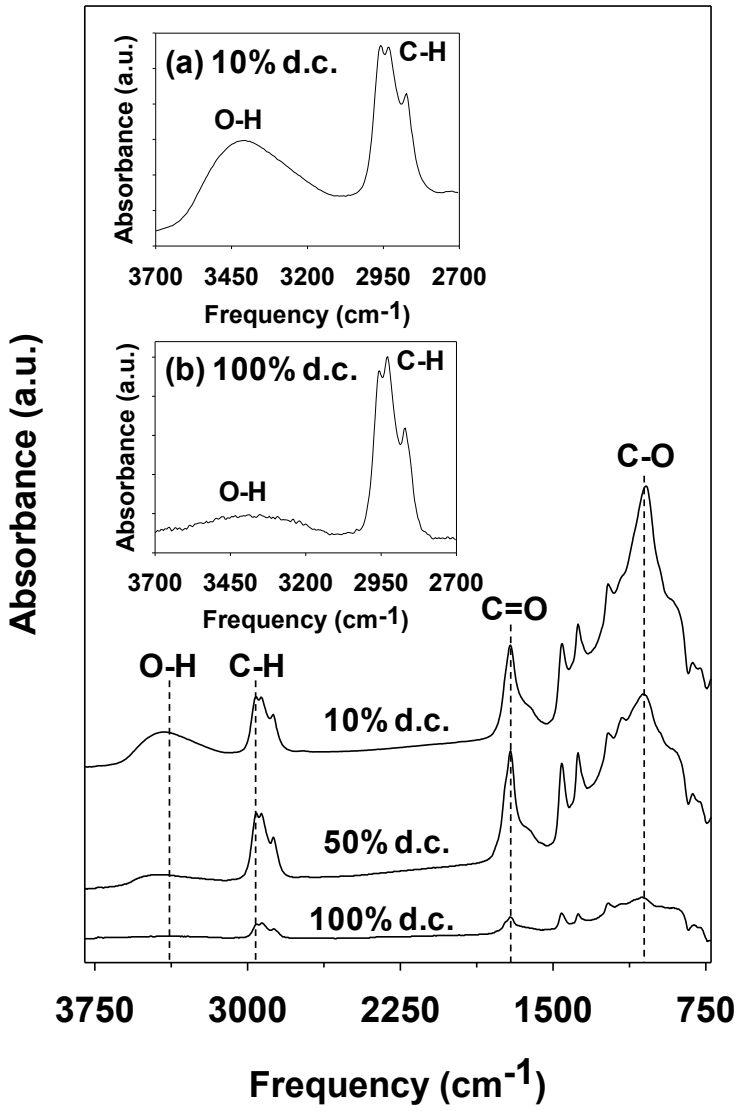


**Figure 4.3.** FTIR spectra for *pp*-allylOH coated Si wafers deposited in plasmas with d.c. = 10%, 50%, and 100%. The dotted lines indicate the O-H, C-H, C=O, and C-O stretch vibrations. The inset contains an enlarged view of the 2700-3700 $cm^{-1}$ spectral region for films deposited in 10% and 100% d.c. plasmas, highlighting changes in the O-H and C-H stretches.

these spectra are the $sp^3$ C-H stretch at ~2900 $cm^{-1}$ (containing contributions from $CH_x$ (x = 1-3) moieties) and the broad O-H absorbance band centered at ~3400 $cm^{-1}$. As plasma d.c. decreases from CW to 10%, the intensity of the O-H stretching vibration dramatically increases, relative to the C-H stretching peak, suggesting that the alcohol functionality contained within the films increases concomitantly. The insets show enlargements of the 2700-3700 $cm^{-1}$ region for clarification. These data, combined with XPS results (Figure 4.1), confirm that as the plasma d.c. decreases, more alcohol functionality is implanted onto the nanoparticle surface. This agrees well with the findings of Fahmy, et al. who also observed a significant increase in OH functionality at the lowest d.c. in their system.[25]

To further explore the deposition mechanisms involved in functionalizing nanoparticle surfaces, AOES data were collected for pulsed allylOH plasmas at different duty cycles. The raw OES spectra for CW and 20% d.c. allylOH plasmas, shown in Figure 4.4 (insets), exhibit emission signals at ~308, ~389, ~656, and ~820 nm, corresponding to emission from OH, CH, $H_\alpha$, and O, respectively.[24, 40] Although all four of these species are observed under all conditions, the dominant emitting species change as a function of d.c., Figure 4.4. Specifically, the relative densities of both H atoms and OH radicals in the plasma increase as the d.c. increases. In contrast, the gas-phase density of CH radicals and O atoms correlate inversely with d.c. In the CW plasmas (100% d.c.), the H atom density is the highest of the four species considered. This is likely the result of the first step of fragmentation of the parent molecule, as described by Short and coworkers, reaction (4.1).[36] Subsequent fragmentation proceeds via loss of $H_2O$ to form a cyclic $C_3H_3$ radical [c-$(CH)_3$], reaction (4.2). Decomposition of these two reaction products leads to formation of OH and CH radicals, processes (4.3) and (4.4), respectively. Further decomposition of OH produces oxygen atoms and additional hydrogen atoms.

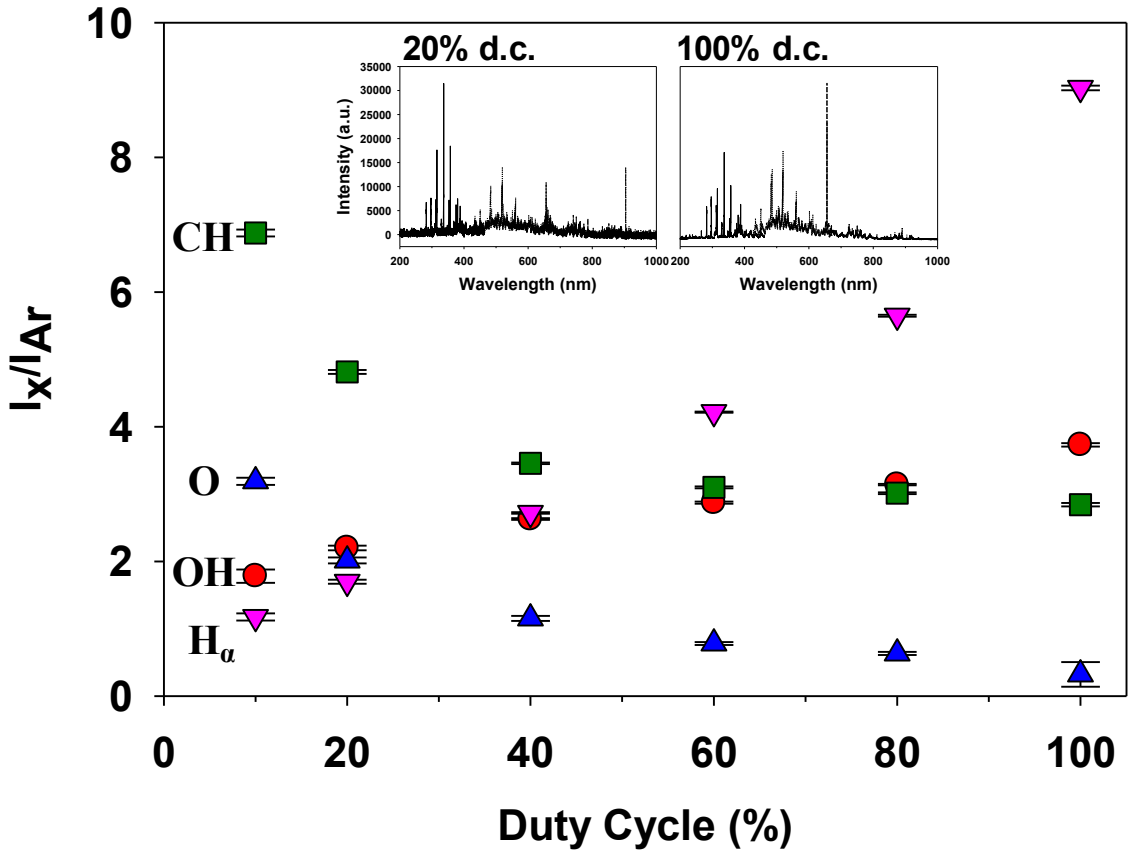


**Figure 4.4.** AOES data showing relative gas-phase CH (■), OH (●), O (▲), and $H_\alpha$ (▼) densities as a function of plasma duty cycle. Insets show raw spectra for 20% and 100% d.c. plasmas.

$$CH_2{=}CH{-}CH_2{-}OH + e^- \rightarrow H + [CH_2{=}CH{-}CH{=}OH \leftrightarrow CH_2{-}CH{=}CH{-}OH] + e^- \quad (4.1)$$

$$CH_2{=}CH{-}CH{=}OH \leftrightarrow CH_2{-}CH{=}CH{-}OH \rightarrow H_2O + c\text{-}(CH)_3 \quad (4.2)$$

$$H_2O \rightarrow OH + H \rightarrow O + 2H \quad (4.3)$$

$$c\text{-}(CH)_3 \rightarrow 3\ CH \quad (4.4)$$

At the lowest d.c., CH is the more dominant species, with significant contributions from O atoms and much smaller densities of OH and H atoms. The longer off times in low d.c plasmas allows for additional decomposition of the species formed from initial electron impact dissociation of the monomer. Specifically, unstable c-$(CH)_3$ species can decompose in the off cycle of low d.c. plasmas, process 4.4, which accounts for the higher CH signal at these conditions. Additionally, as species in high d.c. plasmas undergo more collisions (potentially resulting in excitation and/or decomposition), excited state CH radicals could be quenched, leading to lower AOES signals for CH* under CW conditions. Effectively, in pulsed plasmas, the four steps shown in processes 4.1-4.4 can go to completion during pulse off times without additional formation of reactants. The relatively high OH and H signals at high d.c. conditions indicate that the dissociation of water can occur even under these conditions. Furthermore, a higher [OH] at high d.c. suggests further dissociation of the parent monomer. This is substantiated by the higher OH content found in the *pp*-allylOH film at low d.c. Likewise, low d.c. films exhibit similar stoichiometry as the parent monomer, suggesting less overall dissociation of the parent molecule. Additional AOES experiments found no pressure dependence for plasma species densities.

As a primary goal of this research is to create biocompatible nanomaterial surfaces, and hydrophilicity is a key factor in determining biocompatibility, the hydrophilicity of the plasma treated nanoparticles was tested using contact angle goniometry. Figure 4.5 shows time-resolved images collected during the first 15 sec after a 2 μL water drop was placed on the surface of the nanoparticles. The images obtained using films deposited in a 10% d.c. plasma are

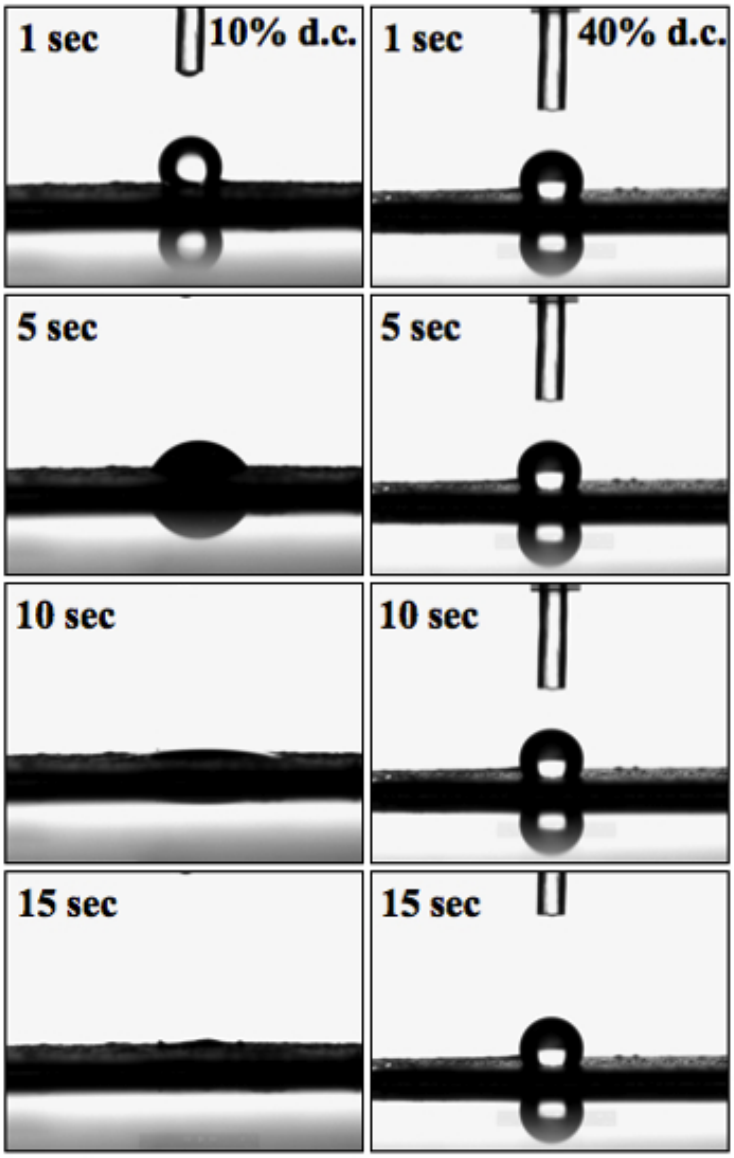


**Figure 4.5.** Time-resolved photographs of water drops interacting with *pp*-allylOH coated $Fe_2O_3$ nanoparticles deposited in pulsed plasmas with d.c. = 10% (left column) and 40% (right column), showing the relative contact angles of the nanoparticle substrates.

representative of all films created in plasmas with d.c ≤ 20%, whereas the images for films deposited with a 40% d.c. are representative of films created in plasmas with d.c. > 20%. For all films deposited in low d.c. plasmas (≤ 20%), water droplets were absorbed by the nanoparticles in under 15 sec. For films deposited in higher d.c. plasmas (> 20%), water droplets did not absorb onto the nanoparticle substrate. Moreover, a water contact angle of ~116° was observed for > 10 min (or until evaporation) on the surface of the nanoparticle substrates treated in high d.c. plasmas. Although the surface morphology of a substrate can affect the measured contact angle, we do not observe significant differences in morphology between samples coated under different plasma processing conditions. Thus, we attribute the behavior of the water drops to the relative concentration of OH in the *pp*-allylOH films. As described above, XPS and FTIR data confirm that films deposited under low d.c. conditions contain larger concentrations of oxygen in the form of hydroxyl groups, thereby creating more hydrophilic materials.

### 4.3 Summary

In summary, we have used pulsed plasma polymerization to conformally coat supported $Fe_2O_3$ nanoparticles. As the d.c. decreases, the OH content in the pp-allylOH films deposited increases, as does the hydrophilicity of the film. AOES data suggest the gas-phase composition of the plasma in CW plasmas (100 % d.c.) is dominated by the products of the first steps in monomer decomposition, H atoms and OH radicals, whereas at the lowest d.c., the increased off time allows the initial products to decompose further (to O atoms and CH radicals) before they are replenished by the next plasma pulse. Future studies will include alternate reactor designs to coat freestanding nanoparticles and additional coatings designed to promote biocompatibility.

REFERENCES


[1] B. Chertok, B. A. Moffat, A. E. David, F. Q. Yu, C. Bergemann, B. D. Ross and V. C. Yang, Biomaterials **29**, 487 (2008).

[2] A. Petri-Fink, M. Chastellain, L. Juillerat-Jeanneret, A. Ferrari and H. Hofmann, Biomaterials **26**, 2685 (2005).

[3] M. M. Meyyappan, M., J. Phys. D., Appl. Phys. **44**, (2011).

[4] Z. H. Han, Z. J., I. Levchenko, S. Kumar, M. M. A. Yajadda, S. Yick, D. H. Seo, P. J. Martin, S. Peel, Z. Kuncic and K. Ostrikov, J. Phys. D, Appl. Phys. **44**, (2011).

[5] F. Rossi and P. Colpo, J. Phys. D., Appl. Phys. **44**, 9 (2011).

[6] D. F. Moyano and V. M. Rotello, Langmuir **10** (2011).

[7] G. Han, P. Ghosh, M. De and V. M. Rotello, Nanobiotechnol. **3**, 40 (2007).

[8] H. B. Na, I. C. Song and T. Hyeon, Adv. Mater **21**, 2133 (2009).

[9] N. M. Mackie, D. G. Castner and E. R. Fisher, Langmuir **14**, 1227 (1998).

[10] G. S. Malkov, I. T. Martin, W. B. Schwisow, J. P. Chandler, B. T. Wickes, L. J. Gamble, D. G. Castner and E. R. Fisher, Plasma Process. Polym. **5**, 129 (2008).

[11] A. Harsch, J. Calderon, R. B. Timmons and G. W. Gross, Journal of Neuroscience Methods **98**, 135 (2000).

[12] V. Ley, A. P. Kruzic and R. B. Timmons, Journal of Membrane Science **226**, 213 (2003).

[13] S. Schiller, J. Hu, A. T. A. Jenkins, R. B. Timmons, F. S. Sanchez-Estrada, W. Knoll and R. Forch, Chemistry of Materials **14**, 235 (2002).

[14] Y. L. J. Wu, R. B. Timmons, J. S. Jen and F. E. Molock, Colloids and Surfaces B-Biointerfaces **18**, 235 (2000).

[15] M. L. Steen, L. Hymas, E. D. Havey, N. E. Capps, D. G. Castner and E. R. Fisher, J. Membrane Sci. **188**, 97 (2001).

[16] M. L. Steen, A. C. Jordan and E. R. Fisher, J. Membrane Sci. **204**, 341 (2002).

[17] G. S. Malkov and E. R. Fisher, Plasma Process. Polym. **7**, 12 (2010).

[18] S. Debnath, R. Ranade, S. L. Wunder, G. R. Baran, J. Zhang and E. R. Fisher, J. Appl. Polym. Sci. **96**, 1564 (2005).

[19] M. L. Steen, W. C. Flory, N. E. Capps and E. R. Fisher, Chem. Mater. **13**, 2749 (2001).

[20] J. Zhou and E. R. Fisher, J. Nanosci. Nanotechnol. **4**, 539 (2004).

[21] J. C. Shearer, M. J. Fisher, D. Hoogeland and E. R. Fisher, Appl. Surf. Sci. **256**, 2081 (2010).

[22] I. T. Martin, B. Dressen, M. Boggs, Y. Liu, C. S. Henry and E. R. Fisher, Plasma Process. Polym. **4**, 414 (2007).

[23] E. Sardella, P. Favia, E. Dilonardo, L. Petrone and R. d'Agostino, Plasma Process. Polym. **4**, S781 (2007).

[24] M. Lejeune, F. Bretagnol, G. Ceccone, P. Colpo and F. Rossi, Surf. Coatings Technol. **200**, 5902 (2006).

[25] A. Fahmy, R. Mix, A. Schönhals and J. F. Friedrich, Plasma Chem. Plasma Process. **22** (2011).

[26] P. Rossini, P. Colpo, G. Ceccone, K. D. Jandt and F. Rossi, Mater. Sci. Eng. C **23**, 353 (2003).

[27] N. T. K. Thanh and L. A. W. Green, Nano Today **5**, 213 (2010).

[28] S. Swaraj, U. Oran, A. Lippitz, J. F. Friedrich and W. E. S. Unger, Surf. Coatings Technol. **200**, 494 (2005).
[29] L. OToole and R. D. Short, Journal of the Chemical Society-Faraday Transactions **93**, 1141 (1997).
[30] W. Asghar, A. Ilyas, R. R. Deshmukh, S. Sumitsawan, R. B. Timmons and S. M. Iqbal, Nanotechnology **22**, (2011).
[31] N. M. Mackie, N. F. Dalleska, D. G. Castner and E. R. Fisher, Chem. Mater. **9**, 349 (1997).
[32] C. Susut and R. B. Timmons, International Journal of Pharmaceutics **288**, 253 (2005).
[33] C. I. Butoi, N. M. Mackie, L. J. Gamble, D. G. Castner, J. Barnd, A. M. Miller and E. R. Fisher, Chemistry of Materials **12**, 2014 (2000).
[34] M. A. Leich, N. M. Mackie, K. L. Williams and E. R. Fisher, Macromolecules **31**, 7618 (1998).
[35] I. T. Martin, G. S. Malkov, C. I. Butoi and E. R. Fisher, Journal of Vacuum Science & Technology A **22**, 227 (2004).
[36] L. OToole, C. A. Mayhew and R. D. Short, J. Chem. Soc. Faraday Trans. **93**, 1961 (1997).
[37] L. OToole and R. D. Short, J. Chem. Soc. Faraday Trans. **93**, 1141 (1997).
[38] K. H. A. Bogart, N. F. Dalleska, G. R. Bogart and E. R. Fisher, J. Vac. Sci. Technol. A **13**, 476 (1995).
[39] D. S. Wavhal, J. M. Zhang, M. L. Steen and E. R. Fisher, Plasma Processes Polym. **3**, 276 (2006).
[40] K. J. Trevino and E. R. Fisher, Plasma Processes Polym. **6**, 180 (2009).
[41] N. B. Colthup, L. H. Daly and S. E. Wiberley, *Introduction to Infrared and Raman Spectroscopy*, Academic Press, San Diego (1990).

# CHAPTER 5

# DESIGN AND OPERATION OF A ROTATING DRUM RADIO FREQUENCY PLASMA REACTOR FOR THE MODIFICATION OF FREE NANOPARTICLES

This chapter encompasses work published in *Review of Scientific Instruments* and describes the design and function of a rotating drum rf plasma reactor. This proof-of-concept reactor utilizes plasma polymerized allyl alcohol (*pp*-allylOH) to add OH functionality to $Fe_2O_3$ nanoparticles. The reactor is designed to be adapted to current plasma hardware, eliminating the need for an independent reactor setup. Deposition was performed on Si wafers, $Fe_2O_3$ nanoparticles supported on Si wafers, and freely rotating $Fe_2O_3$ nanoparticles to demonstrate the utility of the reactor. Many surface characterization methods were used to verify that no extensive change in the size or shape of the nanoparticles occurred because of the rotating motion of the reactor. The reactor design was also extended to a non-depositing plasma modification system to show the design is effective under multiple plasma processing conditions.

## 5.1 Introduction

The use of nanoparticles (nps) in biological applications, such as targeted drug delivery,[1] has become an extremely active area of research. The ability to use many nps in a range of applications is, however, limited as their surface chemistry can generate issues with agglomeration, biological incompatibility,[2] and metal toxicity.[3] One solution for many of these problems is to functionalize the surface of nanomaterials using thin polymeric films that can be tailored for specific applications.[4] Several methods have been employed to create these thin coatings, including chemical vapor deposition (CVD),[5] spray pyrolysis,[6] and plasma-enhanced CVD (PECVD).[7]

Plasma processing is a model method for modifying and functionalizing np surfaces as it can provide uniform films on uniquely shaped particles through low temperature, solution free processing. Moreover, an assortment of processing parameters can be readily adjusted to tailor the surface composition and deposition characteristics from an immense selection of starting materials. This flexibility makes plasma processing ideal for implanting specific functional groups onto the surface of nanomaterials as well as for encapsulating nps in thin film coatings.

Several recent studies have demonstrated the power of plasma processing for nanomaterial encapsulation using cylindrical rotating plasma reactors. Hisada et al. coated FeCo nps in carbon nanotubes using a microwave PECVD technique.[7] They synthesized composite nanomaterials with high environmental resistance and catalytic properties. Susut and Timmons encapsulated acetylsalicyclic acid crystals with pulsed plasma polymerized allyl alcohol (ppallylOH) films with the goal of controlling the release rate in a model HCl system for stomach acid.[4] Their films did effectively control release rates, which they discovered were inversely proportional to plasma power, deposition time, and plasma duty cycle. Kim et al. analyzed $TiO_2$ film growth on glass beads using a rotating plasma reactor model.[8] Their calculations showed that glass beads free falling through the gas phase would have uniform coatings around the particles. Furthermore, the rotation speed of the reactor was directly proportional to film thickness, as deposition processes can occur more readily when the particles spend more time tumbling through the plasma.

Many rotating plasma reactor designs utilize independent reactor systems that cannot be adapted for other purposes. Here, we describe the design of a glass insert that can be adapted to a standard glass tubular reactor design common to our laboratory and many others within the plasma community. This insert (hereafter referred to as the rotating drum) can function within

the confines of current reactor designs, thereby mitigating the need for a specialized experimental setup. Notably, the rotating drum can be removed to allow for the plasma treatment of larger substrates or substrates that do not require movement during processing. Furthermore, our design is low cost and can be easily adapted to different configurations (e.g. by adjusting the size of the rotating drum).

As a proof-of-concept experiment, commercial $Fe_2O_3$ nps were functionalized with surface –OH via plasma polymerized allyl alcohol (*pp*-allylOH) films. The resulting composite materials were characterized with x-ray photoelectron spectroscopy (XPS), Fourier-transform infrared (FTIR) spectroscopy, and scanning electron microscopy (SEM). Films deposited on both static and rotating samples were compared using Si wafers and supported np substrates for comparison to free, unsupported nps (fnps).

The ability of the rotating drum reactor to produce customizable films was evaluated under CW and pulsed plasma conditions. As noted in Section 1.3, pulsed plasma deposition allows for better retention of the monomer structure and also limits ambient heating of the substrate, both of which reduce monomer fragmentation.[9] Furthermore, films deposited using pulsed plasma systems typically have a higher degree of functionality than films deposited under CW conditions. Having highly functionalized films on np surfaces is ideal for biological applications (i.e. cell proliferation and drug attachment). Thus, designing a reactor with the ability to conformally coat nanoparticles with tailored surface properties would undoubtedly be applicable in a variety of research areas. The ability to economically adapt existing laboratory reactors with rotating drums would provide additional opportunities for np research across a wide range of laboratories.

## 5.2 Apparatus Design

A schematic of our rotating drum plasma reactor is shown in Fig. 5.1. The outer glass tubular reactor is a standard design that has been used extensively by our labs, as described previously.[10] Briefly, it consists of two borosilicate glass tubes joined with 50 mm o-ring joints to create a 35 cm long reactor. Each outer sleeve can be easily customized with a variety of ports to allow for gas feed, pressure readouts, diagnostic monitoring, or vacuum exhaust. The total length of the reactor can also be expanded to examine downstream processes.[11] In a typical rotating drum experiment, monomer gases enter the reactor (point A) and are routed into the 70 mm x 48 mm glass inner chamber through a capillary using an o-ring seal (point B). Gases flow into the coil region (point C), where the plasma is ignited, thereby generating the plasma species that ultimately interact with the substrates. A series of three holes (point D) allow gas to exit the rotating drum region to be pumped away with the total system pressure measured (point E) adjacent to the exhaust (point F). The inner chamber is connected to a glass rod via an o-ring joint; the rod is connected to a rotating motor (point G) and is used as the primary axis of rotation. A five-turn, copper plated nickel induction coil (average distance between turns ~1.0 cm) was used to generate the plasma within the rotating drum region. Optimization experiments with alternate reactor designs showed that longer, less compact induction coils did not yield plasma glow within the drum region. Sample introduction and removal occurs by disconnecting the joint between the rotating drum and glass rod. Rotating Si wafers and supported np substrates were taped to the inner wall of the rotating drum during deposition.

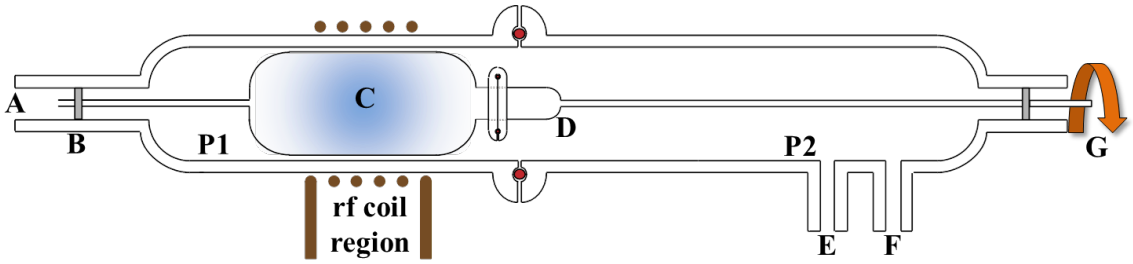


**Figure 5.1.** Schematic of the rotating drum reactor apparatus.

## 5.3 Experimental Details

**5.3.1 Sample Preparation** Si wafers were cleaned with methanol prior to plasma treatment to remove possible contaminants (i.e. dust or debris). Supported nanoparticle substrates were prepared by the suspension method described in Section 2.1.2. No additional cleaning or surface modification was performed on these substrates. Free $Fe_2O_3$ nanoparticles (fnps) were also used as substrates and were used as received with no additional cleaning.

**5.3.2 Deposition Parameters** CW *pp*-allylOH depositions were performed in a 50 W plasma for 30 min with a total system pressure of 100 mTorr. Between depositions, the reactor was cleaned with an $O_2$ plasma (100 mTorr, 150 W, 30 min) to remove residual deposited films from the reactor walls. All pulsed plasma depositions were performed at a 5% d.c. with a pulse duration of 10 ms and an on-time applied rf power of 50 W. For surface modification studies, fnps were treated in a 50 W, 100 mTorr $NH_3$ (Air Gas, 99.99%) CW plasma for 20 min while the reactor was rotating at 15 rpm.

## 5.4 Evaluation of Reactor Performance

The reactor's design was evaluated under non-rotating, or static, (placing substrates both inside and outside of the drum region) and rotating conditions. Three types of substrates were employed in this study: Si wafers, supported $Fe_2O_3$ nps, and free, unsupported $Fe_2O_3$ nps. Depositions on Si wafers and supported $Fe_2O_3$ nps were used to aid in characterization of the deposited films via XPS and SEM, and to serve as controls for films deposited on fnps. The viability of the rotating reactor design was based on its ability to conformally coat the fnps and precisely tailor the composition of the deposited films. The experiments described here were designed to

maximize –OH functional groups on the nps with *pp*-allylOH films to provide a medium for further functionalization (i.e. cell, protein, or drug attachment).

### 5.4.1 Static Substrates

Table 5.1 lists the XPS atomic compositions of *pp*-allylOH films deposited on various substrates under CW and pulsed plasma conditions. When the drum is static, CW plasma conditions yield deposited films with 78.6 ± 0.7 % C and 21.4 ± 0.7 % O for film deposited on bare Si wafers within the drum region. Films deposited under the same conditions on supported np substrates have similar atomic compositions with 80.5 ± 0.4 % C and 19.5 ± 0.4 % O. Furthermore, deconvolution of high resolution XPS spectra (Fig. 5.2a-b) reveals similar $C_{1s}$ binding environments for films deposited on bare Si wafers and on supported np substrates. This is consistent with previously published results from our lab[14] that indicate there is little difference in atomic compositions for films deposited on Si wafers and those deposited on supported np substrates in our standard, inductively-coupled glass tubular plasma reactors. Specifically, $SiO_xC_y$ films deposited on $TiO_2$ supported np substrates and *pp*-allylOH films deposited on $Fe_2O_3$ supported np substrates were shown to have similar atomic compositions to films deposited on bare Si wafers under the same plasma conditions.[15]

Table 5.1 also lists atomic compositions for films deposited on bare Si wafers and supported np substrates under pulsed plasma conditions (d.c. = 5%). Under these conditions, oxygen incorporation in the films (%O ≈ 33%) is significantly higher than in films deposited under CW conditions (%O ≈ 21%). Additionally, as with films deposited under CW conditions, there is little difference in the atomic compositions of films deposited under pulsed plasma conditions on Si wafers and those deposited on supported np substrates when the drum is static.

**Table 5.1.** XPS atomic compositions for *pp*-allylOH films deposited on various substrates

| Substrate Type | Static or Rotating | Location | d.c. | Fe (%) | Si (%) | C (%) | O (%) | O/C |
|---|---|---|---|---|---|---|---|---|
| Untreated Si wafer | | | | | 24.8 ± 1.4 | 21.1± 2.1 | 54.1 ± 1.4 | 2.58 ± 0.3 |
| Si wafer | static | drum | CW | | | 78.6 ± 0.7 | 21.4 ± 0.7 | 0.27 ±0.01 |
| | static | drum | 5% | | | 66.6 ± 0.9 | 33.4 ± 0.9 | 0.50 ± 0.02 |
| | static | P1 | CW | | | 75.4 ± 0.9 | 24.5 ±0.9 | 0.33 ± 0.02 |
| | static | P2 | CW | | | 79.1 ± 0.9 | 21.1 ± 0.6 | 0.27 ± 0.01 |
| | rotating | drum | CW | | | 80.5 ± 0.4 | 19.5 ±0.4 | 0.24 ± 0.005 |
| | rotating | drum | 5% | | | 67.7 ± 0.8 | 33.3 ± 0.8 | 0.50 ± 0.02 |
| Supported $Fe_2O_3$ np | static | drum | CW | | | 80.8 ± 0.1 | 19.2 ± 0.1 | 0.23 ± 0.002 |
| | static | drum | 5% | | | 66.4 ± 0.6 | 33.6 ± 0.6 | 0.50 ± 0.01 |
| | rotating | drum | CW | | | 79.0 ± 0.6 | 21.0 ± 0.6 | 0.27 ± 0.01 |
| | rotating | drum | 5% | | | 63.3 ± 0.8 | 33.0 ± 1.0 | 0.52 ± 0.02 |
| Untreated $Fe_2O_3$ fnps | | | | 37.4 ± 3.6 | | 10.7 ± 2.5 | 51.6 ± 4.8 | 5.1 ± 1.5 |
| $Fe_2O_3$ fnps | static | drum | CW | 32.4 ± 2.2 | | 27.5 ± 1.9 | 40.1 ± 0.3 | 1.4 ± 0.2 |
| | static | drum | 5% | 35.3 ± 0.5 | | 20.5 ± 0.7 | 44.3 ± 1.1 | 2.17 ± 0.1 |
| | rotating – 30 min | drum | CW | 12.2 ± 2.3 | | 59.2 ± 3.6 | 28.6 ± 1.5 | 0.49 ± 0.6 |
| | rotating – 60 min | drum | CW | 12.6 ± 2.0 | | 62.7 ± 2.1 | 24.7 ± 0.8 | 0.39 ± 0.02 |
| | rotating – 60 min | drum | 5% | 28.3 ± 0.5 | | 30.1 ± 2.2 | 41.6 ± 1.8 | 1.39 ± 0.2 |

The fnps were also processed in our rotating drum under static conditions. Elemental analysis data, Table 5.1, reveal the surface composition of the fnps contains ~27% C, 40% O, and 32% Fe when treated under CW plasma deposition conditions. For fnps treated under pulsed plasma conditions, the surface composition is ~21% C, 44% O, and 35% Fe. The high iron content (from the native particles) is indicative of a nonuniform treatment of the nanoparticles while the reactor is static.

Although the reactor was designed to direct all monomer gases into the rotating drum region, we explicitly evaluated how deposition processes differ inside and outside of the rotating drum region. Bare Si wafer substrates were placed ~4 cm upstream and ~14 cm downstream of the rf coil in the main reactor chamber (labeled as P1 and P2 in Fig. 5.1). Films deposited under CW plasma conditions on the upstream substrates have an O/C ratio of ~0.33; films deposited on downstream substrates have a slightly lower O/C of ~0.27. The upstream sample clearly has a thin film, thereby confirming that some portion of the monomer gas travels outside of the rotating drum upstream from the plasma coil. Moreover, films deposited on the downstream substrate have atomic compositions similar to those of films deposited under CW conditions within the drum region. With CW plasma treatments, the rotating drum region of the reactor produces films with compositions similar to those achieved with downstream processing.

Deposited films were also analyzed using FTIR spectroscopy to better understand what functional groups are formed in the *pp*-allylOH films produced in our rotating reactor, Fig. 5.4a-b. All films produced under static conditions exhibit characteristic peaks for *pp*-allylOH, including C-O and C=O stretching (~1050 $cm^{-1}$ and 1650 $cm^{-1}$, respectively), as well as C-$H_x$ vibrations (~2900 $cm^{-1}$). Absorbance bands corresponding to C-$H_x$ wagging and O-H deformation are observed at ~1450 and ~1370 $cm^{-1}$, respectively. The most noticeable difference between the

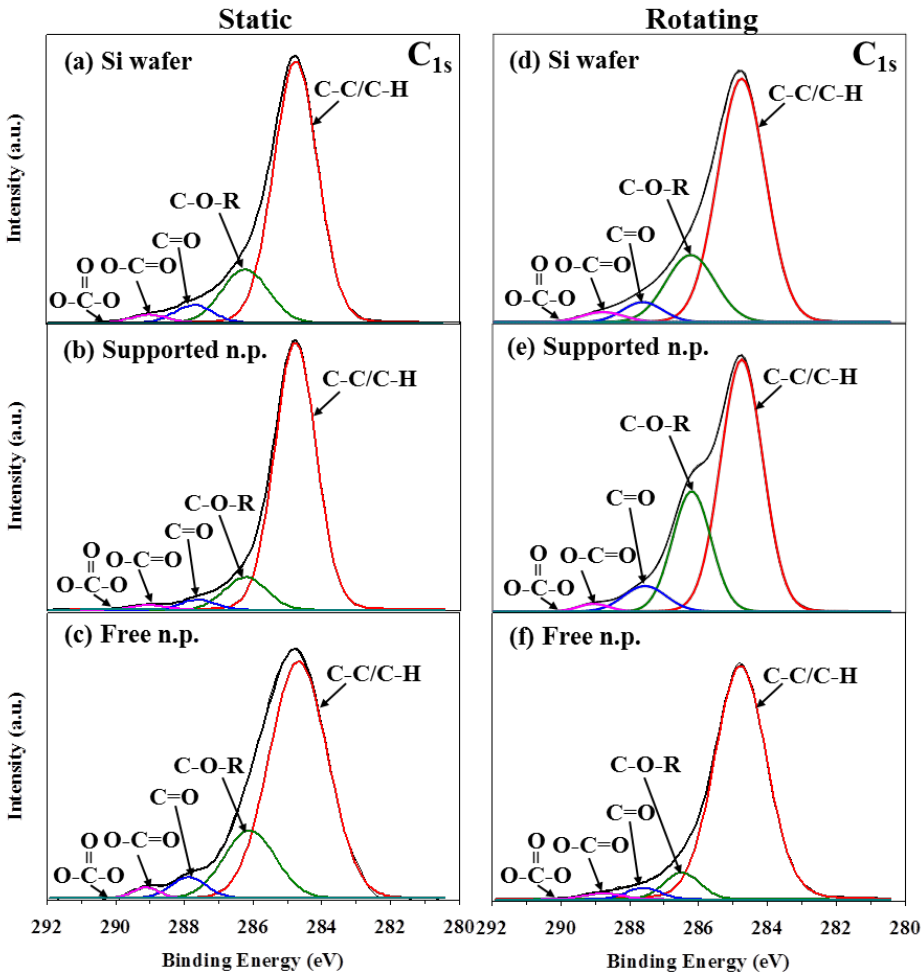


**Figure 5.2.** High resolution $C_{1s}$ spectra of *pp*-allylOH deposited in a CW plasma on Si wafers, supported np substrates, and fnps while the reactor was static **(a-c)** and rotating **(d-f)**.

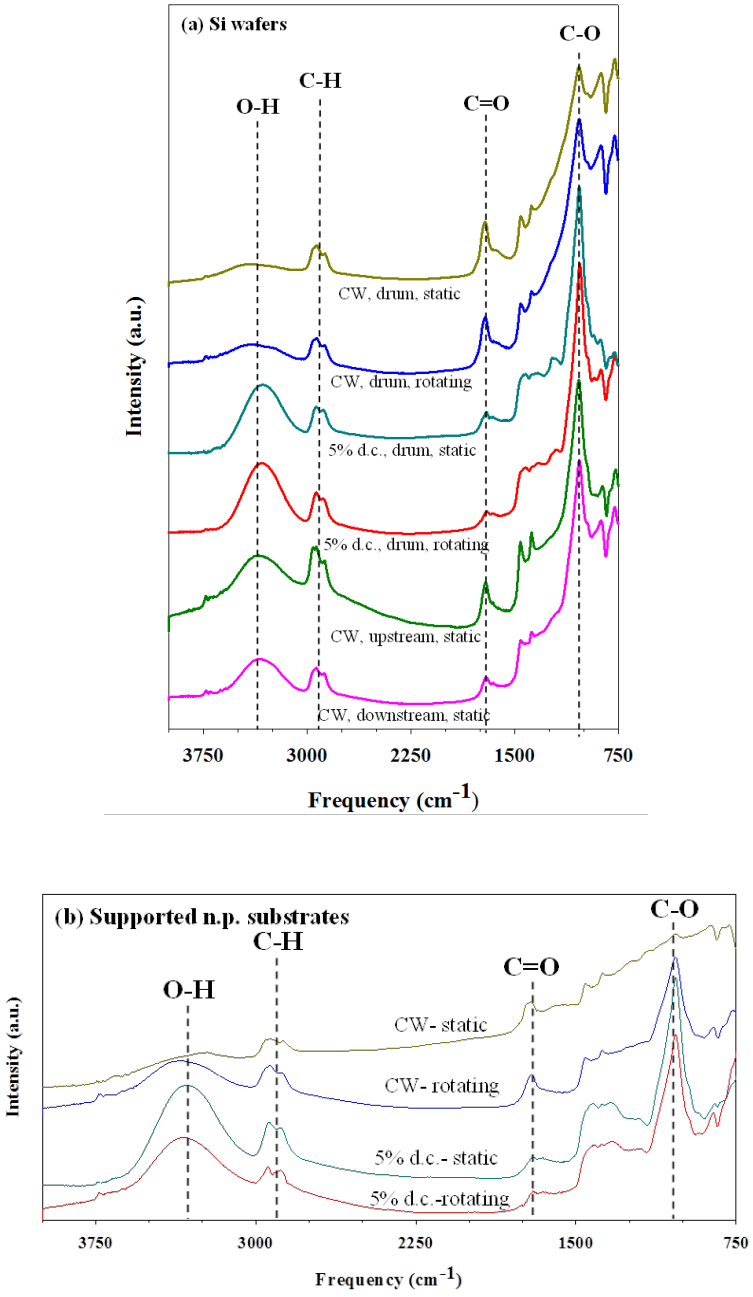


**Figure 5.3.** FTIR spectra for *pp*-allylOH deposited in CW and pulsed plasmas on **(a)** Si wafers and **(b)** supported np substrates. The dotted lines indicate the O-H, C-H, C=O, and C-O stretching vibrations

spectra is the change of the O-H stretching band centered at ~3400 $cm^{-1}$. For films deposited under pulsed conditions, this feature is significantly more intense relative to the C-H stretch, suggesting a higher incorporation of alcohol groups within the film and consequently higher retention of OH functionality from the allylOH monomer. The C-O and O-H absorption peaks are also proportionally larger for films deposited in pulsed mode. As C-O-H functionality requires both C-O and O-H bonds, this proportional increase further reinforces the observation that the pulsed mode incorporates greater alcohol functionality in the films. Similar FTIR spectra were obtained for films deposited in the drum region of the reactor on supported np substrates under CW and pulsed plasma conditions. As with films deposited on Si wafers, the O-H absorbance peak is significantly larger for films deposited under pulsed plasma conditions. Furthermore, films deposited in pulsed plasmas exhibit less intense C=O absorbance relative to the intensity of the O-H stretching band. This corroborates XPS data that suggest *pp*-allylOH films deposited under static conditions, on bare Si wafers are virtually identical to films deposited on supported $Fe_2O_3$ np substrates under both CW and pulsed plasma conditions.

Deposition rates for *pp*-allylOH films were measured on bare Si wafers using VASE. Under static conditions, within the rotating drum, film deposition rates were 13.1 ± 4.2 nm/min and 6.9 ± 2.8 nm/min under CW and pulsed plasma conditions, respectively. In CW plasmas, outside of the rotating drum region films were deposited at 11.9 ± 3.2 nm/min at P1 and 42.1 ± 14.4 nm/min at P2 (Fig. 1). These values are consistent with literature results that indicate CW plasma deposition of *pp*-allylOH is faster than pulsed plasma deposition.[16]

### 5.4.2 Rotating Substrates

Replicate *pp*-allylOH depositions on bare Si wafers, supported np substrates, and fnps were conducted while the inner drum of the reactor was rotating at 15 rpm. Atomic composi-

tions for films deposited on bare Si wafers under CW plasma conditions are similar to those deposited under static conditions, with less than a ±2% difference in C and O percentages between static and rotating samples. Furthermore, this trend holds true for films deposited on supported np substrates under CW conditions, with ~ ±1% difference in C and O atomic compositions between rotating and static samples. Film deposition on bare Si wafers and supported np substrates under pulsed plasma conditions behaved in a similar manner, with static and rotating samples having films with < ±3% difference in atomic composition.

High-resolution XPS $C_{1s}$ spectra for *pp*-allylOH films deposited under CW plasma conditions on bare Si wafers and supported np substrates while the inner drum was rotating (Fig. 5.2d-e) are similar to films deposited under static conditions in that the majority of the $C_{1s}$ binding is associated with the C-C/C-H environment. Figure 5.3a-b shows high-resolution $C_{1s}$ XPS spectra for films deposited on Si wafers and supported np substrates under pulsed plasma conditions. Not only are the carbon binding environments for films deposited on Si wafers and supported np substrates similar (not shown), they mimic those present in samples treated under static conditions. Thus, the rotating action does not significantly alter the resulting film chemistry.

Figure 5.4 contains FTIR spectra for *pp*-allylOH films deposited on rotating Si wafers (Fig. 5.4a) and supported np substrates (Fig. 5.4b). The trends in OH functionality corroborate the XPS compositional data in that oxygen containing moieties are similar between Si wafers and supported np substrates and there is little difference between static and rotating samples. Furthermore, the rotating reactor affords the ability to increase
–OH functionality in the *pp*-allylOH films when operated in a pulsed plasma mode.

VASE was used to measure the deposition rates of *pp*-allylOH on Si wafers while the inner drum was rotating. The deposition rate of films deposited under CW conditions

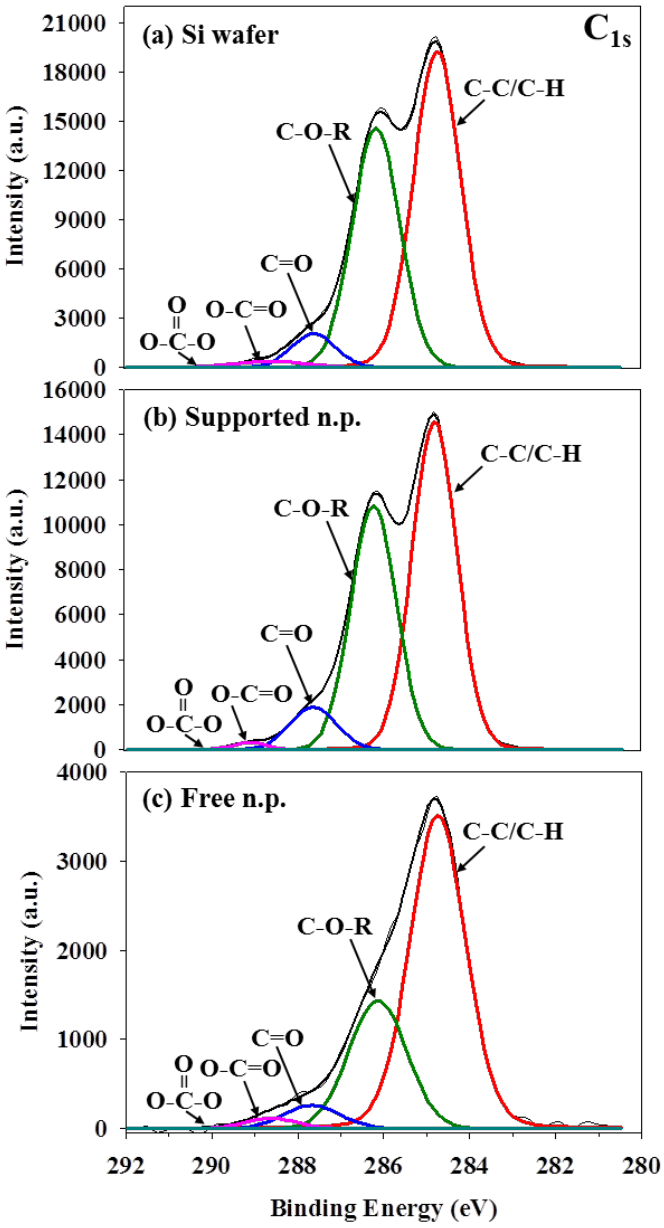


**Figure 5.4.** High resolution $C_{1s}$ spectra of *pp*-allylOH deposited in a 5% d.c. pulsed plasma on **(a)** Si wafers, **(b)** supported np substrates, and **(c)** fnps.

(13.5 ± 2.9 nm/min), was similar to that of films deposited under static conditions. Likewise, deposition rates for films deposited under pulsed plasma conditions (7.2 ± 3.1 nm/min), were identical to those found for films deposited in a static reactor under the same conditions. Thus, the deposition rate for *pp*-allylOH films deposited under CW and pulsed plasma conditions is independent of the rotating motion of the reactor.

XPS, FTIR, and VASE data show that the characteristics of *pp*-allylOH films deposited on Si wafers and supported $Fe_2O_3$ np substrates is independent of the movement of the rotating drum insert. To evaluate the efficacy of the rotating drum on a material that can freely tumble while rotating in the reactor, fnps were treated under the same conditions as the other substrates. Table 5.1 shows the atomic composition of the fnps surface after undergoing plasma treatment for 30 and 60 min while the inner drum was rotating at 15 rpm. After CW plasma deposition for 30 min, the surface of the fnps contained ~59% C, 27% O, and 12% Fe. Although Fe from the underlying substrate is detected through XPS analysis, there is a significant increase in the C content, increasing from ~10% in an untreated fnps sample to almost 60% for fnps treated for 30 min in a rotating reactor. The fnps were also treated for 60 min to increase the film thickness and deposition uniformity across particles (thereby decreasing the Fe content detected).

High resolution $C_{1s}$ XPS data for films deposited in CW plasmas on fnps while rotating for 30 min are shown in Fig. 5.2f. The carbon binding environments, specifically the major C-C/C-H environment, are similar to those in films deposited on static and rotating Si wafers and supported np substrates. Note that there is a larger contribution to the C-O-R binding environment in fnps that were plasma treated in a static reactor. This is likely the result of contributions from partially coated and uncoated $Fe_2O_3$ nps. During static plasma processing, nps are not in contact with the plasma as uniformly as when the reactor is rotating. Signal from untreated and

partially treated nps is difficult to resolve from treated nps in the XPS, as the spot size is ~3 μm in diameter. Nonuniform film deposition could, therefore, be detected for this set of samples by the increase in oxygen environments as a result of the high oxygen content in the underlying substrate. Additionally, the fnps treated under rotating conditions have films that resemble those deposited on flat substrates, Table 1, indicating that the rotating drum reactor can coat large quantities of nps more effectively than can be accomplished using static reactors.

The fnps were also treated for 60 min in a pulsed plasma system while the inner drum was rotating; the XPS atomic composition of these materials is listed in Table 5.1. The oxygen content (~42%) is significantly greater than that of untreated fnps and fnps treated in a CW plasma. Note that although films deposited in CW plasmas on static fnps are almost identical in elemental composition, the carbon and oxygen exist in significantly different binding environments. Figure 5.3c shows a high-resolution $C_{1s}$ XPS spectrum for fnps treated under pulsed plasma conditions. The high percentage of the C-O-R binding environment relative to that of fnps treated under CW, static conditions (Fig. 5.2f) demonstrates that deposition onto fnp surfaces can be specifically controlled with our rotating drum reactor. The rotating drum reactor not only produces similar films on fnps as flat, rotating substrates, but also affords the ability to conformally coat fnps while simultaneously tailoring the deposited film's composition.

As with any film deposition process, it is important to determine if the nps are physically affected by the deposition. Figure 5.5 shows SEM images of as purchased $Fe_2O_3$ fnps and fnps coated in the rotating drum (at 15 rpm, 60 min) using a CW plasma. Although it is apparent that the particles are coated in the plasma process (Fig. 5.5b), the relative size and shape of the particles does not change appreciably. The presence of Fe in the XPS data suggests that the films in the SEM image are <10 nm thick (based on the penetration depth for the XPS 45$^o$ take off angle).

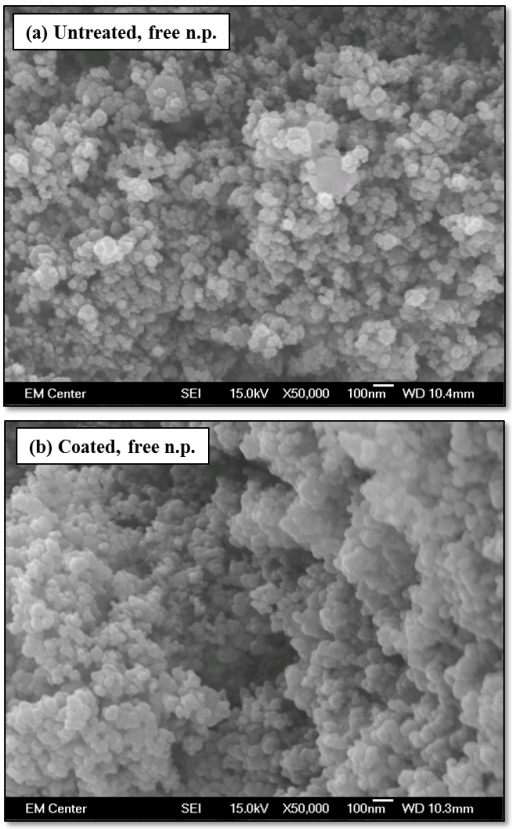


**Figure 5.5.** Scanning electron micrographs for **(a)** untreated fnps and **(b)** fnps coated in the rotating drum using a CW allylOH plasma (15 rpm, 60 min).

Additional data need to be collected to elucidate deposition rate mechanisms on freely falling particles, as the films do not deposit on the nps as fast as they do on flat substrates. It is clear from other data presented, however, that the desirable functional groups are still present on the fnps surface regardless of film thickness.

### 5.4.3 Plasma surface modification

The experiments described above demonstrate the efficacy of our rotating drum plasma reactor to deposit –OH functional groups onto nanoparticle surfaces. For certain applications, it may be necessary to modify surfaces using a non-depositing plasma modification system. To demonstrate the feasibility of using the rotating drum reactor for these types of plasma processes, $Fe_2O_3$ fnps were modified in a 100% $NH_3$ (50 W, 100 mTorr) plasma for 20 min with the reactor rotating at 15 rpm. Figure 5.6 shows XPS survey scans of as received fnps (Fig. 5.6a), $O_2$ plasma-cleaned fnps (Fig. 5.6b), and $O_2$ plasma-cleaned fnps subsequently modified in an $NH_3$ plasma (Fig. 5.6c). XPS elemental composition data reveal the as received fnps contain 10.7 ± 2.5% C, which is attributable to adventitious carbon. After exposing the fnps to a 50 W $O_2$ plasma for 10 min, the adventitious carbon content drops slightly to 8.8 ± 2.4% and the oxygen content of the surface increases from 51.6 ± 4.8% to 68.1 ± 2.2%. Plasma modification of the $O_2$ plasma cleaned fnps produced a surface containing 5.4 ± 0.5% N (N/C 0.76 ± 0.13), demonstrating our rotating drum reactor functionalizes the surface of nanoparticles (in this case with nitrogen) without depositing a film. Using this reactor design for implanting different types of functional groups using non-depositing as well as depositing systems showcases the utility of our design to plasma processing research.

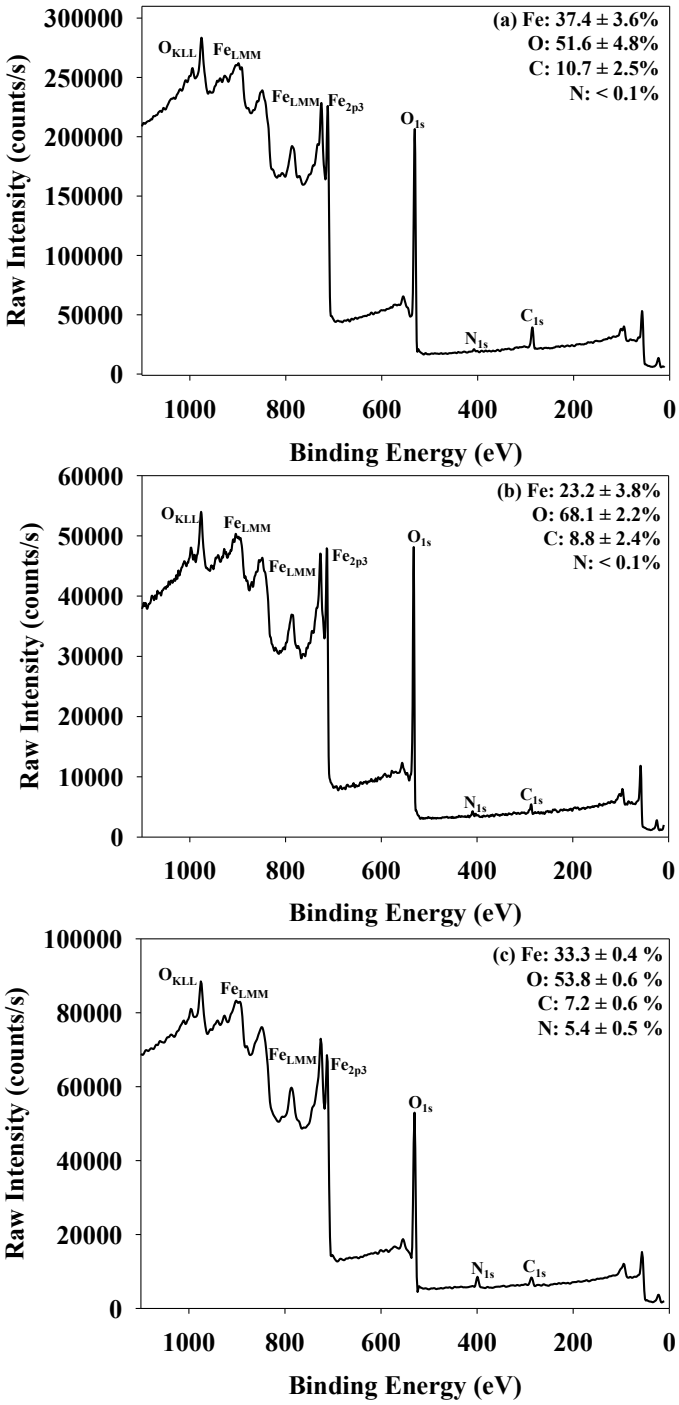


**Figure 5.6.** XPS survey spectra of **(a)** as-received $Fe_2O_3$ fnps; **(b)** $O_2$ cleaned $Fe_2O_3$ fnps; and **(c)** $O_2$ plasma-cleaned $Fe_2O_3$ fnps subsequently treated in the rotating drum with a 50 W, 100 mTorr $NH_3$ plasma (20 min, rotating at 15 rpm).

## 5.5 Further Optimization

The proof-of-concept experiments shown here were conducted to demonstrate the viability of our in-house rotating drum plasma reactor to coat or modify fnps. Our lab is continuing this work by studying the deposition parameters for other organic precursors (e.g. acrylic acid and allylamine) on a variety of nanoparticle substrates (e.g. $TiO_2$ and gold). Furthermore, a range of parameters that were left constant in this study could be explored for further optimization of specific film properties. For example, rotation speed has previously been explored by other researchers and in some cases, more uniform films are produced at faster rotations, as the fnps fall through the plasma more times. Also, our rotating drum insert often resulted in the fnps rolling down the sides of the rotating drum during plasma processing. Installing rods or spikes on the sides of the rotating drum, or using a rectangular drum, could cause the nps to fall through the plasma more effectively and functionalize the np surface more efficiently.

## 5.6 Summary

The rotating drum plasma reactor design described here affords the ability to surface modify free, unsupported nanoparticle surfaces, as demonstrated by coating $Fe_2O_3$ with *pp*-allylOH thin films (thereby imparting –OH functionality) and by surface modification via $NH_3$ plasmas (thereby imparting $–NH_x$ functionality). Although many rotating plasma reactors are designed with the sole purpose of treating rotating substrates, our unique design allows for the use of pre-built glass tubular reactors routinely used in our laboratories and others. This not only provides an inexpensive apparatus design, but also allows for the modification of existing tubular reactors should rotating capabilities be needed. The data presented show that deposited films on bare Si wafers and supported np substrates are independent of the rotating movement of the reac-

tor. Furthermore, pulsing the plasma increases the –OH functionality within the films, similar to what is observed in non-rotating glass reactors. Films deposited on fnps while the reactor is rotating resemble those deposited on flat substrates, affording us the ability to apply a variety of deposition processes to fnps. The reactor also successfully modified fnps in a non-depositing plasma modification system, demonstrating the ability to operate under various plasma conditions. Finally, because this rotating drum apparatus can act as an insert to traditional reactor systems that are already in place, this design is more economical than constructing an independent apparatus and can easily be deployed in existing laboratory environments.

REFERENCES


[1] De, M.; Ghosh, P. S.; Rotello, Adv Mater. **22**, 4225 (2008).
[2] Singh, R. K.; Kim, T. H.; Patel, K. D.; Knowles, J. C.; Kim, H. W., B. J Biomed Mater Res A. **7**, 1734 (2012).
[3] Abdullaeua, Z.; Omurzak, E.; Iwamoto, C.; Ganapathy, H. S.; Sulaimankulova, S.; Chen, L. L.; Mashimo, T., Carbon. **5**, 1776 (2012).
[4] Susut, C.; Timmons, R. B., Int J Pharm. **2**, 253 (2005).
[5] Chopra, N.; Bachas, L. G.; Knecht, M. R., Chem Mater. **7**, 1176 (2009).
[6] Jian, N. W.; Li, Z.; Fan, Y.; Zhao, M. S., J Phys Chem B. **8**, 2119 (2007).
[7] Hisada, D.; Fujiwara, Y.; Sato, H.; Jimbo, M.; Kobayashi, T.; Hata, K., J Magn Magn Mater. **24**, 3184 (2011).
[8] Kim, D. J.; Kang, J. Y.; Kim, K. S., J Ind Eng. **6**, 997 Chem (2010).
[9] Plasma Polymer Films. Imperial College Press: London, 2004; p 391.
[10] Bogart, K. H. A.; Dalleska, N. F.; Bogart, G. R.; Fisher, E. R., J Vac Sci Technol A. **2**, 476 (1995).
[11] Butoi, C. I.; Mackie, N. M.; Gamble, L. J.; Castner, D. G.; Barnd, J.; Miller, A. M. Chem Mater. **7**, 2014 (2000).
[12] OToole, L.; Short, R. D., J Chem Soc Faraday Trans. **6**, 1141 (1997).
[13] Vickerman, J. C., *Surface Analysis - The Principle Techniques*. John Wiley & Sons: Chichester, 1997; p 51.
[14] Shearer, J. C.; Fisher, E. R., Nanosci Nanotech Let. **3**, 358 (2012).
[15] Shearer, J. C.; Fisher, M. J.; Hoogeland, D.; Fisher, E. R., Appl Surf Sci. **7**, 2081 (2010).
[16] Watkins, L.; Bismarck, A.; Lee, A.; Wilson, D.; Wilaon, K., Appl Surf Sci. **23**, 8203 (2006)

CHAPTER 6

# PLASMA COPOLYMERIZATION OF ALLYL ALCOHOL AND ALLYL AMINE: THE EFFECTS OF AGING ON CONTACT ANGLE AND SURFACE COMPOSITION

This chapter describes the plasma copolymerization of allyl amine (allylNH) and allyl alcohol (allylOH). The effects of various gas feed mixtures on resulting film properties were analyzed using both CW and pulsed plasma deposition conditions. Deposited films were analyzed with x-ray photoelectron spectroscopy and contact angle goniometry; data were evaluated as a function of film age. Films deposited under CW plasma conditions were more hydrophobic than the underlying substrate and were primarily composed of hydrocarbon, ether and amine functionalities. Pulsed plasma-deposited films contained significant alcohol and amine functionality and were very hydrophilic. As the films aged, all CW plasma-deposited films experienced hydrophobic recovery, whereas some films deposited under pulsed plasma conditions showed increased wettability during the aging period. At the time of this writing, this work is being prepared for submission to *Surface Coatings and Technology*.

## 6.1 Introduction

Plasma polymerization is widely used to implant functional groups onto a variety of materials for applications in cell growth, tissue regeneration, protein fouling, and controlled drug release.[1-6] Incorporating functional groups such as carboxylic acids, alcohols, and amines can increase wettability of and cell adhesion to surfaces designed for use in biomedical devices.[2,7-10] However, there is ongoing debate as to which surface properties and chemistries better enhance cell attachment and growth.[2,11-15] Khorasani and coworkers plasma modified poly ($_L$-lactic acid)

(PLA) surfaces, increasing the wettability as well as incorporating a variety of oxygen-containing functional groups onto the polymer surface.[16] They showed that these newly functionalized surfaces enhanced the growth and attachment of B65 cells over that on untreated PLA. These enhancements were attributed to the reactions between the cells and the implanted O-containing functional groups, as well as the increased wettability caused by the polar surface functional groups.

Garrido et al. plasma treated 3-hydroxybutyrate-3-hydroxyvalerate (PHBV) with oxygen and nitrogen plasmas and found the hydrophilicity of the surfaces increased after treatment,[15] likely as a result of incorporated C-O and C-N functionality. Human keratinocytes seeded onto the PHBV grew more actively on oxygen plasma-treated surfaces than nitrogen plasma-treated surfaces, and all plasma treated surfaces showed enhanced cell growth over untreated PHBV. In contrast, Pompe et al. demonstrated that endothelial cells showed enhanced growth on nitrogen-containing surfaces produced by $NH_3$ plasma treatments relative to that on $H_2O$ plasma treated surfaces. Recently, Jacobs et al. published a comprehensive review listing over 60 methods of enhancing cell growth by imparting oxygen and nitrogen functionality to control wettability and chemical functionality on surfaces.[2] This review noted that the vast array of parameters that exist in cell-surface interaction studies make it difficult to gain a detailed understanding of the processes. It is, however, generally accepted that highly hydrophilic surfaces containing oxygen and nitrogen functionalities are key to promoting cell attachment and growth mechanisms. Because it can be difficult to find one material that meets all the requirements for a specific application, the simultaneous implantation of two or more of these functionalities in a single process could efficiently facilitate creation of tailored surfaces for biomedical applications.

Plasma copolymerization can create thin, conformal, pinhole-free films with varying functionalities and is an effective method for producing surfaces with a wide range of functional groups. For example, allylamine (allylNH) has been copolymerized with acrylic acid,[17,18] ethylene glycol,[19,20] and 1,2-octadiene[21,22] to deposit hydrocarbon films with alcohol, carboxylic acid, and amine functionality, respectively. Acrylic acid and hexamethyldisilazane (HMDS) have been plasma copolymerized to implant carboxylic acid functionality into the Si-C/Si-N network of the HMDS precursor.[1,3,23] Gallino and Short used an allyl alcohol (allylOH) and 1,7-octadiene copolymerization process to add alcohol functionality to surfaces to promote human keratinoctye attachment.[19,24] As all of these studies suggest, producing surfaces with a variety of functional groups is a critical component to further development of many advanced biomedical applications.

Whereas Chapter 7 will discuss the effects of plasma treatment on cell growth, this chapter focuses on efforts to controllably produce thin film materials containing a range of functional groups by using plasma copolymerization of allylOH and allylNH. Precursor selection was predicated on previous results that indicated a variety of functional groups could be incorporated into deposited films and that film functionality could be controlled by deliberately choosing specific reaction conditions. Specifically, pulsed allylOH plasmas deposit films containing ester and alcohol functional groups, as described in Chapter 4 and elsewhere.[1,3,21,25] Likewise, allylNH plasmas can deposit films rich in amine functionality.[19,26] To our knowledge, this is the first report of plasma copolymerization of these two monomers; thus one goal of this work was to produce copolymerized films using CW and pulsed plasmas to gain insight into the relationship between film composition and wettability for materials containing multiple functional group types (i.e. –OH, –COOR, –C-O-C, and $–NH_x$). Because long term stability is

important for practical use of these materials,[7,27] film composition and wetting properties were analyzed as a function of film age.

## 6.2 Results and Discussion

### 6.2.1 CW plasma deposited films

Table 6.1 lists the XPS elemental composition of films deposited under CW plasma conditions (50 W, $P_T$ = 100 mTorr, 9 cm downstream, 8 min). Films were deposited with uniform thickness (~50 nm), and those analyzed immediately (< 2 h) after plasma treatment are described as "fresh" and films that were aged under ambient laboratory conditions are described by the time after deposition when the analysis was performed. Films are also referenced by the relative amount of allylNH present in the plasma gas feed, with the remaining percentage attributable to allylOH.

As expected, the oxygen content within the films decreases and nitrogen content increases with increasing allylNH in the plasma gas feed, Table 6.1. Figure 6.1 provides a graphical depiction of these data, showing O/C and N/C ratios as a function of allylNH in the gas feed. Freshly deposited films from ≤40% allylNH plasmas have similar O/C ratios of ~0.14, Fig. 6.1a. Films freshly deposited from ≥60% allylNH plasmas all have similar O/C. After deposition, oxidation of the films occurs immediately, as evidenced by the O/C ratio increasing as much as 99% in the first 24 h, but does not undergo as substantial additional oxidation over the remainder of the 1 month aging period.

The N/C ratio for all freshly deposited films produced with allylNH in the gas feed increases linearly as a function of increasing allylNH, Fig. 6.1b. This positive linear correlation persists as the scaffolds age, with high coefficients of determination ($R^2 \geq 0.96$) for all data sets.

**Table 6.1. XPS Elemental Composition of films deposited in allylNH/allylOH plasmas[a]**

| Sample Age | AllylNH in Feed (%)[b] | C (%) | O (%) | N (%) |
|---|---|---|---|---|
| Fresh | 100 | 74.3 ± 0.4 | 4.7 ± 0.5 | 21.1± 0.4 |
| | 80 | 76.2 ± 0.9 | 5.2 ± 0.4 | 18.7 ± 1.0 |
| | 60 | 77.3 ± 0.6 | 5.4 ± 0.6 | 17.3 ± 1.2 |
| | 40 | 77.6 ± 1.9 | 9.9 ± 0.2 | 12.4 ± 1.9 |
| | 20 | 83.6 ± 1.5 | 6.1 ± 1.3 | 10.3 ± 0.3 |
| | 0 | 87.3 ± 0.4 | 12.7 ± 0.4 | 0.0 ± 0.0 |
| 24 h | 100 | 73.2 ± 0.7 | 9.2 ± 1.1 | 17.7 ± 0.7 |
| | 80 | 73.1 ± 1.3 | 10.3 ± 0.5 | 16.7 ± 1.2 |
| | 60 | 75.0 ± 0.3 | 11.2 ± 0.6 | 13.8 ± 0.4 |
| | 40 | 74.9 ± 1.5 | 16.2 ± 0.4 | 8.9 ± 1.2 |
| | 20 | 79.1 ± 0.5 | 15.9 ± 0.6 | 5.0 ± 0.2 |
| | 0 | 83.2 ± 0.7 | 16.5 ± 0.4 | 0.0 ± 0.0 |
| 1 month | 100 | 71.1 ± 1.6 | 12.8 ± 0.6 | 16.0± 1.6 |
| | 80 | 74.1 ± 2.0 | 11.2 ± 1.3 | 14.7 ± 0.8 |
| | 60 | 75.3 ± 0.3 | 12.9 ± 0.3 | 11.7 ± 0.3 |
| | 40 | 74.3 ± 0.6 | 17.8 ± 0.1 | 7.9 ± 0.5 |
| | 20 | 80.5 ± 0.3 | 14.7 ± 0.2 | 4.8 ± 0.4 |
| | 0 | 84.7 ± 0.2 | 15.1 ± 0.2 | 0.0 ± 0.0 |

[a]All films were produced in CW plasmas with $P$ = 50 W, total pressure of 100 mTorr, treatment time of 8 min, and substrate location = 9 cm downstream from the coil.
[b]Remainder of feed gas composition was allylOH.

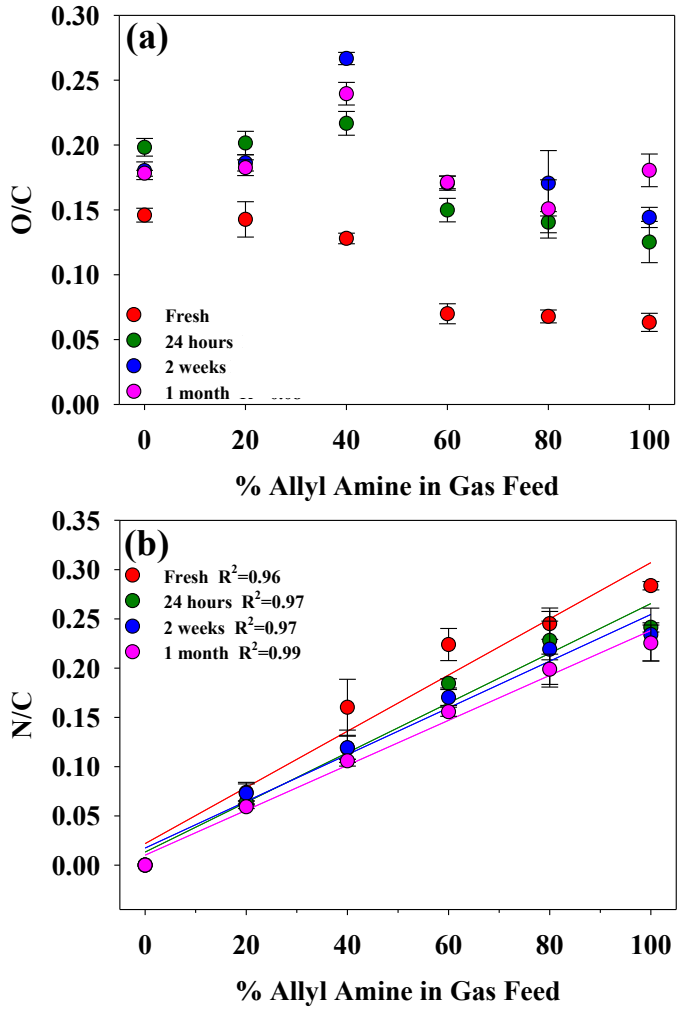


**Figure 6.1.** O/C and N/C ratios for the films deposited in CW allylOH/allylNH plasmas as a function of gas feed composition. Data were fit with a linear least squares regression analysis; $R^2$ values for the fits are reported in the figure legend where appropriate.

Although the N/C ratio is relatively stable over the 1 month aging period, films deposited in ≥40% allylNH plasmas do exhibit a small decrease 24 h after plasma treatment, which has been suggested by Gerenser[28] to occur through loss of $NH_3$ upon exposure to air.

High-resolution $C_{1s}$ XPS spectra for films deposited in CW systems are shown in Figure 6.2. The spectrum of the freshly deposited 100% allylOH plasma-deposited film, Fig. 6.2a, was deconstructed into three primary binding environments, C-C/C-H (285.0 eV), C-OH/C-OR (286.5 eV), and C=O/O-C-O (288.0 eV), all of which are characteristic of plasma polymerized allylOH (*pp*-allylOH).[1,3,21,29] The $C_{1s}$ spectrum for a freshly deposited film using a 100% allylNH plasma is shown in Fig. 6.2c and was deconstructed based on literature assignments by Kearns[7] and Shard.[17] Peak fitting XPS spectra of plasma polymerized allylNH (*pp*-allylNH) films is complex because of the many oxygen and nitrogen binding environments that can form in the film as well as the overlap in binding energies that can occur between these moieties. For this reason, we chose to group several binding environments together to streamline data analysis. Specifically, the $C_{1s}$ spectrum for *pp*-allylNH deposited in a 100% allylNH CW plasma has been fit using peaks assignable to C-C/C-H (285.0 eV), C-N/C-O (286.0 eV), C-OH/C-OR/C-N (286.5 eV), and N-C=O/C=O (288.0 eV) moieties. Based on XPS elemental analysis, oxygen incorporation occurs essentially immediately upon exposure to atmosphere as described by the mechanisms in Section 1.2.1. The associated C-O binding environments, which correspond to the uptake of oxygen during aging, overlap with the C=N binding environment at 286.5 eV and 288.0 eV in the films. Gallino and coworkers have shown, however, that amide binding is very weak in *pp*-allylNH films; thus, we assign the peak at 288.0 eV to primarily C=O from oxidation upon exposure to air.[19] The distinct appearance of the peak at 286.0 eV (peak *v*) can, therefore, be associated with C-N binding from the allylNH precursor.

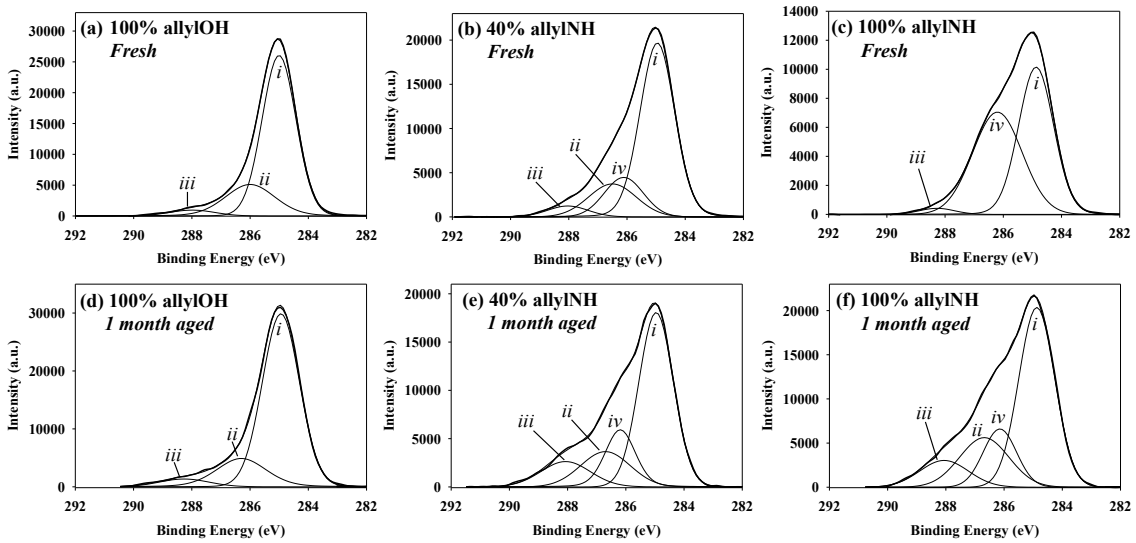


**Figure 6.2.** High resolution $C_{1s}$ XPS spectra for the films deposited in CW plasmas containing 100% allylOH, 40% allylNH, and 100% allylNH. Data for (a-c) freshly deposited and (d-f) aged films are shown. The labeled binding environments correspond to (*i*) C-C/C-H, (*ii*) C-OH/C-OR, (*iii*) N-C=O/C=O, and (*iv*) N-C/C=O.

The high-resolution $C_{1s}$ spectrum from a film freshly deposited in a 40% allylNH plasma, Fig. 6.2b, is representative of films deposited under CW conditions in mixed-gas systems. All of the binding environments in films deposited in single-gas systems appear in the films deposited in mixed-gas systems. As such, the copolymerized films contain a mixture of -C-C, -C-OR, -C-OH, -C-N, -C=O binding. Unfortunately, because of the significant overlap of the nitrogen-carbon and oxygen-carbon signal in the XPS spectra, it is difficult to extract and differentiate contributions from C-O and C-N binding in the environments at 286.0 and 286.5 eV. Thus, we have again analyzed these as a single environment at ~286.3 eV. Figure 6.2d-f shows high-resolution $C_{1s}$ XPS spectra for films aged 1 month. Notable changes occur with an increase in (and appearance of, in the case of the 100% allylNH deposited film) environments containing contributions from C-O moieties. This supports the elemental composition data that suggest oxidation of the films occurs upon aging.

FTIR was utilized to further explore the functional groups present within the films. Figure 6.3 shows FTIR spectra for films deposited with 0, 40, and 100% allylNH in the gas feed. Prominent absorption peaks include NH and OH stretching at ~ 3300 $cm^{-1}$,[20] aliphatic $CH_x$ stretching at ~2800 $cm^{-1}$, CH stretching at ~2700 $cm^{-1}$,[30] and CN stretching at ~2280 $cm^{-1}$. The large absorbance band between 1500 and 1700 $cm^{-1}$ arises from the stretching modes of C=C, imines, amines, or amide groups.[19] Peaks at ~1460 and 1390 $cm^{-1}$ are associated with $CH_2$ and CH bending, respectively, and the large absorbance band between 1000 and 1250 $cm^{-1}$ corresponds to C-O and C-N stretching.[19] Analysis of the copolymerized films indicates that all of the functional groups present in the single-gas deposited films appear in the copolymerized films. Thus, different amounts of CN, C-O-R, and NH are observed in the spectra of copolymerized films that are correlated to the concentration of allylNH in the gas feed. High

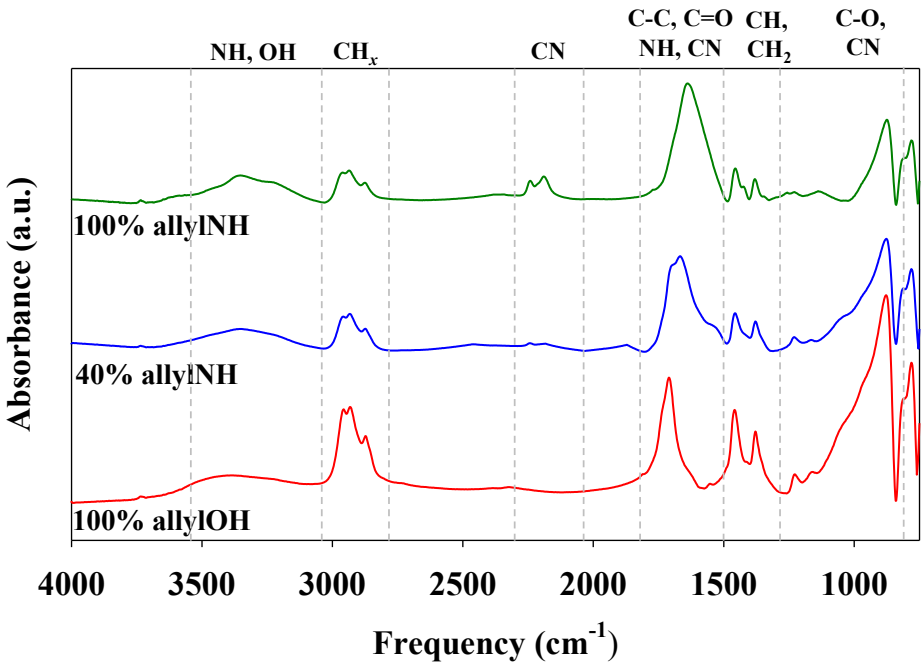


**Figure 6.3.** FTIR spectra for films deposited in CW allylOH/allylNH plasmas. Notable functional group assignments are listed at the top of the figure. Dashed lines represent the spectral regions corresponding to these assignments.

concentrations of allylNH in the feed result in more intense N-H/O-H absorbance bands. Because the oxygen content of the film is relatively low, the higher intensity of the N-H/O-H peak in 100% allylNH films can be attributed to more $NH_x$ in the films. The appearance of the C-N/C=O peak in the high resolution $C_{1s}$ XPS spectra of 100% allylNH films supports this hypothesis. For copolymerized films, the intensity of FTIR absorbance bands associated with $NH_x$ functional groups is correlated to the concentration of allylNH in the feed.

Determining the exact structure of *pp*-allylNH is difficult because of overlapping signals in both XPS and FTIR spectra. Literature data for both *pp*-allylOH and *pp*-allylNH films can, however, help elucidate general characteristics of the films produced here. Depositions using 100% allylOH CW plasmas yield *pp*-allylOH films that chiefly consist of hydrocarbon, ether, and alcohol functional groups. Proposed deposition mechanisms outlined by Watkins[21] and O'Toole[1,3] and depicted in Section 1.2 indicate that *pp*-allylOH films deposited under highly fragmenting, CW plasma conditions produce films with oxygen bound primarily in ether functionality. Our high-resolution XPS data confirm similar binding in our films, which is further substantiated by the FTIR data in Fig. 6.3. Indeed, FTIR spectra for films deposited using 100% allylOH plasmas display strong absorbance bands associated with C-O groups and weak OH absorbance relative to that of the C-C and C-H stretches. Derivatization studies by Gallino[19] and mass spectrometry studies by Beck[31] show that *pp*-allylNH films can have a high concentration of primary amines, however, the addition of allylOH to the gas feed produces C-N-O and C-O functionalities, which complicates the identification of primary amines in our materials using XPS or FTIR, as discussed above.

After plasma treatment, active surface sites and surface rearrangement can lead to oxygen uptake as the films age.[32,33] Here, the most oxygen uptake occurs in films deposited from larger

concentrations of allylNH in the gas feed. Specifically, the O/C ratio increases ~185% over the 1 month aging period for films deposited in 100% allylNH plasmas and ~35% for films deposited in 0% allylNH plasmas. Moreover, a 99% increase in the O/C ratio for films deposited in 100% allylNH plasmas occurs within the first 24 hours after deposition, which is characteristic of plasma deposited allylNH films.[2,4-6,19,31,34,35] As *pp*-allylNH films age, additional oxygen is gained in the form of imines, amides, hydroxylamines, and nitro compounds as outlined in schemes by Wertheimer, Unger, and others.[2,8-10,26,27,36] In contrast to the 100% allylNH deposited films, the O/C ratio slightly decreases over the 1 month aging period for 100% allylOH films, which has been attributed to oxygen species diffusing of low molecular weight species from the surface into the bulk, and is thoroughly described by the Unger group elsewhere.[37]

As discussed in the Introduction, the wettability of a film can affect how a material behaves in biological applications. Figure 6.4 shows WCA data as a function of allylNH in the gas feed. For mixed-gas precursor systems (20-80% allylNH), the WCAs for freshly deposited films linearly decrease as a function of increasing allylNH content in the gas feed, with $R^2$ = 0.95. In contrast, the films deposited with 100% allylOH have a WCA ~5° lower than that of films deposited with 20% allylNH and those deposited with 100% allylNH have a WCA ~5° higher than that of films deposited with 80% allylNH. The WCA for films deposited from mixed-gas systems increases ~10% after the first 24 h of aging, and another ~10% after two weeks, but then decrease after 1 month. Films deposited in allylNH containing plasmas could undergo aging mechanisms outlined in Chapter 1. As such, –OH groups could be incorporated within the film structure after 1 month of aging and could have an effect on the wettability of aged films, as discussed later in this section. As with freshly deposited films, aged films

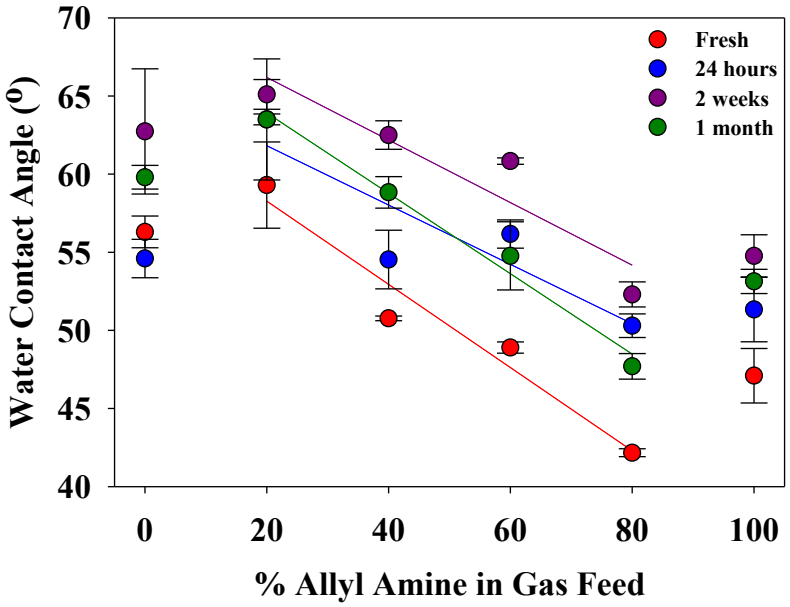


**Figure 6.4.** Water contact angle as a function of allylNH content in the gas feed for films deposited in CW allylOH/allylNH plasmas. Data for freshly deposited and aged films are presented. Lines correspond to linear least squares fits to the data for films deposited in 20-80% allylNH plasmas.

deposited with 20-80% allylNH plasmas decrease linearly with increasing allylNH in the gas feed.

Because the surface roughness of a given sample can affect WCA measurements, each film was analyzed via optical profilometry to account for possible complicating roughness effects in the WCA data. Figure 6.5 shows optical profilometry images including the measured RMS roughness values. Bare Si wafers, Fig. 6.4a, have an RMS roughness of 2.4 ± 0.7 nm, and films deposited from a 100% allylNH CW plasma onto Si wafers are nearly identical in topology, with an RMS roughness of 2.8 ± 0.6 nm, Fig. 6.6b. This is representative of all films deposited in CW plasmas, regardless of gas feed composition, as the average RMS roughness value for films deposited in all allylNH/allylOH CW plasmas was 3.2 ± 0.3 nm (averaged over 3 spots on 3 samples from each plasma system).

It is also important to determine if the WCAs of our films are correlated to their O or N content, as this could provide useful insight into how specific functional groups affect the wettability of plasma copolymerized films. In general, the WCA increases with increasing oxygen content (Fig. 6.6a) and decreases with increasing nitrogen content (Fig 6.6b). These trends hold for all films deposited using CW plasmas, independent of film age, suggesting that materials deposited in plasmas with higher concentrations of allylOH are less hydrophilic than those deposited in plasmas with higher concentrations of allylNH. Moreover, this is supported by Kearns and Short in work showing that allylOH films have larger WCA values than allylNH films.[7,20] One possible explanation for these wetting properties lies in the hydrogen bonding capabilities of the functional groups present within the deposited films. As mentioned above, films deposited in CW allylOH plasmas contain oxygen primarily in ether functional groups and films deposited in CW allylNH plasmas contain amine groups. The hydrogen bonding

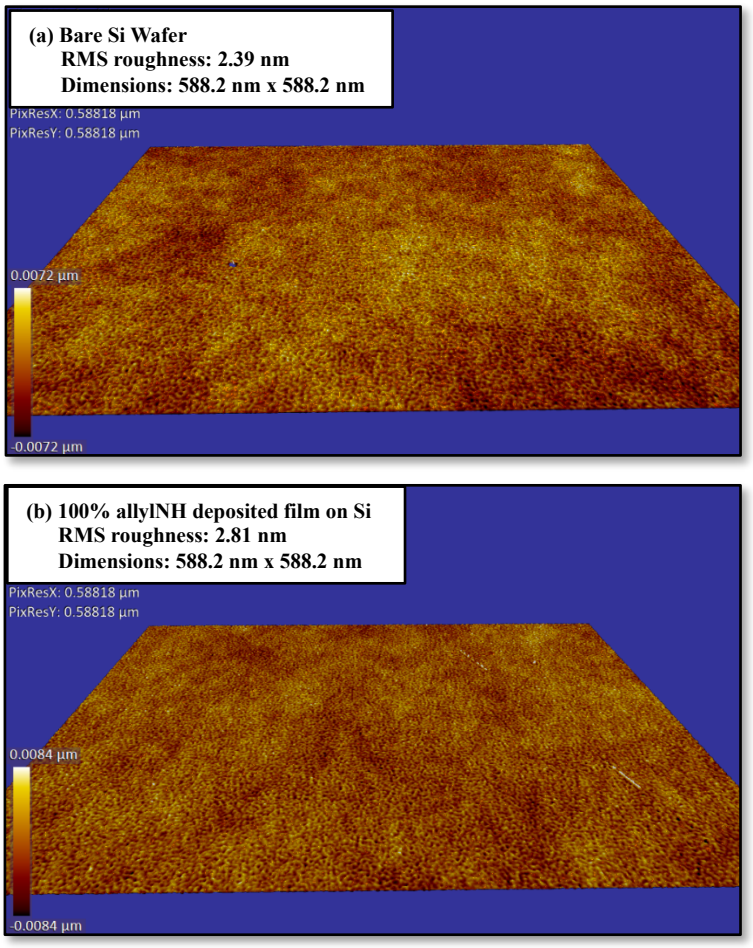


**Figure 6.5.** Optical profilometry images depicting RMS roughness for (a) a bare Si wafer and (b) a film deposited onto a Si wafer in a 100% allylNH plasma under CW conditions.

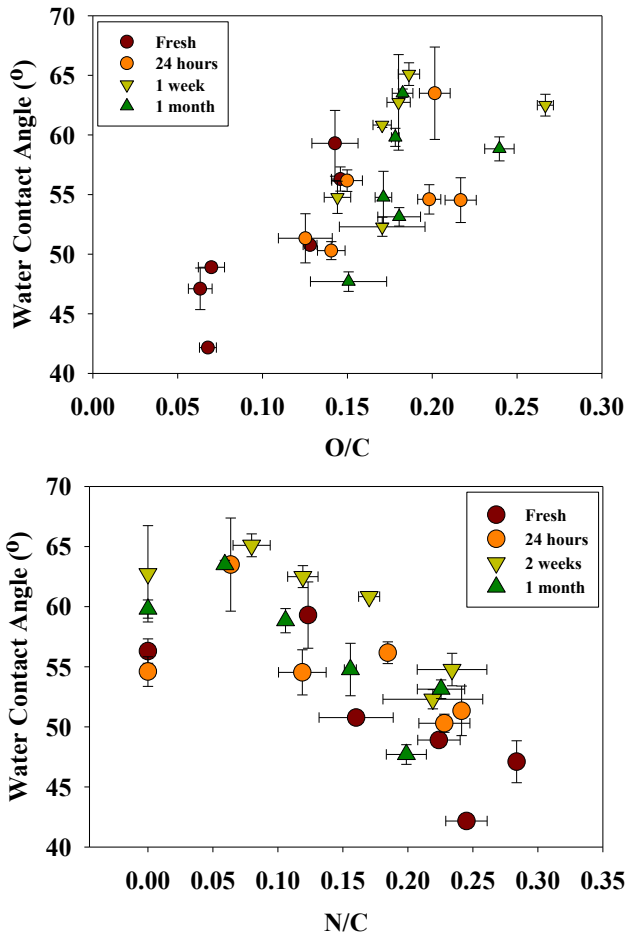


**Figure 6.6.** WCA as a function of O/C and N/C ratios for films deposited in CW allylOH/allylNH plasmas. Data for freshly treated and aged films are presented.

capabilities of $-NH_x$ groups cause films deposited in CW plasmas with high concentrations of allylNH to be more wettable than films deposited with high concentrations of allylOH. Thus, adjusting the relative amounts of the precursor gas can help regulate the wetting properties of the CW plasma deposited allylOH/allylNH films.

### 6.2.2 Pulsed plasma deposited films

As mentioned in Section 1.3, pulsed plasma polymerized films retain much of the functionality of the parent monomer. As such, allylOH and allylNH films deposited under pulsed plasma conditions would be expected to retain alcohol and amine functionalities, respectively, and copolymers of allylOH and allylNH deposited under these conditions would similarly contain both -OH and $-NH_x$ functional groups.

Table 6.2 lists the XPS elemental composition for films deposited in allylNH/allylOH plasmas pulsed at a 5% duty cycle (peak power = 50 W, $P_T$ = 100 mTorr, 9 cm downstream, 15 min). These data are graphically represented in Figure 6.7. The O/C ratio linearly decreases as a function of increasing allylNH in the gas feed, Fig. 6.7a. Upon aging, most of the films oxidize, with greater oxidation observed in films deposited in plasmas with higher concentrations of allylNH in the feed. Specifically, films deposited in 100% allylNH pulsed plasmas incorporate ~13% oxygen over one month, whereas films deposited in 100% allylOH pulsed plasmas do not appreciably oxidize over the same aging period. In Section 1.2, it was discussed that many groups have found *pp*-allylNH films rapidly oxidize when exposed to air, whereas allylOH films do not undergo substantial oxidation processes upon aging. The data presented in Fig. 6.7a support this finding, as films deposited in higher concentrations of allylNH exhibit more oxidation as they age. Thus, the marginal oxidation observed for films deposited in pulsed allylOH plasmas when compared to those deposited in pulsed allylNH plasmas allows us to

**Table 6.2. XPS Elemental Composition of films deposited in pulsed allylNH/allylOH plasmas[a]**

| Sample Age | AllylNH in Feed (%)[b] | C (%) | O (%) | N (%) |
|---|---|---|---|---|
| Fresh | 100 | 71.5 ± 1.4 | 3.7 ± 1.0 | 24.5 ± 1.1 |
| | 80 | 74.3 ± 0.8 | 7.6 ± 0.8 | 18.1 ± 1.4 |
| | 60 | 74.1 ± 1.9 | 9.8 ± 1.0 | 16.0 ± 1.7 |
| | 40 | 76.1 ± 1.2 | 12.3 ± 2.7 | 11.7 ± 2.8 |
| | 20 | 77.7 ± 1.4 | 20.2 ± 0.6 | 2.0 ± 0.9 |
| | 0 | 74.4 ± 0.6 | 25.6 ± 0.6 | 0.0 ± 0.0 |
| 24 h | 100 | 67.8 ± 1.4 | 11.5 ± 0.9 | 20.8 ± 0.7 |
| | 80 | 71.3 ± 0.8 | 12.2 ± 0.8 | 16.2 ± 0.7 |
| | 60 | 71.5 ± 1.4 | 13.7 ± 0.8 | 14.8 ± 0.7 |
| | 40 | 73.6 ± 2.5 | 17.8 ± 0.4 | 8.6 ± 2.0 |
| | 20 | 73.3 ± 1.1 | 25.9 ± 0.5 | 0.8 ± 0.7 |
| | 0 | 77.8 ± 0.7 | 22.2 ± 0.7 | 0.0 ± 0.0 |
| 1 month | 100 | 64.8 ± 0.3 | 16.6 ± 0.9 | 18.7 ± 1.1 |
| | 80 | 66.4 ± 0.1 | 17.9 ± 0.4 | 15.7 ± 0.4 |
| | 60 | 67.5 ± 0.7 | 20.1 ± 0.3 | 12.4 ± 0.8 |
| | 40 | 70.3 ± 0.5 | 22.1 ± 0.4 | 7.6 ± 0.2 |
| | 20 | 71.6 ± 0.4 | 26.0 ± 0.4 | 2.4 ± 0.1 |
| | 0 | 72.6 ± 0.9 | 27.0 ± 1.2 | 0.0 ± 0.0 |

[a]All films were produced in pulsed plasmas with $P$ = 50 W, 5% d.c., total pressure of 100 mTorr, treatment time of 15 min, and substrate location = 9 cm downstream from the coil.

[b]Remainder of feed gas composition was allylOH.

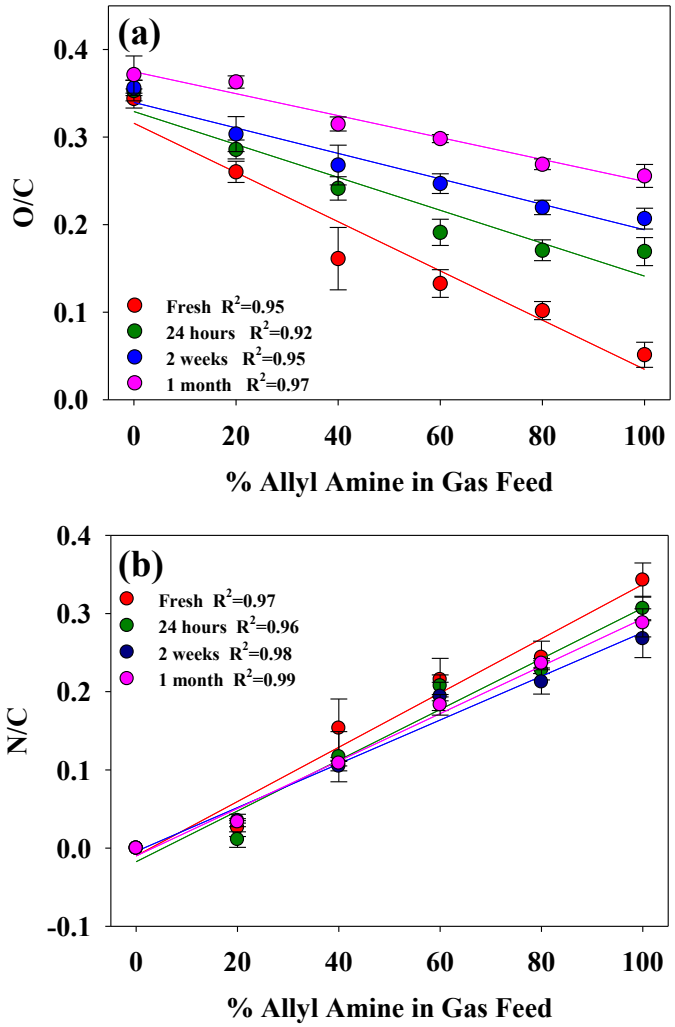


**Figure 6.7.** O/C and N/C ratios for films deposited in pulsed allylOH/allylNH plasmas as a function of feed gas composition. Data were fit with a linear least squares analysis; $R^2$ values for the fits are reported in the figure legend.

attribute the majority of the oxidation upon aging to functional groups contributed by the allylNH precursor.

In contrast to the O/C ratio, the N/C ratio for freshly deposited films linearly increases with the allylNH in the gas feed. Furthermore, the N/C ratio does not substantially change upon aging except for the films deposited in 100% allylNH pulsed plasmas, where ~6% N is lost over the 1 month aging period. The propensity of these films to retain N is observed for both pulsed and CW plasma deposition systems and is beneficial when considering applications in which shelf-life and nitrogen-retention are important. Furthermore, both the O/C and N/C ratios show strong linear correlations ($R^2 \geq 0.92$) to the allylNH concentration in the gas feed, regardless of film age. The ability to predict film composition for these copolymerized systems is key to achieving the preferred atomic concentrations for specific applications. The linearity observed for the pulsed plasma copolymerized films nicely allows for the straightforward prediction of film composition.

Figure 6.8 shows high-resolution $C_{1s}$ XPS spectra and their accompanying theoretical deconstruction into component peaks for films deposited in pulsed plasmas using gas feeds containing 100% allylOH, 40% allylNH, and 100% allylNH. Binding environments were deconstructed in a manner similar to that reported in Section 6.2.1. Specifically, C-C/C-H, C-OH/C-OR, and O-C-O/C=O environments are observed in films produced with 100% allylOH, Fig. 6.8a,d. Freshly deposited films from 100% allylNH plasmas contain C-C/C-H, N-C/C=O, and C=O/O-C-O environments, Fig. 6.8b, with the C-OH/C-OR environment appearing in spectra of aged films, Fig. 6.8e. Films deposited in pulsed mixed gas systems contain combinations of the binding environments present in films deposited under single-gas conditions, Fig. 6.8c. High-resolution $C_{1s}$ XPS spectra show a significantly larger C-OH/C-OR binding

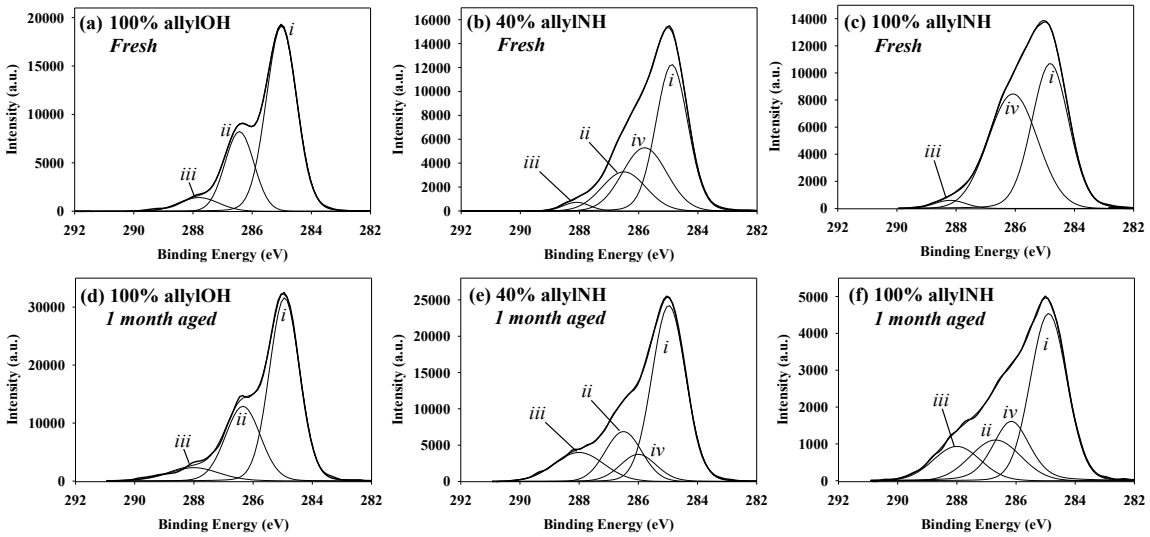


**Figure 6.8.** High resolution $C_{1s}$ XPS spectra for the films deposited in pulsed plasmas containing 100% allylOH, 40% allylNH, and 100% allylNH. Data for (a-c) freshly deposited and (d-f) aged films are shown. The labeled binding environments correspond to (*i*) C-C/C-H, (*ii*) C-OH/C-OR, (*iii*) N-C=O/C=O, and (*iv*) N-C/C=O.

environment for films deposited in 100% allylOH plasmas under pulsed conditions as compared to those for films deposited under CW conditions, which is typical for pulsed *pp*-allylOH films.[1,3,21,22]

Figure 6.9 contains FTIR spectra for films deposited under pulsed plasma conditions for various gas mixtures, with the same peak assignments as in Fig. 6.3. Strong absorbance bands corresponding to -$NH_x$ and -OH functional groups are observed. The dramatic increase in O-H stretching relative to C-H stretching in the spectrum of films deposited in pulsed 100% allylOH plasmas indicates more oxygen is bound in alcohol groups. This agrees well with literature results for pulsed *pp*-allylOH depositions from our group and others.[25,29]

As with CW deposited films, detailed analysis of the pulsed plasma deposited 100% allylNH films is hindered partially because of the immediate oxygen incorporation that occurs upon exposure to atmosphere, and the overlap of oxygen and nitrogen containing signals in XPS and FTIR spectra. The high-resolution XPS data in Fig. 6.8c,f reveal that the films deposited in 100% allylNH plasmas are similar to those deposited under CW conditions, which is a trend also observed elsewhere in the literature.[19,23,31]

WCA values as a function of allylNH in the gas feed are shown in Figure 6.10. The WCAs for freshly deposited copolymer films increase linearly as a function of increasing allylNH in the gas feed. The WCA for films freshly deposited in single-gas systems deviate from this trend, similar to CW plasma deposited films. Upon aging, films deposited in plasmas with ≤40% allylNH behave differently than films deposited with gas feeds ≥60% allylNH. Specifically, WCAs for films deposited in ≤40% allylNH plasmas are similar, which suggests these films do not undergo significant hydrophobic recovery during the 1 month aging period. Films deposited in ≥60% allylNH plasmas initially have significantly higher WCAs than those

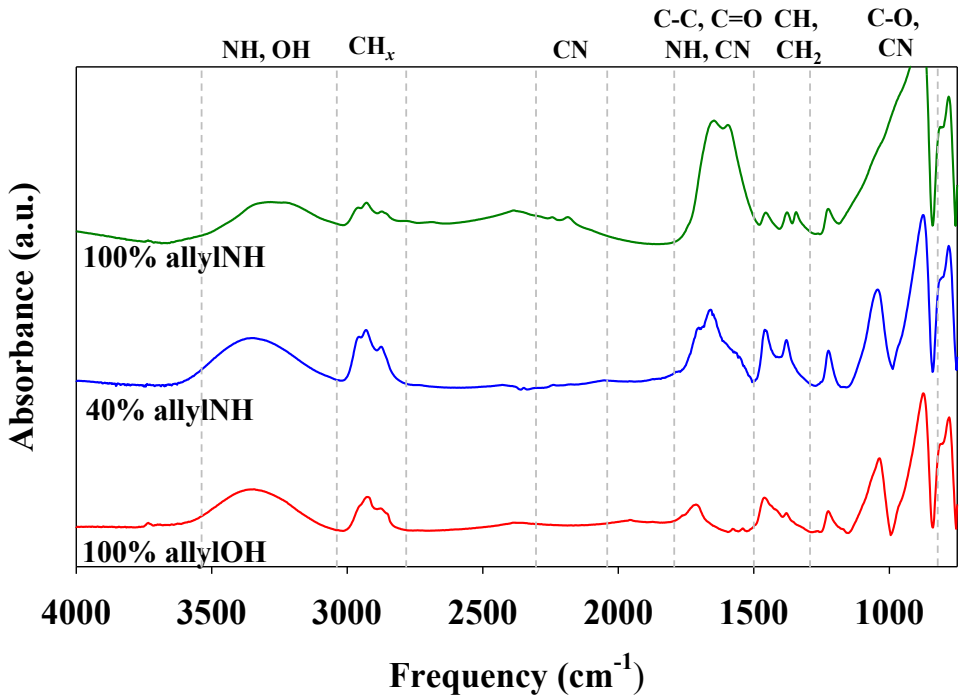


**Figure 6.9.** FTIR spectra for films deposited in pulsed allylOH/allylNH plasmas. Notable functional group assignments are listed at the top of the figure. Dashed lines represent the spectral regions corresponding to these assignments.

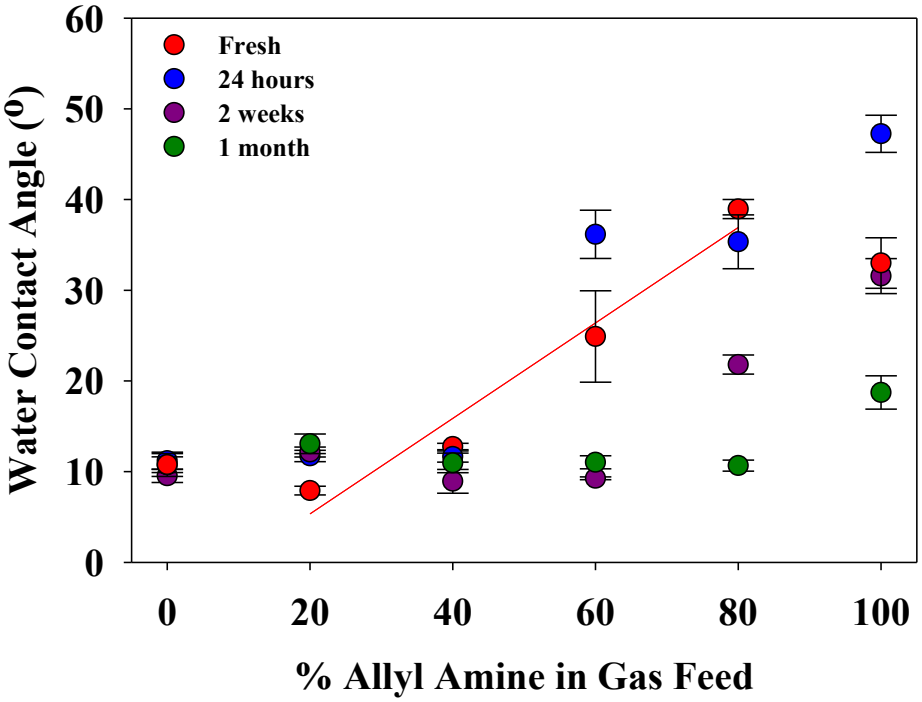


**Figure 6.10.** WCA as a function of plasma gas feed for films deposited in pulsed allylOH/allylNH plasmas. The red line represents a linear least squares fit to data for freshly deposited films in 20-80% allylNH pulsed plasmas.

deposited in lower concentrations of allylNH. Upon aging for 24 h, the higher WCA values are retained, but over the remainder of the 1 month aging period, the WCA values for films deposited in ≥60% allylNH decrease and become comparable to those of films deposited in ≤40% allylNH plasmas. At the end of the aging period, all WCAs, independent of plasma composition, are the same within ±5°.

Comparing WCA data to the O/C data in Fig. 6.7a reveals that the films with the largest WCA changes during the aging period are also those that experience the most oxidation during aging. To further explore this, WCA values were analyzed as a function of O/C and N/C ratios of the films, Fig. 6.11. Generally, the WCA decreases as the O/C ratio increases (Fig. 6.11a) for freshly deposited films and films aged 24 h, but become similar after aging for 1 month, independent of O/C content within the film. Freshly deposited films with N/C ratios < 0.2 yield WCAs < ~20°, Fig. 6.11b. WCAs > 20° are observed for freshly deposited films that contain N/C ratios between 0.2-0.4. The trend is observed over the first 2 weeks of aging. However, after 1 month of aging, the WCAs decrease and are similar for all N/C ratios. As the films age, more hydrophilic O groups, some in the form of alcohol groups due the aging mechanisms of allylNH, are incorporated into the film structure which can result in an increased wettability.[7,21,24,38] This suggests that the oxygen within the film plays a larger role than nitrogen in the wettability of the pulsed plasma deposited films.

Although this is in direct opposition to the data for CW plasma deposited films, the disparity can be reconciled when the differences in film structure are considered. Films deposited under pulsed plasma conditions retain a high degree of –OH groups from the allylOH precursor, and therefore have the ability to hydrogen bond when compared to the ether functionality in the CW deposited films. Because oxygen is much more electronegative than

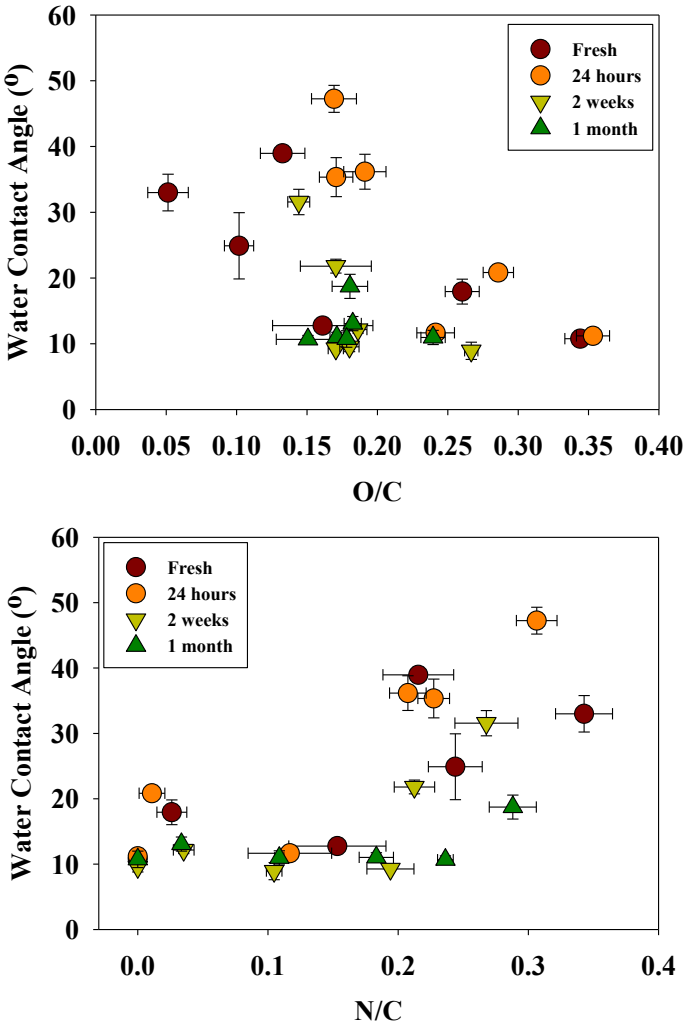


**Figure 6.11.** WCA as a function of O/C and N/C ratios for films deposited in pulsed allylOH/allylNH plasmas. Data for freshly treated and aged films are presented.

nitrogen, the more polar –OH functionality produced from the allylOH portion of the plasma gas increases the films wettability more than the less polar $–NH_x$ functional groups produced from allylNH. Thus, knowing the relative –OH content of a film can provide a general metric for assessing the films general hydrophilic properties.

## 6.4 Summary

This chapter details the plasma deposition of functionalized films copolymerized from allylNH and allylOH. Two distinct film types were created, those deposited under CW plasma conditions and those deposited under pulsed plasma conditions. Copolymer films deposited under CW conditions exhibit properties of both *pp*-allylOH and *pp*-allylNH films. The ester and amine groups within the copolymerized films resulted in a positive linear dependence of WCA on nitrogen content. Furthermore, the WCA increased with increasing O/C and decreased with increasing N/C. In contrast, the WCA for pulsed plasma deposited copolymer films decreased with increasing O/C and increased with increasing N/C. These trends suggest the WCA is directly related to the oxygen content and functionality in the films. Specifically, -OH groups created in the pulsed plasma deposited films lead to more wettable surfaces than the ether groups incorporated into films deposited from CW plasmas. Overall, WCAs for CW deposited films were higher than pulsed plasma deposited films, which could suggest the latter may be better for applications requiring high cell-surface affinity. Ultimately, this work sets the stage for additional studies of cell behavior on allylNH/allylOH copolymer films, specifically as it relates to surface composition and film hydrophilicity.

REFERENCES


[1] L. O'Toole, C. A. Mayhew, and R. D. Short, J. Chem. Soc., Faraday Trans. **93**, 1961 (1997).

[2] T. Jacobs, R. Morent, N. Geyter, P. Dubruel, and C. Leys, Plasma Chem Plasma Process **32**, 1039 (2012).

[3] L. O'Toole and R. D. Short, J. Chem. Soc., Faraday Trans. **93**, 1141 (1997).

[4] R. Förch, A. N. Chifen, A. Bousquet, H. L. Khor, M. Jungblut, L. Q. Chu, Z. Zhang, I. Osey-Mensah, E. K. Sinner, and W. Knoll, Chem. Vap. Deposition **13**, 280 (2007).

[5] R. Di Mundo, M. Nardulli, A. Milella, P. Favia, R. d'Agostino, and R. Gristina, Langmuir **27**, 4914 (2011).

[6] D. Mangindaan, C.-T. Chen, and M.-J. Wang, Applied Surface Science **262**, 114 (2012).

[7] V. Kearns, A. Mistry, S. Mason, Y. Krishna, C. Sheridan, R. Short, and R. L. Williams, J Mater Sci: Mater Med **23**, 2013 (2012).

[8] F. Renò, D. D'Angelo, G. Gottardi, M. Rizzi, D. Aragno, G. Piacenza, F. Cartasegna, M. Biasizzo, F. Trotta, and M. Cannas, Plasma Processes Polym. **9**, 491 (2012).

[9] F. Intranuovo, P. Favia, E. Sardella, C. Ingrosso, M. Nardulli, R. d'Agostino, and R. Gristina, Biomacromolecules **12**, 380 (2011).

[10] K. S. Siow, L. Britcher, S. Kumar, and H. J. Griesser, Plasma Processes Polym. **3**, 392 (2006).

[11] M. T. Khorasani, H. Mirzadeh, and S. Irani, J. Appl. Polym. Sci. **112**, 3429 (2009).

[12] E. D. Yildirim, R. Besunder, D. Pappas, F. Allen, S. Güçeri, and W. Sun, Biofabrication **2**, 014109 (2010).

[13] E. D. Yildirim, H. Ayan, V. N. Vasilets, A. Fridman, S. Güçeri, and W. Sun, Plasma Processes Polym. **5**, 58 (2008).

[14] H. Park, J. W. Lee, K. E. Park, W. H. Park, and K. Y. Lee, Colloids and Surfaces B: Biointerfaces **77**, 90 (2010).

[15] L. Garrido, I. Jiménez, G. Ellis, P. Cano, J. M. García-Martínez, L. López, and E. de la Peña, J. Appl. Polym. Sci. **119**, 3286 (2010).

[16] M. T. Khorasani, H. Mirzadeh, and S. Irani, Radiation Physics and Chemistry **77**, 280 (2008).

[17] A. G. Shard, J. D. Whittle, A. J. Beck, P. N. Brookes, N. A. Bullett, R. A. Talib, A. Mistry, D. Barton, and S. L. McArthur, J. Phys. Chem. B **108**, 12472 (2004).

[18] A. J. Beck, J. D. Whittle, N. A. Bullett, P. Eves, S. Mac Neil, S. L. McArthur, and A. G. Shard, Plasma Processes Polym. **2**, 641 (2005).

[19] E. Gallino, S. Massey, M. Tatoulian, and D. Mantovani, Surface & Coatings Technology **205**, 2461 (2010).

[20] L. M. Gomez, P. Morales, G. J. Cruz, M. G. Olayo, C. Palacios, J. Morales, and R. Olayo, Macromol. Symp. **283-284**, 7 (2009).

[21] L. Watkins, A. Bismarck, A. F. Lee, D. Wilson, and K. Wilson, Applied Surface Science **252**, 8203 (2006).

[22] A. J. Beck, F. R. Jones, and R. D. Short, Polymer **37**, 5537 (2003).

[23] T. Hirotsu, C. Tagaki, and A. Partridge, Plasmas and Polymers **7**, 353 (2002).

[24] M. Richard, D. Robert, E. Duval, F. R. Jones, R. A. Dawson, and S. MacNeil, Chem. Mater. **10**, 1176 (1998).

[25] A. Fahmy, R. Mix, A. Schönhals, and J. F. Friedrich, Plasma Chem Plasma Process **31**, 477 (2011).
[26] A. J. Beck, S. Candan, R. M. France, F. R. Jones, and R. D. Short, Plasmas and Polymers **3**, 97 (1998).
[27] J.-C. Ruiz, A. St-Georges-Robillard, C. Thérésy, S. Lerouge, and M. R. Wertheimer, Plasma Processes Polym. **7**, 737 (2010).
[28] L. J. Gerenser, Journal of Adhesion Science and Technology 303 (1987).
[29] J. C. Shearer and E. R. Fisher, Nanosci Nanotechnol Lett **4**, 358 (2013).
[30] B. Yameen, H. U. Khan, W. Knoll, R. Förch, and U. Jonas, Macromol. Rapid Commun. **32**, 1735 (2011).
[31] A. J. Beck, S. Candan, R. D. Short, A. Goodyear, and N. S. J. Braithwaite, J. Phys. Chem. B **105**, 5730 (2001).
[32] M. L. Steen, A. C. Jordan, and E. R. Fisher, Journal of Membrane Science **204**, 341 (2002).
[33] H. Biederman, *Plasma Polymer Films* (World Scientific Publishing Compant, n.d.).
[34] N. Moreau, O. Feron, B. Gallez, B. Masereel, C. Michiels, T. Vander Borght, F. Rossi, and S. Lucas, Surface & Coatings Technology **205**, S462 (2011).
[35] X. Wang, J. Wang, Z. Yang, Y. Leng, H. Sun, and N. Huang, Surface & Coatings Technology **204**, 3047 (2010).
[36] J. Friedrich, R. Mix, G. Kühn, I. Retzko, A. Schönhals, and W. Unger, Composite Interfaces **10**, 173 (2003).
[37] S. Swaraj, U. Oran, A. Lippitz, J. F. Friedrich, and W. E. S. Unger, Plasma Processes Polym. **4**, S784 (2007).
[38] R. Chen and M. S. Silverstein, Journal of Polymer Science Part a: Polymer Chemistry **34**, 207 (2000).

# CHAPTER 7

# PLASMA SURFACE MODIFICATION OF 3D POLYCAPROLACTONE SCAFFOLDS USING $H_2O/N_2$ PLASMAS

The data presented in this chapter were collected as part of a collaboration established through the ACS Global Research Experiences, Exchanges, and Training (GREET) Program, and completed at the University of Bari (Bari, Italy) in the laboratories of Prof. Pietro Favia. Plasma treatments and contact angle measurements were performed by Prof. Ellen R. Fisher, Marta Grazia, Dr. Eliosa Sardella, and me. XPS data collection was performed by Dr. Sardella and analyzed by me. Biological experiments were performed under the direction of Dr. Roberto Gristina, with initial experiments performed by Prof. Ellen R. Fisher and me and replicate experiments performed by Dr. Gristina. Results showed that plasma treated scaffolds were more wettable, had higher water absorption rates, and exhibited enhanced cell growth over non plasma-treated scaffolds. As of the time of this writing, this body of work is being prepared for an invited article in *ACS Applied Materials and Interfaces*.

## 7.1 Introduction

In the proceeding chapters, plasma deposition was used to create thin films that enhanced the surface functionality of the underlying substrate. For certain applications, it might be it beneficial to enhance surface functionality by implanting functional groups through surface activation processes rather than depositing a thin film as discussed at the end of Chapter 5. In this chapter, we explore the plasma surface modification of three dimensional (3D) biodegradable polymeric scaffolds.

Polymeric scaffolds have attracted significant attention recently because they can act as the structural backbone for cell and tissue growth.[1-5] The 3D nature of the scaffolds mimics the architecture of tissues, bones, and cartilage found in the human body,[1] thereby making them novel substrates for tissue engineering applications. Tateishi et al. outlined several considerations when fabricating scaffolds for these purposes.[3] The surface of the scaffolds must promote cell adhesion and growth while retaining the functions of the growing cells. The scaffolds should be biocompatible and biodegradable, and the porosity of the 3D structure should be such that there is space for cell adhesion and allow for even cell distribution to enable homogeneous tissue formation.[3] However, limitations associated with synthetic materials, such as non-ideal surface properties that promote cell growth, require surface treatments to maximize the benefits of these materials.[1]

Some of the more popular materials used in fabricating polymer scaffolds are poly $_{D,L}$-lactic acid (PLA) and poly(ε-caprolactone) (PCL). Tailoring a scaffold's surface for very specific applications is essential for these materials to be biologically relevant. Although a range of plasma chemistries have been explored to accomplish this task, many studies have concentrated on depositing thin films onto the 3D scaffolds to create a highly functionalized surface. For example, Intranuovo and coworkers plasma deposited allylamine coatings onto PCL scaffolds to increase the cell growth of Saos2 osteoblasts.[4] Additionally, Yen and coworkers demonstrated that grafting poly(ethylene glycol) (PEG) onto PCL scaffolds can increase biofouling and prevent fibroblast adhesion on the surface of the scaffolds.[6] Additional background detailing plasma deposition methods on polymeric scaffolds can be found in Section 8.1.

Although there are significant literature studies showing that plasma processing can enhance cell growth on polymeric surfaces, it has been suggested that the most influential factors on cell growth are surface wettability,[7,8] surface chemistry,[9-13] and surface roughness.[8,13-15] A variety of studies have shown that cell growth is enhanced on plasma treated, plasma oxidized surfaces such as poly($_{D,L}$-lactide-co-glycolide) and poly ($_{L}$-lactide).[8,13,15] They all attribute the enhanced growth on the added wettability caused by the addition of polar oxygen-containing groups. However, there is an ongoing debate within the literature about what surface properties promote cell growth. While the previous authors attributed surface oxygen functional groups to enhanced cell growth, Khorasani and Wan[13] theorized that enhanced growth to increases in surface roughness caused by the plasma processing.

Chu, Yang, and others have suggested that the nitrogen content of a surface is directly related to enhanced cell growth at the surface[10] due to increases in wettability and enhanced cell-surface interactions.[9,16] Specifically, Chu states that amine groups implanted via plasma processing ionically bond with acidic groups on the surface of the cell membrane and cause better cell adhesion and growth. These authors also suggest that a more hydrophilic surface can contribute to better attachment of cell binding proteins. Clearly, increasing the wettability and nitrogen content on a polymer's surface can affect cell growth on surfaces.

Thus, in this study, we utilize $N_2$ and $H_2O$ vapor plasmas to modify PCL scaffolds with the intent to increase the scaffolds' wettability and implant nitrogen-containing functional groups on the external surface of the scaffold and throughout scaffolds' core such that Saos2 osteoblast cell growth is promoted. Although studies have reported successful cell growth on PLA[17] and PCL[5] scaffolds, few have explicitly detailed the wettability changes associated with plasma processing of these materials. Thus, we shall not only focus on changing the surface

functionality of the scaffolds, but also on changing the scaffolds' wettability. The ability to relate wettability and surface functionality to cell growth will allow for a greater understanding of how these materials might interact in biological systems.

### 7.2 Results and Discussion

PCL scaffolds were treated in various mixtures of $N_2$ and $H_2O$ vapor plasmas in the translating electrode plasma reactor described in Section 2.1.1. WCA characterization was performed on the tops, cross-sections, and bottoms of scaffolds treated in various mixtures of $N_2/H_2O$ plasmas under static conditions. Figure 7.1 shows the WCA at $t = 0$ as a function of $H_2O_{(g)}$ in the plasma gas feed. PCL scaffolds are natively hydrophobic with WCAs of 130 ± 5°, which can decrease ~30° upon plasma treatment. The WCA for the top and bottom of scaffolds treated in 100% $H_2O_{(g)}$ plasmas is significantly lower than that of untreated PCL scaffolds. The top and cross sections of scaffolds treated in 50/50 $N_2/H_2O$ mixtures exhibited WCAs within statistical error of untreated scaffolds; however, it should be noted that the error on these samples is quite high, which we attributed to the incredibly high absorption rates observed immediately after plasma treatment. Water drops for these samples were completely absorbed into the scaffold in < 6 ms, making measurements of WCA and drop volume challenging. As observed in Fig. 7.1, WCAs for all plasma treated scaffolds were statistically the same, independent of plasma treatment. WCA values for the scaffold cross sections are similar to that of untreated PCL. Note that these plasma modification methods are generally regarded as treating only the outermost surface of a material. Thus, when the scaffolds are cross-sectioned, the hydrophobic, untreated bulk material is exposed, thereby causing the absorption characteristics of the cross section to closely resemble that of untreated PCL.

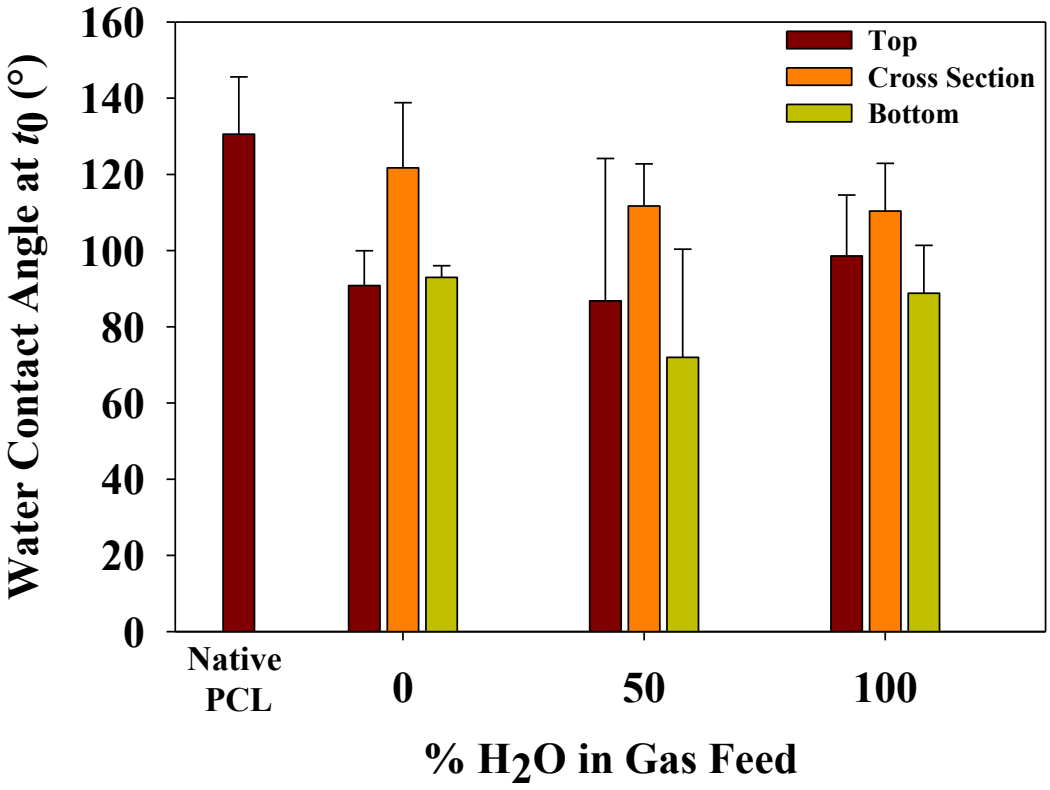


**Figure 7.1.** Water contact angle as a function of $H_2O$ concentration in the gas feed. Measurements taken on the top, bottom, and interior (cross section) are shown.

Figure 7.2 shows the water absorption rate on plasma treated scaffolds as a function of $H_2O$ in the gas feed. The tops and bottoms of scaffolds treated in 100% $H_2O$ plasmas exhibit the highest water absorption rates (185.8 ± 42.4 $\mu$L/s and 112.0 ± 40.2 $\mu$L/s, respectively). In contrast, scaffolds treated in 100% $N_2$ plasmas exhibited the slowest absorption rate (~ 5 $\mu$L/s for both the top and bottom) immediately after plasma treatment. Untreated PCL scaffolds do not absorb water, so all scaffolds treated under all plasma conditions showed enhanced water absorption relative to native PCL. For cross-section measurements, only those scaffolds treated in a 50/50 $N_2/H_2O$ plasma showed non-negligible absorption properties. Again, it should be noted that a significant amount of the untreated, hydrophobic PCL is exposed in the cross-sectioning process, undoubtedly affecting the absorption characteristics.

The absorption rate of the scaffolds was monitored over one week to evaluate the aging properties, Figure 7.3. Within the first 24 hours after plasma treatment, the absorption rate for all plasma treated scaffolds dropped from > 100 $\mu$L/s to ~40 $\mu$L/s. Although the top of the $H_2O_{(g)}$ plasma treated scaffolds exhibited slightly enhanced absorption rates over the bottom immediately after plasma treatment, Figure 7.3a, there was little difference between the two sides after 24 hours. In contrast, both sides of 50/50 $N_2/H_2O$ plasma treated scaffolds had similar absorption properties immediately upon plasma treatment. After 1 week, the tops of the scaffolds showed slightly enhanced absorption properties over that of the bottom surfaces. Although the absorption rate for scaffolds treated in a 100% $N_2$ plasma is significantly lower than those for scaffolds treated under other plasma conditions, they still absorb water throughout the 1 week aging period. Independent of the gas feed compositions used in these studies, plasma treatments render the scaffolds wettable, which lasts a minimum of 7 days. We attribute much of this to the chemical composition of the surface, discussed below.

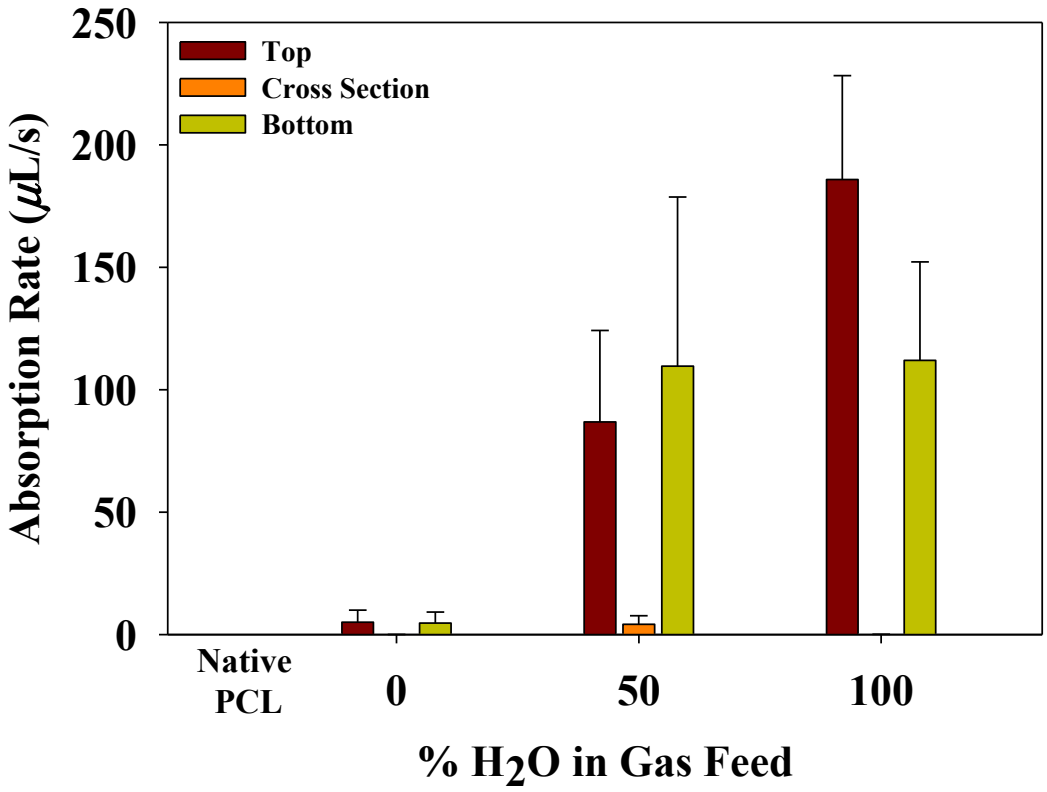


**Figure 7.2.** Initial water absorption rate as a function of $H_2O_{(g)}$ in the gas feed for various positions on the scaffold. For clarity, native PCL does not absorb water and does not have data bars on the plot.

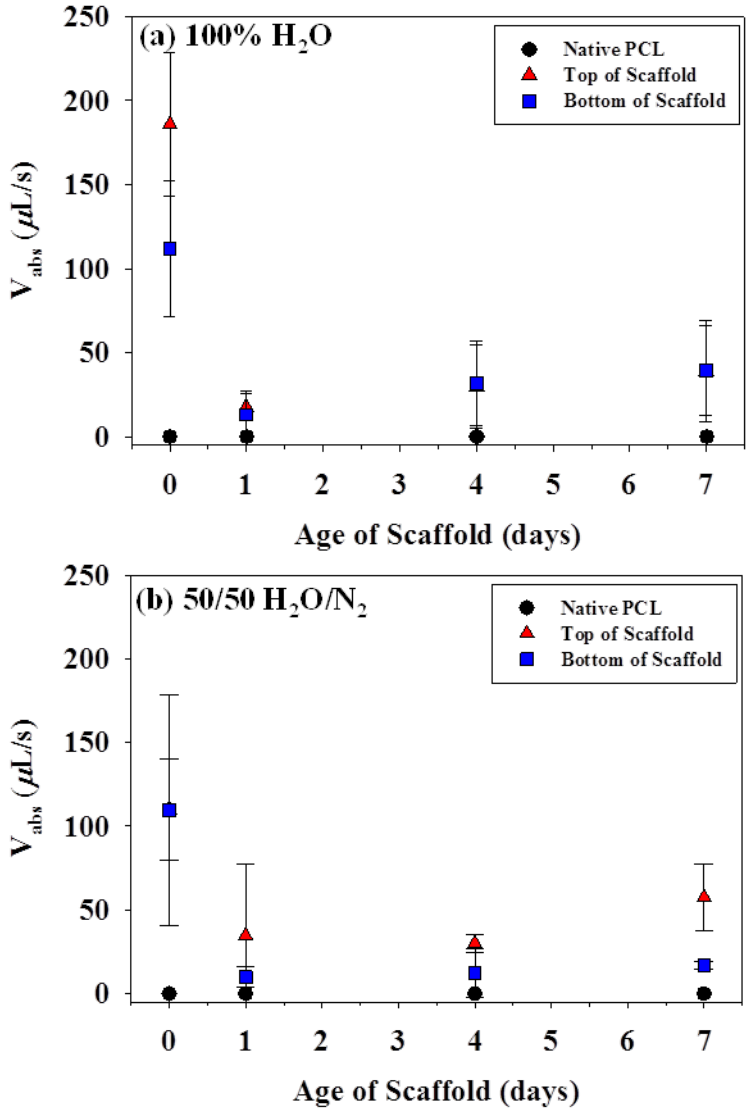


**Figure 7.3.** Initial water absorption rate as a function of age for scaffolds treated in a **(a)** 100% $H_2O$ plasma and **(b)** 50/50 $H_2O/N_2$ plasma.

As mentioned in Section 7.1, one of the criteria for biologically relevant scaffolds is having a porosity such that cells have adequate space for adhesion and proliferation. The porosity of scaffolds needs to be maintained upon plasma treatment so that cell migration can take place and form 3D tissues. Furthermore, changes in surface morphology alone (regardless of porosity) can affect the nature in which cells grow.[8] The porosity of the scaffolds was examined both prior to and after plasma treatment to evaluate any plasma-induced damage that may occur upon treatment. Figure 7.4 shows SEM images for the top (Fig. 7.4a) and cross-section (Fig. 7.4b) of untreated PCL scaffolds. The porous nature of the scaffold is most evident upon cross-sectioning. The morphology of the top of the scaffold can be partially attributed to the surface of molds used in casting process. The porous structure of the scaffolds is maintained after treatment in a 100% $H_2O_{(g)}$ plasma (Fig. 7.4c,d). These images are representative of all scaffolds treated under all gas feed ratios.

The chemical compositions of the scaffolds were analyzed as a function of gas feed composition and location throughout the scaffold cross section. Figure 7.5 shows cross-sectional analysis of the N/C and O/C ratios for scaffolds treated using the three plasma compositions explored here. The inset demonstrates the locations within the cross section where the analysis occurred. Data presented are average values obtained from samples treated under both static and translating electrode conditions, as data confirmed that there were no statistical differences in the elemental composition between the different treatments. All plasma treatments change the chemical functionality of both the external and internal surface of the scaffolds (theoretical O/C = 0.33 for untreated scaffolds). Notably, uniform N/C ratios were observed for the scaffolds treated in a 50/50 $N_2/H_2O$ plasma.

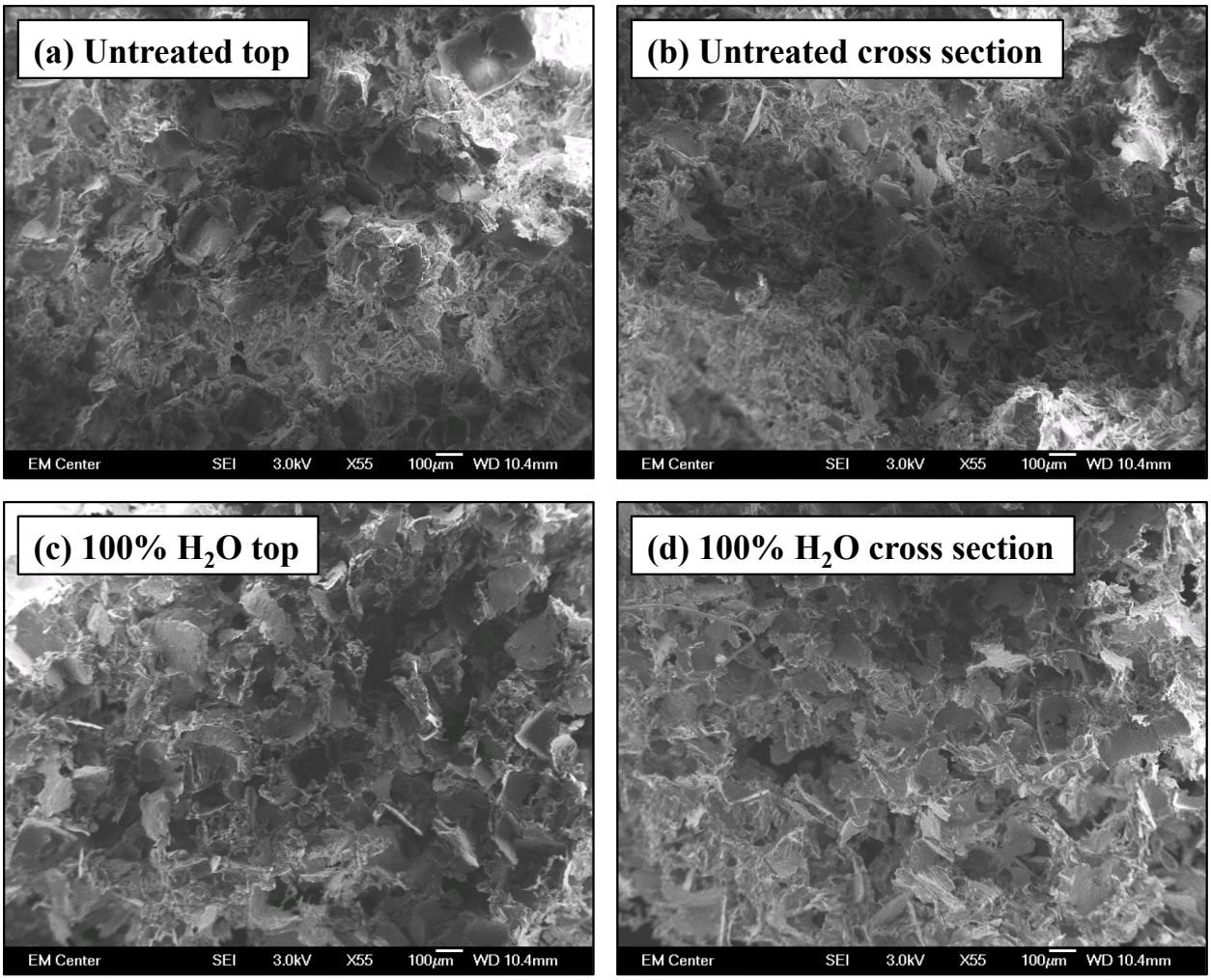


**Figure 7.4.** SEM images for **(a-b)** untreated scaffolds and **(c-d)** scaffolds treated in a 100% $H_2O_{(g)}$ plasma. Images shown in 7.4a-b are representative of all plasma modified scaffolds discussed in this chapter.

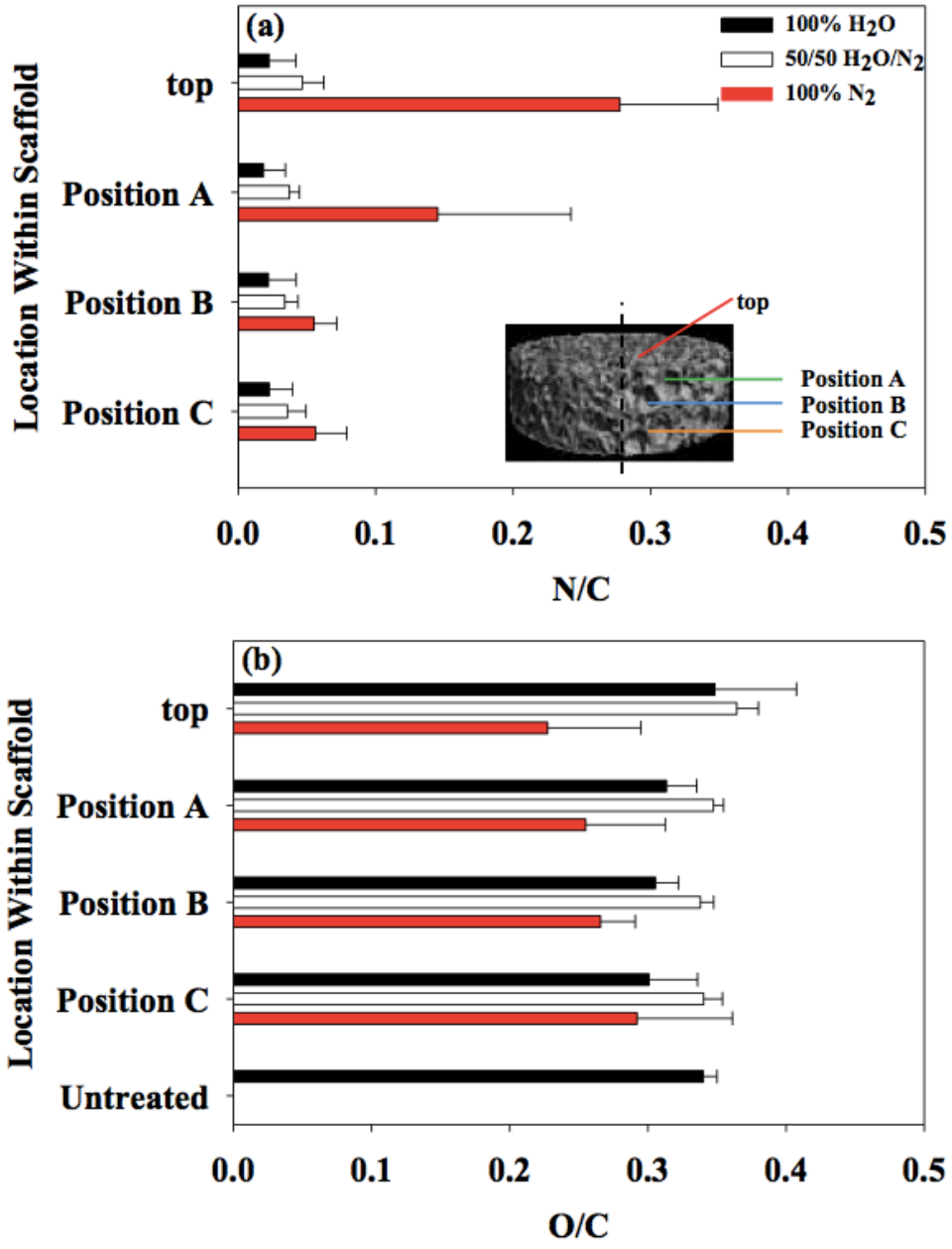


**Figure 7.5.** Cross sectional mapping for $N_2/H_2O$ treated scaffolds using XPS elemental compositional data to calculate O/C and N/C ratios. The inset shows the various positions analyzed in the analysis.

Furthermore, the largest N/C was observed on the tops of scaffolds treated in 100% $N_2$ plasmas, and the most oxidation was observed on the tops of scaffolds treated in 100% $H_2O$ and 50/50 $N_2/H_2O$ plasmas. Note that ~3% N is observed in scaffolds treated with 100% $H_2O$ plasmas. We attribute this to contamination from the reactor walls due to poor cleaning after treatments with 100% $N_2$. Preliminary experiments reveal that cleaning the reactor with 100% $H_2O$ for 1.5 h removes all contamination and does not introduce N into the scaffold. Ongoing experiments in the Bari laboratories aim to collect more data for statistical analysis for 100% $H_2O$ treated scaffolds.

Deconstruction of the $C_{1s}$ high-resolution XPS spectra, Fig. 7.6, reveals that the surface composition of plasma treated scaffolds is differs from that of native PCL. As is typical for untreated PCL,[4,6] four main binding environments are observed, Fig. 7.6a. Spectra for scaffolds treated in 100% $H_2O_{(g)}$ plasmas, Fig. 7.6b, show a slight increase in the C-OH/C-OR and O-C-O/C=O components over those observed for untreated scaffolds. The addition of $N_2$ to the plasma feed introduces nitrogen binding environment at 285.8 eV and an increase in the intensity of the binding environment at 288.0 eV, Fig. 7.6c-d. As has been previously documented, these binding energies in $C_{1s}$ spectra are not exclusively attributable to C-N moieties, but also can contain contributions from C-O species. Thus, it is difficult to elucidate the individual contributions; therefore, these are grouped together for clarity. We are forced to make a grouped assignment to these peaks, however $N_{1s}$ high-resolution XPS data, Figure 7.7, can provide more information about the nitrogen binding in the sample. Reports by Renò[18] and Fally[19] report that $N_{1s}$ energies for N-C and N-C=O are ~398.8 ± 0.2 eV and ~400.5 ± 0.5 eV, respectively. As Fig. 7.7 shows, the $N_{1s}$ signal for scaffolds treated in a 50/50 $N_2/H_2O$ plasma is centered around 400.0 eV and the signal for scaffolds treated in a 100% $N_2$ plasma is centered around 398.5 eV. This

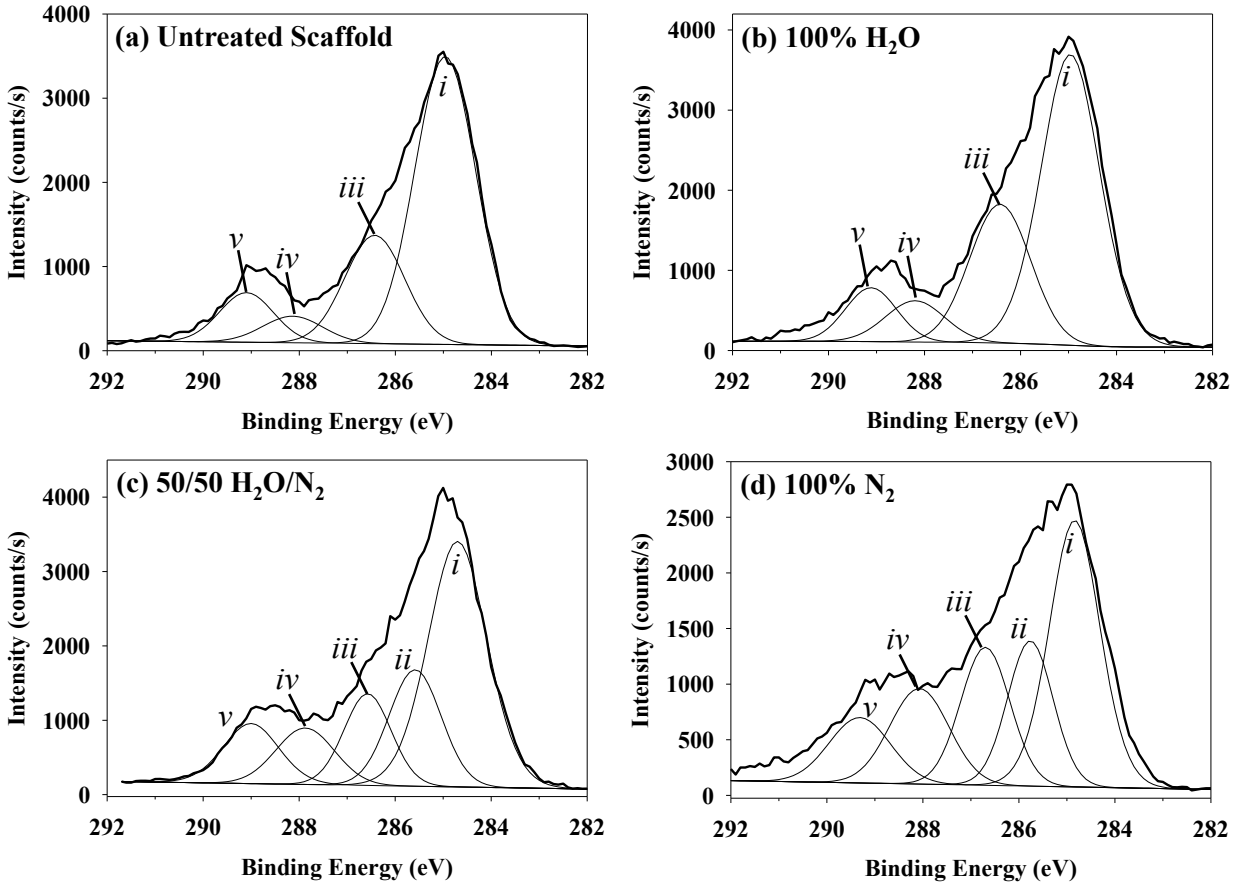


**Figure 7.6.** High resolution $C_{1s}$ XPS spectra scaffolds for (a) untreated scaffolds and freshly treated scaffolds modified in (b) 100% $H_2O$ plasmas, (c) 50/50 $N_2/H_2O$ plasmas, and (d) 100% $N_2$ plasmas. Labeled binding environments correspond to (*i*) C-C/C-H, (*ii*) C-N/C-COOH, (*iii*) C-OH/C-OR, , and (i*v*) N-C=O/C=O, (*v*) -O-C=O/-COOH

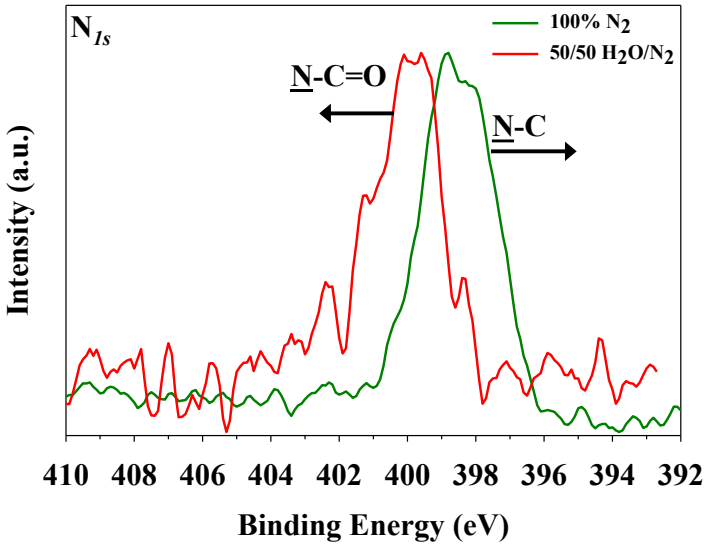


**Figure 7.7.** High-resolution $N_{1s}$ XPS data for scaffolds freshly treated in 100% $N_2$ and 50/50 $H_2O/N_2$ plasmas.

suggests that the majority of the nitrogen binding present on the 100% $N_2$ plasma treated scaffolds is more amine-like, and nitrogen that exists on the 50/50 $N_2/H_2O$ treated scaffolds is more amide-like. Note that an increase in amide functionality has been suggested[9] to be directly related to enhanced cell growth. Even though the nitrogen exists in very low concentrations, a surface concentration of nitrogen as low as 1-3% can increase cell growth on polymeric surfaces.[9,10]

The wettability of a polymeric surface is directly related to the functional groups present on the surface as observed in previous work by Steen and Fisher. They showed that the wettability of polysulfone, polyethersulfone, and polyethylene membranes can be increased upon treatment with $H_2O_{(g)}$ plasmas[20,21] and attributed the increased wettability to the incorporation of oxygen-containing functional groups implanted on the surface. Specifically, OH, CO, C=O, and O-C=O were introduced to the polymer surfaces upon $H_2O_{(g)}$ plasma treatment. Here, XPS data confirm an increase in the oxidation of scaffolds upon treatment with $H_2O_{(g)}$-containing plasmas. Figure 7.8 expands upon this by plotting the $C_{1s}$ binding environments relative to the hydrocarbon environment as a function of $H_2O_{(g)}$ in the gas feed. The C-COOH/C-N binding environment at ~285.5 eV (labeled as *ii* in Fig. 7.6) was omitted from the calculation because it does not appear in the untreated sample. General trends indicate an overall increase in the functional groups present relative to the hydrocarbon backbone of the polymeric surface. Specifically, the O-C=O/C-OOH environment increases dramatically with all plasma treatments. Thus, these treatments can increase the overall wettability of the scaffolds by implanting more polar (O and N) functional groups onto the surface relative to untreated scaffolds. Furthermore, we attribute the greater absorption properties of scaffolds treated in 100% $H_2O_{(g)}$-containing

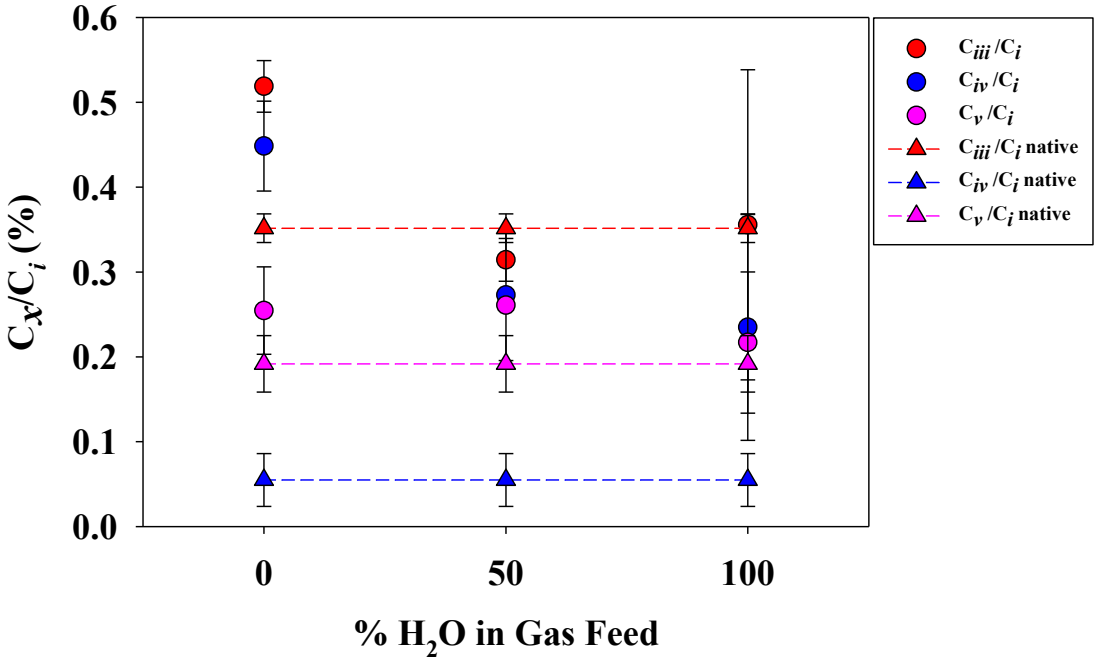


**Figure 7.8.** $C_{1s}$ binding environments relative to the C-C/C-H binding environment as a function of $H_2O$ in the gas feed.

plasmas over those treated in 100% $N_2$ plasmas to the greater polarity of the O atoms present on that surface.

Saos-2 osteoblast cells ($5.0 \times 10^4$ cells/scaffold) were seeded on untreated and plasma treated scaffolds and allowed to incubate for 18, 42, and 114 h, and two metrics were used to evaluate the efficacy of plasma treatment on the cells' growth and proliferation. The cells' metabolic activity was examined with the MTT colorimetric assay and the clustering and morphological characteristics of the cells were measured with fluorescence microscopy. Metabolic activity data, Fig. 7.9, are presented as mean optical densities (O.D.), where an increase in O.D. is directly related to an increase in cell viability. For all incubation times, cell metabolic activity is observed for all samples. Metabolic activity observed 18 h after cell seeding is similar to that of untreated scaffolds, within experimental error. After 48 h, cells seeded on scaffolds treated in 50/50 $H_2O/N_2$ and 100% $N_2$ plasmas displayed higher metabolic activity than untreated scaffolds. After 114 h of incubation, all plasma treated scaffolds, regardless of gas feed composition, showed enhanced cell growth over that of untreated scaffolds.

The clustering characteristics and cell morphology were evaluated with fluorescence microscopy, Figure 7.10. Cells on untreated PCL scaffolds exhibit rounded morphology and are not clustered, Fig. 7.10a (seen as small, bright green dots). In contrast, cells on plasma treated scaffolds are clustered together and much larger. Specifically, these cells appear web-like and spread over the scaffold surface, Fig. 7.10b-d. The spreading morphology is indicative of healthy cells in an active state of adhesion,[15] as it affects cell division and the synthesis of DNA and proteins.[22] Furthermore, the low spreading characteristic observed for cells seeded on

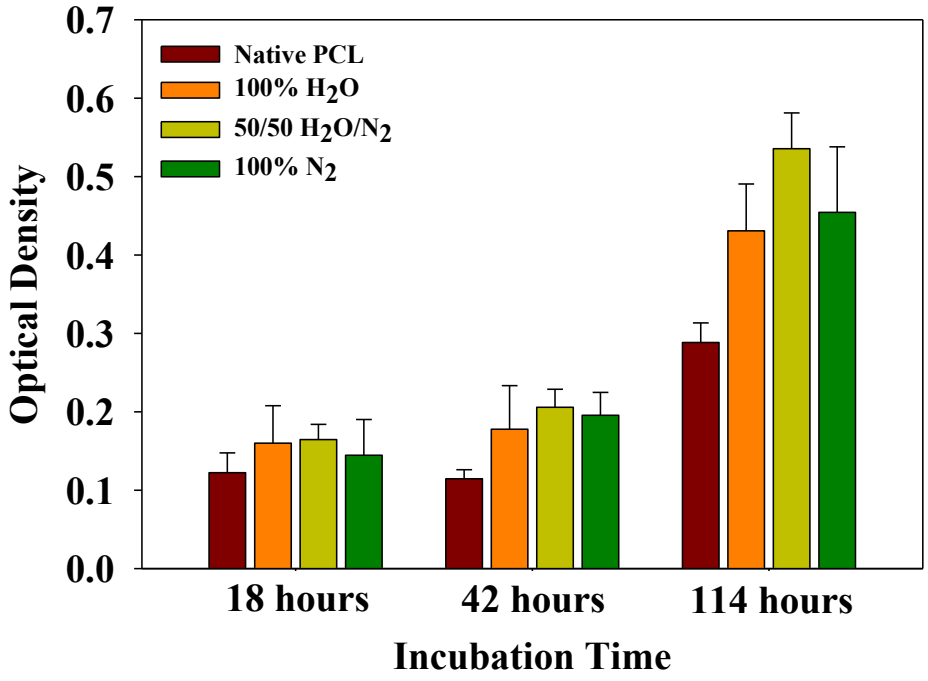


**Figure 7.9.** Optical density as a function of incubation time acquired from the MTT colorimetric assay for untreated scaffolds and scaffolds treated in $H_2O/N_2$ plasmas.

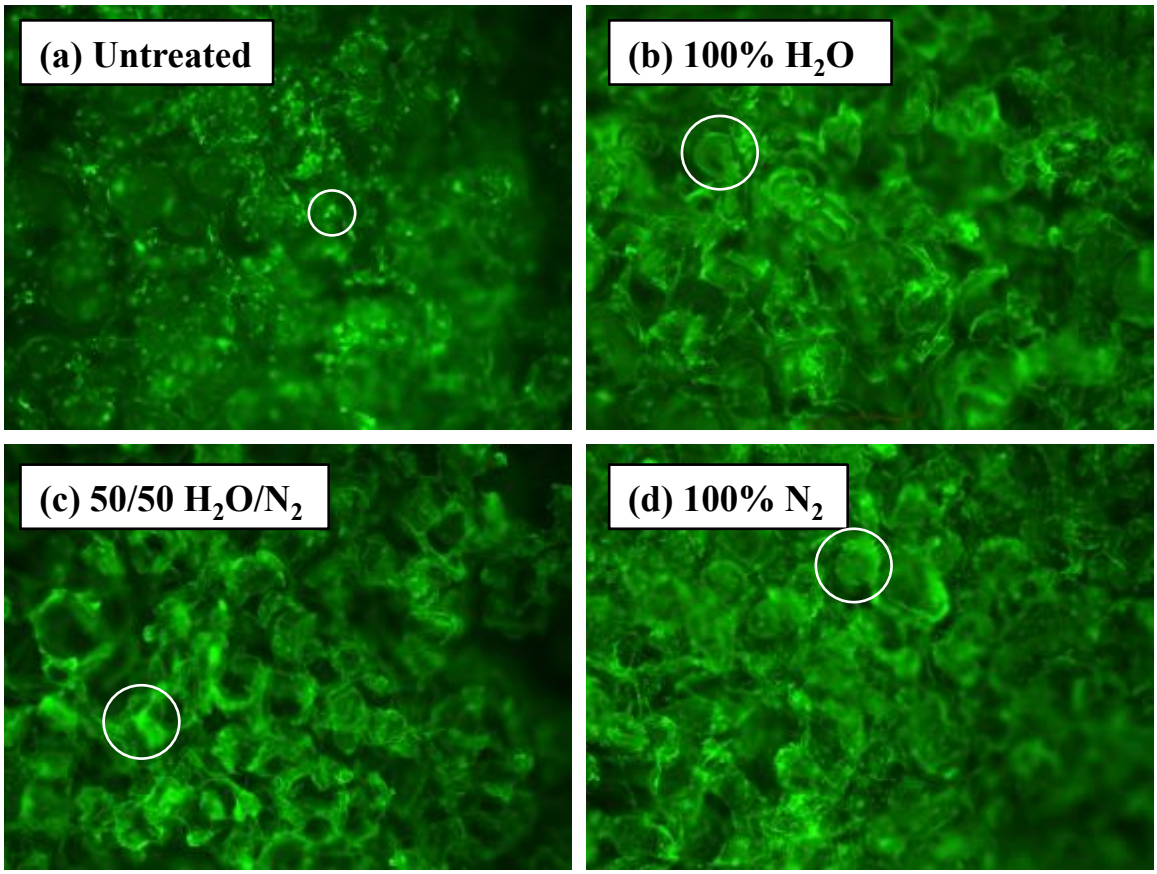


**Figure 7.10.** Fluorescence microscopy images of Soas-2 cells growing on untreated and plasma treated PCL scaffolds. For reference, circles surround bright green cells, where the darker green and black areas are part of the background.

untreated scaffolds can indicate weak cell adhesion.[23] Lastly, it should be noted that the images in 7.10 are representative for all incubation times.

As mentioned in Section 7.1, ongoing research in many groups focuses on factors affecting cell growth on polymeric surfaces.[9] Hypotheses suggest that a surface's chemical composition,[10-12] roughness, [8,13,14], and wettability[3,9,18,23] can all contribute to cell-surface interactions. Indeed, Jacobs et al. presents a comprehensive overview of cell-surface interactions that suggests each combination of plasma treatment, surface type, surface functionality, and cell type could be studied as an independent system due to the wide range of observations found in the literature.[9] However, it is generally accepted that more wettable, N containing surfaces promote cell adhesion and growth to some degree.

In the study presented in this chapter, we focused on functionalizing the surface with N- and O-containing functional groups while creating a scaffold capable of absorbing water. Our results indicate an increase in -COOR, -COR, amine and amide functionality on the surface of PCL scaffolds not only add the polar groups necessary for increasing wettability, but also enhance Saos2 osteoblast cell growth. As mentioned in Section 7.1, the N-containing groups distributed throughout the scaffold network can interact with the cell membrane and promote adhesion and growth.[11] Furthermore, the increase in wettability can contribute to better attachment of cell binding proteins. [9,11] Clearly, the combination of N implantation and increased wettability from $H_2O$ and $N_2$ plasma modification systems allow for enhanced Soas2 cell growth on PCL scaffolds.

## 7.3 Summary

Plasma modification was shown to have a significant impact on the wettability, surface functionality, and cell growth capabilities of PCL scaffolds. Upon plasma treatment, the naturally hydrophobic scaffolds were immediately hydrophilic, and allowed water absorption for the entirety of a one-week aging period. Different chemical functionalities were grafted on the surface of the scaffolds, with a 50/50 mixture of $N_2$ and $H_2O$ vapor implanting the most uniform amount of nitrogen throughout the scaffold. Biological tests showed that Saos-2 osteoblasts exhibit enhanced cell growth on all plasma treated scaffolds with respect to untreated scaffolds. Furthermore, the scaffolds treated in a 50/50 mixture of $N_2$ and $H_2O$ vapor showed the most cell growth of all plasma treated scaffolds.

REFERENCES


[1] D. W. Hutmacher, Biomaterials **21**, 2529 (2000).
[2] Y. Deng, K. Zhao, X.-F. Zhang, P. Hu, and G.-Q. Chen, Biomaterials **23**, 4049 (2002).
[3] G. Chen, T. Ushida, and T. Tateishi, Macromol. Biosci. **2**, 67 (2002).
[4] F. Intranuovo, E. Sardella, R. Gristina, M. Nardulli, L. White, D. Howard, K. M. Shakesheff, M. R. Alexander, and P. Favia, Surface & Coatings Technology **205**, S548 (2011).
[5] F. Intranuovo, D. Howard, L. J. White, R. K. Johal, A. M. Ghaemmaghami, Pietro Favia, S. M. Howdle, K. M. Shakesheff, and M. R. Alexander, Acta Biomaterialia **7**, 3336 (2011).
[6] C. Yen, H. He, Z. Fei, X. Zhang, L. J. Lee, and W. S. W. Ho, International Journal of Polymeric Materials **59**, 923 (2010).
[7] M. T. Khorasani, H. Mirzadeh, and S. Irani, J. Appl. Polym. Sci. **112**, 3429 (2009).
[8] N. Hasirci, T. Endogan, E. Vardar, A. Kiziltay, and V. Hasirci, Surf. Interface Anal. **42**, 486 (2010).
[9] T. Jacobs, R. Morent, N. Geyter, P. Dubruel, and C. Leys, Plasma Chem Plasma Process **32**, 1039 (2012).
[10] H. Park, J. W. Lee, K. E. Park, W. H. Park, and K. Y. Lee, Colloids and Surfaces B: Biointerfaces **77**, 90 (2010).
[11] C. F. Chu, A. Lu, M. Liszkowski, and R. Sipehia, Biochim. Biophys. Acta **1472**, 479 (1999).
[12] L. Garrido, I. Jiménez, G. Ellis, P. Cano, J. M. García-Martínez, L. López, and E. de la Peña, J. Appl. Polym. Sci. **119**, 3286 (2010).
[13] Y. Wan, X. Qu, J. Lu, C. Zhu, L. Wan, J. Yang, J. Bei, and S. Wang, Biomaterials **25**, 4777 (2004).
[14] E. D. Yildirim, H. Ayan, V. N. Vasilets, A. Fridman, S. Güçeri, and W. Sun, Plasma Processes Polym. **5**, 58 (2008).
[15] M. T. Khorasani, H. Mirzadeh, and S. Irani, Radiation Physics and Chemistry **77**, 280 (2008).
[16] J. Yang, J. Bei, and S. Wang, Polym. Adv. Technol. **13**, 220 (2002).
[17] J. J. A. Barry, M. M. C. G. Silva, K. M. Shakesheff, S. M. Howdle, and M. R. Alexander, Adv. Funct. Mater. **15**, 1134 (2005).
[18] F. Renò, D. D'Angelo, G. Gottardi, M. Rizzi, D. Aragno, G. Piacenza, F. Cartasegna, M. Biasizzo, F. Trotta, and M. Cannas, Plasma Processes Polym. **9**, 491 (2012).
[19] F. Fally, C. Doneux, J. Riga, and J. J. Verbist, J. Appl. Polym. Sci. **56**, 597 (1995).
[20] M. L. Steen, A. C. Jordan, and E. R. Fisher, Journal of Membrane Science **204**, 341 (2002).
[21] M. L. Steen, L. Hymas, E. D. Havey, N. E. Capps, D. G. Castner, and E. R. Fisher, Journal of Membrane Science **188**, 97 (2001).
[22] K. S. Siow, L. Britcher, S. Kumar, and H. J. Griesser, Plasma Processes Polym. **3**, 392 (2006).
[23] R. Di Mundo, M. Nardulli, A. Milella, P. Favia, R. d'Agostino, and R. Gristina, Langmuir **27**, 4914 (2011).

# CHAPTER 8

# FUNCTIONALIZATION OF POLYMERIC SCAFFOLDS USING $NH_3/H_2O$ PLASMA MODIFICATION AND ALLYL ALCOHOL/ALLYL AMINE PLASMA COPOLYMERIZATION

This chapter extends the work presented in Chapter 7 as it translates work done at the University of Bari to the Fisher labs at Colorado State University. This chapter describes both plasma surface modification and plasma deposition systems to achieve N- and O-containing functional group implantation throughout the scaffolds. At the time of this writing, this work is being prepared for submission to *Surface Coatings and Technology.*

## 8.1 Introduction

As discussed in Chapter 7, there is an increased interest in plasma modifying polymeric scaffold materials for the purpose of enhancing cell growth. While Chapter 7 discussed plasma modification of PCL scaffolds, there is a strong desire to also use plasma deposition methods to functionalize polymeric scaffolds to increase the tunability of cell behavior.[1-5] In one of the first reported studies of plasma deposits on polymeric scaffolds, Barry et al. investigated 3T3 fibroblast growth on poly($_{DL}$-lactic acid) (PLA) scaffolds after plasma grafting and plasma deposition of allylNH.[4] Their main focus was achieving N incorporation throughout the 3D scaffold network in an effort to promote cell growth. Their plasma deposition scheme coated the scaffolds with a maximum of 13.7% N whereas the plasma grafting methods created surfaces with 2.2% N. Furthermore, they determined that the plasma grafting methods were less successful at functionalizing the interior of the scaffold than plasma deposition of allylNH,

which they attributed to improved diffusion of species during plasma deposition. The scaffolds treated under allylNH plasma deposition conditions promoted the 3T3 fibroblast activity and attachment over that of the scaffolds treated under plasma grafting conditions. However, the authors still observed increased cell activity for grafted scaffolds over that of native PLA.

Barry et al. later extended their work in this area by designing plasma treatments that allowed cells to homogeneously grow throughout the scaffold network.[3] They first treated the scaffolds in a depositing allylNH plasma system. Then, the scaffolds were treated in a hexane plasma such that *pp*-hexane was only deposited on the edge region of the scaffold. This gradient of non-cell-adhesive *pp*-hexane to cell-adhesive *pp*-allylNH allowed for a radial, homogeneous distribution of 3T3 fibroblasts throughout the scaffold network.

Intranuovo and coworkers used similar allylNH/hexane plasma systems to improve the penetration of N into the scaffold core.[2] They were able to increase the uniformity of the distribution of 3T3 fibroblasts through the scaffold network over that of Barry et al. This method of scaffold modification effectively created a chemical concentration gradient, which allowed for more uniform cell penetration within the scaffold network. They extended this work by copolymerizing ethylene and $N_2$ onto PCL scaffolds as an alternate method for implanting the N functionality necessary for cell growth.[1] The work showed that although there was a decrease in N functionality within the interior of the scaffold, Saos2 osteoblast proliferation was still enhanced over untreated scaffolds. These studies by Intranuovo and by Barry, along with the studies presented in Chapter 7, forms the basis of the work presented here.

As this dissertation has referenced on several occasions, N incorporation is key for achieving enhanced cell growth and proliferation within a scaffold's 3D network.[3-5] Furthermore, as mentioned in the preceding chapter, oxygen incorporation onto PCL scaffolds

can enhance the wettability and add additional functionalities to the scaffold surface, both of which can aid in enhancing cell growth. Previous experiments in our laboratory and others have shown that $NH_3$ and $H_2O$ plasmas can implant amine, alcohol, and carboxyl functionality onto polymeric surfaces, as well as increase surface wettability.[1,4,6-9] Chapter 6 showed that the copolymerization of allylOH and allylNH can simultaneously impart amine, alcohol and carboxylic acid functionality onto surfaces. With this in mind, experiments described herein were designed to explore the use of $NH_3/H_2O$ plasma modification systems and allylNH/allylOH plasma deposition systems to simultaneously implant nitrogen and increase the hydrophilicity of PCL scaffolds. To ensure the viability of the surface modification processes for a range of application, scaffold aging after treatment is also monitored using WCA measurements.

## 8.2 Results and Discussion

PCL scaffolds were treated in both plasma modification ($NH_3/H_2O$, 30 W, 250 mTorr, 6.5 min) and plasma deposition (allylOH/allylNH, 50 W, 5% d.c., 100 mTorr, 15 min) regimes. The rotating drum plasma reactor described in Chapter 5 was used for all plasma treatments to ensure a more uniform plasma treatment. Scaffolds used for XPS and WCA measurements were 10 x 3 mm and 20 x 3 mm, respectively.

### 8.2.1 Surface modification with $NH_3/H_2O$

Table 8.1 lists the elemental composition of the external surface and cross sections for untreated and plasma modified PCL scaffolds. Regardless of location in the scaffold network, all samples contain a significant amount of oxygen, as expected from the composition of native PCL. Notably, for a given gas feed composition, the oxygen content of the surface does not change appreciably between external and internal surfaces of the scaffolds, suggesting equivalent treatment throughout the scaffold network. As expected, the nitrogen content of the scaffold

surfaces increase with increasing $NH_3$ in the gas feed. Although this trend holds for both the external surface (top) and the cross section of the scaffolds, the nitrogen content in the cross section is ~4% lower than that found on the external surface. Note that when the scaffolds are cut to allow sampling of the cross section, untreated surfaces are exposed and thus included in the XPS measurements. Thus, much of the discrepancy in nitrogen content between the top and the cross section can be attributed to the inclusion of untreated PCL surfaces in the measurement of the cross section.

The elemental composition of scaffold tops and cross-sections was monitored for 3 weeks after plasma treatment to evaluate how the scaffolds aged, Table 8.1. For a given plasma modification system, minimal oxidation of the scaffold occurs over the 3 week aging period. The scaffolds do tend, however, to lose more nitrogen in the cross section than on the external surface upon aging. Specifically, measurements of both the tops and cross sections of scaffolds treated in a 100% $NH_3$ plasma indicate more than 50% loss of nitrogen during the aging process.

Figure 8.1 extends the Table 8.1 data by plotting O/C and N/C ratios as a function of $NH_3$ content in the gas feed for the tops of plasma-treated scaffolds. For gas feed compositions of 0-75% $NH_3$, the O/C ratio of the surface linearly decreases ($R^2$=0.99) as a function of increasing $NH_3$ in the gas feed before leveling off. Thus, the surface modified with 100% $NH_3$ do not have statistically different O/C ratios than surfaces modified in gas feeds of 75% $NH_3$. This trend continues for 24 hours after deposition ($R^2$=0.97). However, after an aging period of 3 weeks, the O/C ratio all modified surfaces, independent of gas feed, is the same within statistical error. The N/C ratio for surfaces modified in gas feeds of 0-50% $NH_3$ linearly increase ($R^2$=0.99) with increasing $NH_3$ content. The same strong linear correlation for these gas feeds holds throughout the entire 3-week aging period. The external surface of scaffolds modified in 75% and 100%

**Table 8.1. XPS Elemental Composition of scaffolds treated in $NH_3/H_2O$ plasmas[a]**

| Sample Position and Age | $NH_3$ in Feed (%)[b] | C (%) | O (%) | N (%) | O/C | N/C |
|---|---|---|---|---|---|---|
| Top Fresh | Untreated | 74.6 ± 0.7 | 25.4 ± 0.7 | 0 | 0.34 ± 0.01 | 0 |
| | 100 | 69.0 ± 0.2 | 20.0 ± 0.4 | 10.4 ± 1.2 | 0.29 ± 0.01 | 0.15 ± 0.02 |
| | 75 | 70.7 ± 1.2 | 19.7 ± 1.7 | 9.4 ± 0.3 | 0.28 ± 0.01 | 0.13 ± 0.01 |
| | 50 | 65.0 ± 2.6 | 25.3 ± 1.3 | 9.4 ± 2.4 | 0.39 ± 0.03 | 0.15 ± 0.04 |
| | 25 | 70.1 ± 1.5 | 24.0 ± 1.8 | 5.7 ± 1.2 | 0.34 ± 0.03 | 0.08 ± 0.02 |
| | 0 | 68.9 ± 2.1 | 30.9 ± 1.9 | 0 | 0.45 ± 0.04 | 0 |
| Cross Section Fresh | Untreated | 75.4 ± 0.9 | 24.6 ± 0.9 | 0 | 0.33 ± 0.02 | 0 |
| | 100 | 75.0 ± 0.7 | 18.7 ± 1.3 | 6.3 ± 0.7 | 0.25 ± 0.02 | 0.08 ± 0.01 |
| | 75 | 75.4 ± 0.7 | 21.6 ± 1.8 | 3.0 ± 1.1 | 0.29 ± 0.03 | 0.04 ± 0.01 |
| | 50 | 74.3 ± 0.2 | 23.8 ± 1.5 | 1.9 ± 0.5 | 0.32 ± 0.03 | 0.03 ± 0.01 |
| | 25 | 69.8 ± 1.8 | 27.0 ± 1.0 | 3.1 ± 1.0 | 0.39 ± 0.02 | 0.04 ± 0.02 |
| | 0 | 69.7 ± 0.4 | 30.3 ± 0.4 | 0 | 0.44 ± 0.01 | 0 |
| Top Aged 3 Weeks | 100 | 70.9 ± 1.1 | 21.8 ± 1.5 | 7.0 ± 0.8 | 0.31 ± 0.03 | 0.10 ± 0.01 |
| | 75 | 67.1 ± 5.4 | 23.6 ± 4.4 | 9.1 ± 1.5 | 0.31 ± 0.03 | 0.14 ± 0.03 |
| | 50 | 71.6 ± 5.6 | 24.1 ± 4.2 | 4.2 ± 1.3 | 0.34 ± 0.09 | 0.06 ± 0.02 |
| | 25 | 68.1 ± 0.8 | 25.2 ± 0.5 | 6.8 ± 1.3 | 0.37 ± 0.003 | 0.10 ± 0.02 |
| | 0 | 69.9 ± 3.7 | 29.8 ± 3.2 | 0 | 0.42 ± 0.07 | 0 |
| Cross Section Aged 3 Weeks | 100 | 74.1 ± 4.2 | 23.4 ± 2.9 | 2.5 ± 1.7 | 0.31 ± 0.06 | 0.03 ± 0.02 |
| | 75 | 72.6 ± 2.7 | 24.1 ± 3.9 | 3.3 ± 1.3 | 0.33 ± 0.06 | 0.04 ± 0.02 |
| | 50 | 71.7 ± 1.7 | 26.1 ± 1.7 | 2.2 ± 0.3 | 0.36 ± 0.03 | 0.03 ± 0.004 |
| | 25 | 72.2 ± 4.7 | 27.2 ± 4.2 | 0.7 ± 0.5 | 0.37 ± 0.09 | 0.03 ± 0.008 |
| | 0 | 71.9 ± 3.2 | 28.1 ± 3.1 | 0 | 0.39 ± 0.06 | 0 |

[a]Scaffolds were treated in $NH_3/H_2O$ plasmas with $P$ = 30 W, total pressure of 250 mTorr and treatment time of 6.5 min
[b]Remainder of feed gas composition was $H_2O$.

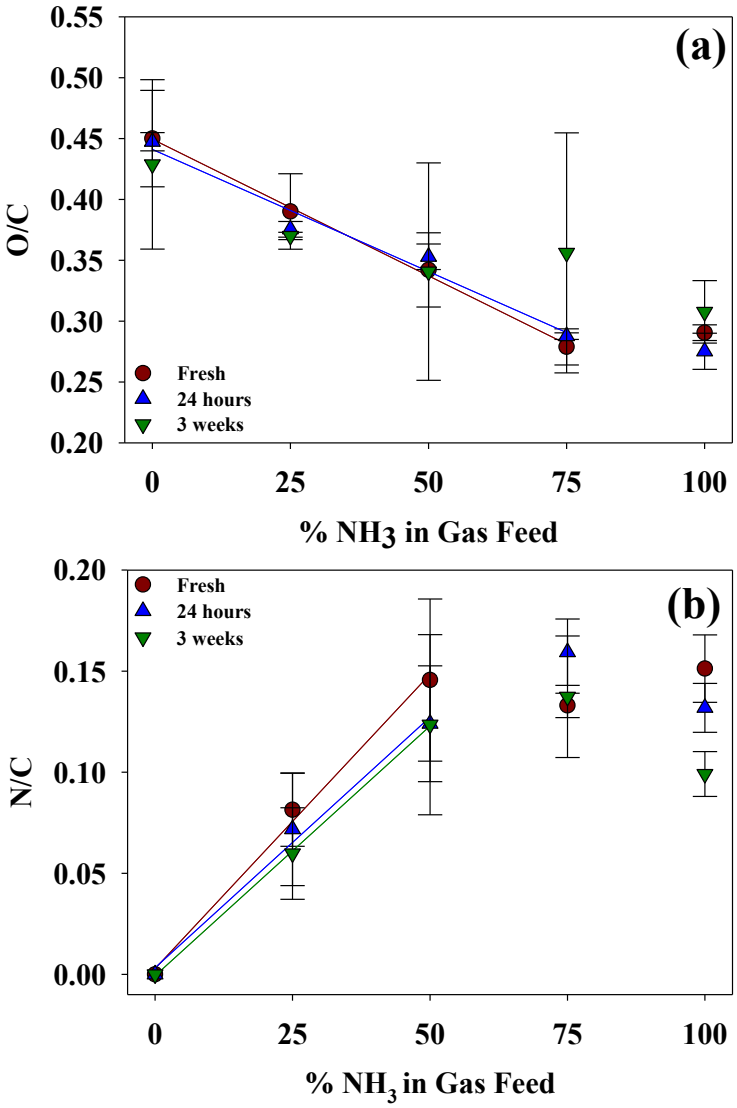


**Figure 8.1.** O/C and N/C ratios of the tops of scaffolds treated in $NH_3/H_2O$ plasmas (30 W, 250 mTorr) as a function of gas feed composition. The lines represent best fitting for the linear portions of the data.

$NH_3$ plasmas have the same N/C ratio as those modified in 50% $NH_3$ plasmas within experimental error. This suggests that, in these systems, there is a maximum N/C concentration that can be achieved on the external surface of the scaffold. Furthermore, , unlike the O/C ratio, the N/C ratios of the scaffold surface does not change upon aging. Additionally, the linearity of the N/C ratio allows for better predicting of surface composition when tailoring the plasma treatments for specific applications.

The O/C and N/C content for the scaffold cross-sections are shown in Figure 8.2. Across the range of all gas feed compositions, the O/C ratio linearly decreases ($R^2$=0.99) as a function of increasing $NH_3$ content in the gas feed. The O/C ratio of the internal surface of the scaffold does not appreciably change as the scaffolds age. The N/C ratio linearly increases ($R^2$=0.99) as a function of $NH_3$ content in gas feeds composed of 0-50% $NH_3$ for freshly treated scaffolds and scaffolds aged throughout the 3 week aging period. Upon aging, the N/C ratio in the cross section of the scaffolds is similar for those modified in plasmas that contain ≥ 50% $NH_3$, within statistical error. However, N incorporation, which was discussed earlier as a method for enhancing cell growth, is still present within the network after 3 weeks, which is important when considering the cell-growth potential of these materials as related to shelf life.

High-resolution XPS data were collected to better understand the functional groups in which C and N exist. For reference, a high resolution $C_{1s}$ XPS spectrum for an untreated PCL scaffold is shown in Figure 7.6a. Briefly, the observed binding environments for untreated PCL are (*i*) C-C/C-H at 285.0 eV, (ii) C-OH/C-OR at 286.5 eV, (iii) C=O/O-C-O at 288.0 eV, and (*iv*) -O-C=O/-COOH at 289.1 eV.[1,10-13] Figure 8.3a-c contains high-resolution $C_{1s}$ XPS spectra of scaffolds freshly modified with plasmas containing different mixtures of $NH_3/H_2O$. With the 100% $H_2O$ plasma treatment, Fig 8.3a, the scaffolds exhibit an increase in the carbonyl binding

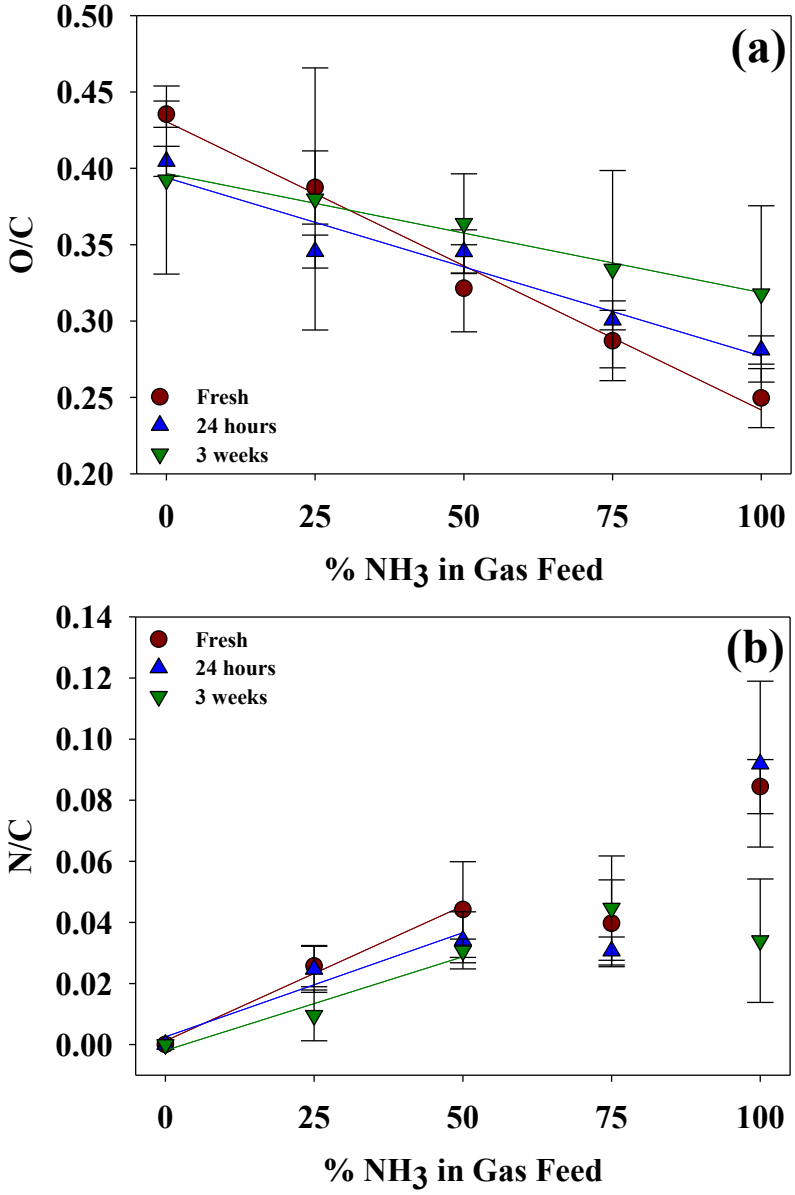


**Figure 8.2.** O/C and N/C ratios of the cross sections of scaffolds treated in $NH_3/H_2O$ plasmas (30 W, 250 mTorr) as a function of gas feed composition. The lines of best fit for the linear portion of the data are shown.

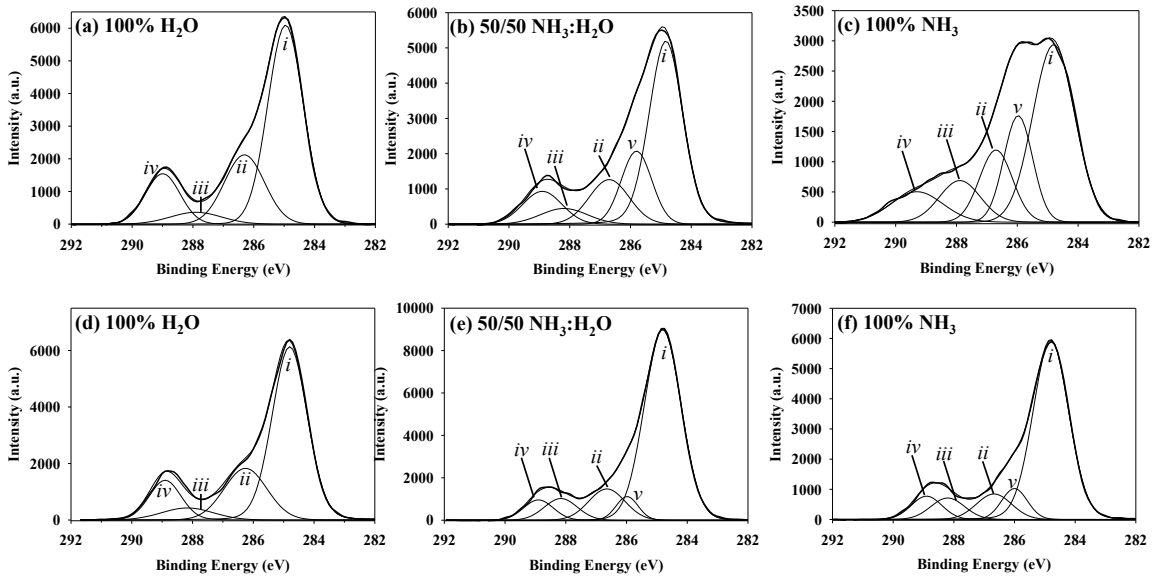


**Figure 8.3** High resolution $C_{1s}$ XPS spectra for freshly treated (a-c) PCL scaffolds and then aged 3 weeks (d-f) after plasma modification using (a,d) 100% $H_2O$, (b,c) 50/50 mixtures of $NH_3$ and $H_2O$, and (c,f) 100% $NH_3$ plasmas (30 W, 250 mTorr). The binding environments correspond to (*i*) C-C/C-H, (*ii*) C-OH/C-OR, (*iii*) C=O/N-C=O, (*iv*) O-C=O/ COOH, and (*v*) N-C/C-COOH

environment, as well as an increase in the alcohol/ether environment, relative to the untreated material. A fifth binding environment, (*v*) N-C/C=O, appears in the spectrum at 286.0 eV for scaffolds treated in 100% $NH_3$ plasmas, Fig. 8.3c. Furthermore, the increase in the binding environment at 288.0 eV in this spectrum can be attributed to contributions from N-C=O binding. These two binding environments are typical for nitridation of PCL reported in the literature.[1,2,11,13,14] Spectra for scaffolds treated in mixed-gas systems exhibit a mixture of binding environments present on scaffolds treated using single-gas systems. For example, XPS spectra for scaffolds treated in a 50:50 $NH_3/H_2O$ plasma, Fig. 8.2b, contain C-C/C-H, C-OH, COOH and C=O binding as seen in spectra of 100% $H_2O$ plasma treated scaffolds, and N-C and N-C=O binding as seen in spectra of 100% $NH_3$ plasma treated scaffolds.

High-resolution $C_{1s}$ spectra for plasma treated scaffolds aged for 3 weeks are shown in Figure 8.3c-d. The most notable change from freshly modified scaffolds is the substantial reduction of the N-C/C-COOH peak ~ 285.6 eV in the spectra for materials treated in $NH_3$-containing plasmas. This supports the observation that N loss occurs throughout the aging period, Table 8.1. Furthermore, the functional groups present on scaffolds treated in 100% $H_2O$ plasmas do not substantially change over time, indicating that these plasma treatments are relatively permanent. High-resolution $N_{1s}$ XPS spectra for the tops of scaffolds treated in 50% and 100% $NH_3$ plasmas are shown in Figure 8.4 to explore how the nitrogen is bound immediately after plasma processing and during the aging process. Two notable peaks are present after deconstruction of the raw data, N-C at ~398.8 ± 0.2 eV and N-C-O at ~400.5 ± 0.5 eV, as described by Fally.[15] Freshly treated scaffolds treated in both 100% $NH_3$ (Fig. 8.4a) and 50% $NH_3$ (Fig. 8.4c) plasmas both contain ~65% N-C and ~35% N-C-O binding. Upon aging, the N-C-O binding environment for scaffolds treated in 100% $NH_3$ plasmas (Fig. 8.4b)

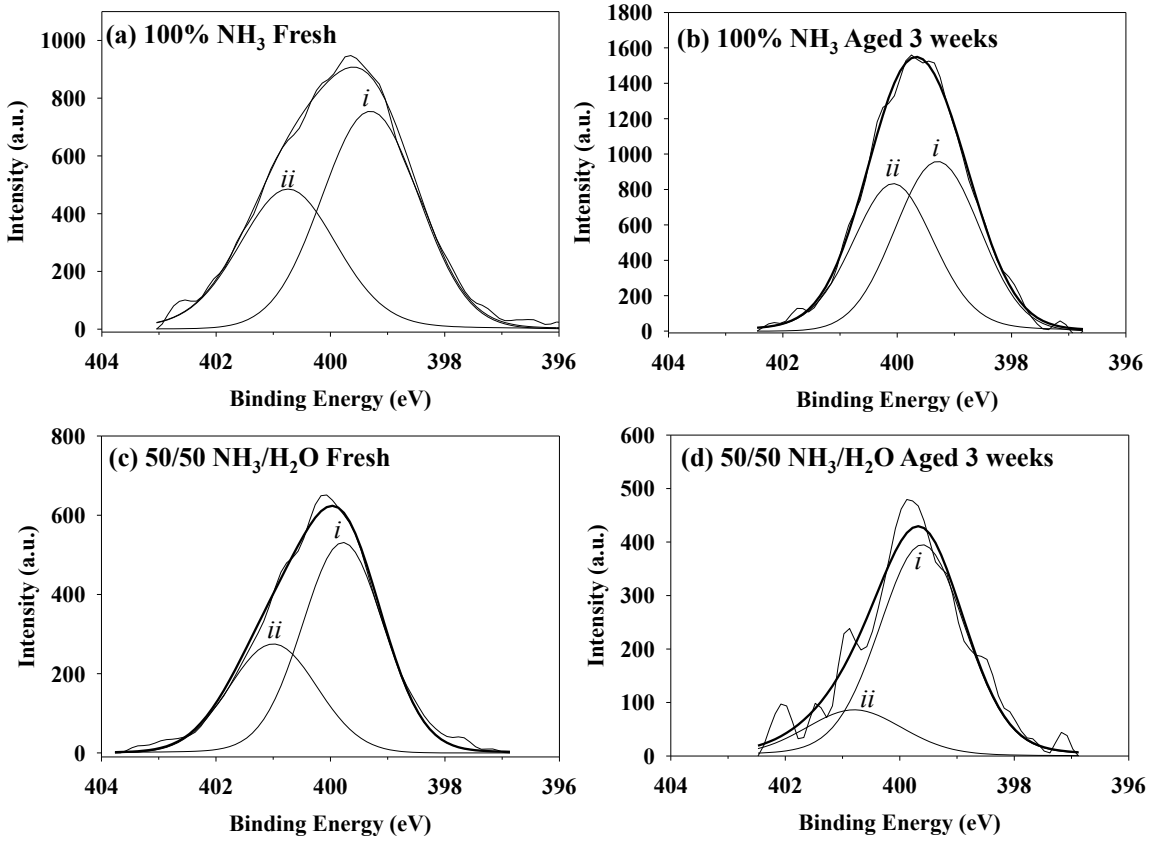


**Figure 8.4.** High-resolution $N_{1s}$ XPS data for scaffolds (a) freshly treated in 100% $NH_3$ and then (b) aged 3 weeks; (c) freshly treated in 50/50% $NH_3/H_2O$ plasmas and then (d) aged 3 weeks. Binding environments correspond to (*i*) N-C and (*ii*) N-C-O functionality.

marginally increases to ~40%. The minimal change in N-C-O binding suggests that the majority of the oxidation due to aging occurs within the polymer network and not the implanted N functional groups, as indicated in the substantial changes of C-O binding presented in Fig. 8.3.

The water absorption properties were measured as a function of gas feed during plasma processing using contact angle goniometry methods similar to those described in Chapter 7. A 4 $\mu$L water drop was dispensed on the top of the scaffold, and the average absorption rate was measured as a function of time. Upon plasma treatment, water droplets placed on the scaffold surface experienced immediate absorption. The instantaneous nature of the water drop absorbing is evident by the large error bars associated with the fresh time points as very few data points could be analyzed. For example, at a collection rate of 211 frames-per-second (fps), only 4-5 data points were available for analysis, thereby introducing a much larger error to the measurement than is true for analysis of data with dozens of data points. The immediate absorption upon plasma treatment nonetheless verifies that $NH_3/H_2O$ vapor plasma modifications increase the absorption properties from the untreated, hydrophobic scaffolds. Note that these high absorption rates were also observed for the scaffolds treated in $N_2/H_2O$ plasmas described in Chapter 7.

The rate of absorption on scaffolds treated in $NH_3/H_2O$ plasmas is shown in Figure 8.5 as a function of $NH_3$ content in the plasma gas feed. Freshly treated scaffolds had an average initial absorption rate of ~200 $\mu$L/s and did not appreciably change with plasma gas composition. For comparison, untreated PCL scaffolds do not absorb water and have water contact angles of ~120°, as described in detail in Chapter 7. After aging the scaffolds for 24 h, the water absorption rate decreases considerably, regardless of plasma feed gas composition. A further decrease in water absorption rate is observed after 96 hours of aging. Typically, the absorption

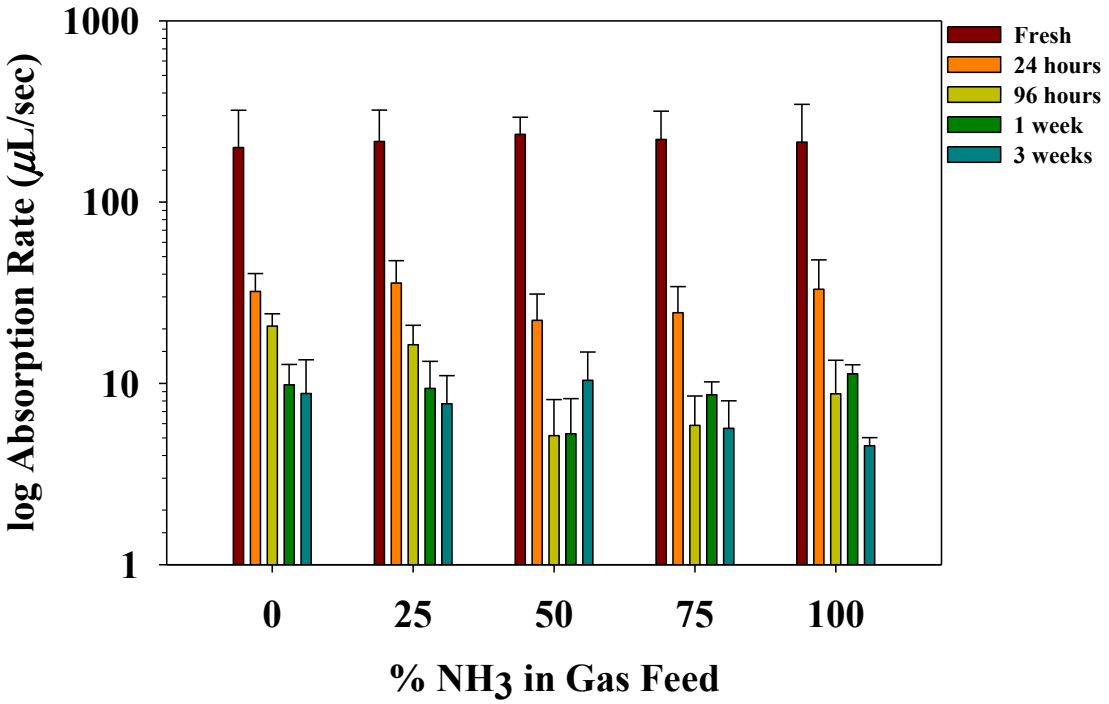


**Figure 8.5.** Initial water absorption rate as a function of $NH_3$ in the gas feed. Data for freshly treated and aged scaffolds are shown.

rate stabilized after the first 96 hours, and after 3weeks of aging, all aged scaffolds had absorption rates of < 15 $\mu$L/s. Importantly, all scaffolds still absorbed water throughout the entirety of the aging period.

The initial water absorption rates of the scaffolds did not appreciably vary between plasma feed compositions, leading us to theorize there may be other contributions besides surface chemistry affecting the water absorbing properties of the scaffolds. To better gauge if these plasma treatments affected the porous structure of the scaffolds, scanning electron microscopy was used to observe the scaffold's porous network. Figure 8.6 shows images of the top and cross section for scaffolds modified in a 100% $H_2O$ plasma. The images are representative of all scaffolds modified in $NH_3/H_2O$ plasma systems. For reference, SEM images of untreated scaffolds are shown in Fig. 7.4a-b. There are no appreciable changes to the porous network upon plasma treatment, which is ideal for applications wherein cell growth relies on the 3D porous structure of the scaffold. Although the structure of the scaffolds was retained upon plasma treatment, changes in nanoscale roughness or the surface hardness could have occurred and is an area for further exploration. Several authors have shown that changes in roughness and hardness of a surface can have dramatic effects on a polymer's wettability,[10,12,16,17] and thus could affect the absorption properties of the scaffolds.

### 8.2.2 Plasma deposition with allylOH/allyNH

PCL scaffolds were also treated in an allylOH/allylNH plasma deposition system to compare and contrast the effect of different plasma processes on the ability to implant functional groups within the scaffold network. Table 8.2 lists the XPS atomic compositions for scaffolds treated in allylOH/allylNH plasmas. As expected, as the allylNH content of the plasma gas feed increases, oxygen content of the scaffold surface decreases and the nitrogen content increases.

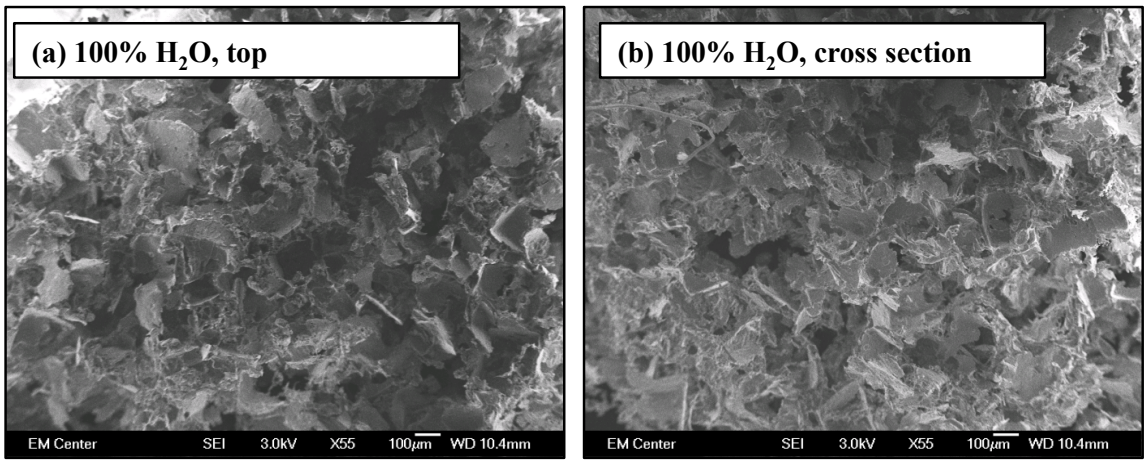


**Figure 8.6.** SEM images for scaffolds treated in a 100% $H_2O_{(g)}$ plasma. Images shown are representative of all plasma modified scaffolds discussed in this chapter.

**Table 8.2. XPS Elemental Composition of scaffolds treated in allylNH/allylOH plasmas[a]**

| Sample Position and Age | AllylNH in Feed (%)[b] | C (%) | O (%) | N (%) | O/C | N/C |
|---|---|---|---|---|---|---|
| Top Fresh | Untreated | 74.6 ± 0.7 | 25.4 ± 0.7 | 0 | 0.34 ± 0.01 | 0 |
| | 100 | 72.4 ± 1.8 | 8.9 ± 1.1 | 18.8 ± 0.8 | 0.12 ± 0.02 | 0.26 ± 0.02 |
| | 75 | 72.3 ± 0.6 | 10.0 ± 0.6 | 17.7 ± 1.3 | 0.14 ± 0.01 | 0.24 ± 0.02 |
| | 50 | 73.5 ± 0.07 | 16.9 ± 0.9 | 9.9 ± 0.5 | 0.23 ± 0.01 | 0.13 ± 0.001 |
| | 25 | 73.4 ± 1.6 | 21.0 ± 0.8 | 5.6 ± 0.7 | 0.29 ± 0.01 | 0.08 ± 0.01 |
| | 0 | 76.2 ± 0.2 | 23.9 ± 0.2 | 0 | 0.31 ± 0.004 | 0 |
| Cross Section Fresh | Untreated | 75.4 ± 0.9 | 24.6 ± 0.9 | 0 | 0.33 ± 0.02 | 0 |
| | 100 | 76.4 ± 0.4 | 19.3 ± 0.5 | 4.4 ± 0.9 | 0.29 ± 0.02 | 0.06 ± 0.01 |
| | 75 | 76.5 ± 0.3 | 19.1 ± 0.1 | 4.3 ± 0.1 | 0.25 ± 0.01 | 0.06 ± 0.002 |
| | 50 | 75.6 ± 0.9 | 22.6 ± 1.3 | 1.6 ± 0.4 | 0.25 ± 0.02 | 0.02 ± 0.004 |
| | 25 | 74.7 ± 2.4 | 24.1 ± 1.7 | 0.9 ± 0.07 | 0.32 ± 0.03 | 0.01 ± 0.002 |
| | 0 | 75.4 ± 0.7 | 24.7 ± 0.7 | 0 | 0.33 ± 0.01 | 0 |
| Top Aged 3 Weeks | 100 | 71.8 ± 0.1 | 16.1 ± 1.9 | 12.1 ± 2.0 | 0.22 ± 0.03 | 0.17 ± 0.03 |
| | 75 | 71.3 ± 0.7 | 14.2 ± 1.7 | 14.6 ± 1.1 | 0.20 ± 0.03 | 0.20 ± 0.01 |
| | 50 | 72.7 ± 0.6 | 18.8 ± 0.2 | 8.5 ± 0.7 | 0.26 ± 0.001 | 0.12 ± 0.02 |
| | 25 | 74.9 ± 0.9 | 20.7 ± 0.6 | 4.4 ± 0.5 | 0.30 ± 0.01 | 0.06 ± 0.01 |
| | 0 | 76.0 ± 0.9 | 24.0 ± 0.9 | 0 | 0.32 ± 0.02 | 0 |
| Cross Section Aged 3 Weeks | 100 | 74.2 ± 0.6 | 24.5 ± 1.4 | 1.3 ± 0.9 | 0.33 ± 0.02 | 0.02 ± 0.01 |
| | 75 | 75.4 ± 0.2 | 21.8 ± 0.4 | 2.9 ± 0.3 | 0.29 ± 0.01 | 0.04 ± 0.004 |
| | 50 | 74.2 ± 1.3 | 21.4 ± 0.8 | 4.3 ± 2.0 | 0.29 ± 0.01 | 0.06 ± 0.03 |
| | 25 | 77.0 ± 0.7 | 22.1 ± 1.0 | 0.9 ± 0.4 | 0.29 ± 0.02 | 0.01 ± 0.005 |
| | 0 | 76.8 ± 0.6 | 23.2 ± 0.6 | 0 | 0.30 ± 0.01 | 0 |

[a]Scaffolds were treated in allylNH/allylOH pulsed plasmas with $P$ = 50 W, d.c. = 5%, total pressure of 100 mTorr and treatment time of 15 min

[b]Remainder of feed gas composition was allylOH.

The most dramatic change occurs with the scaffold treated in the 100% allylNH system, as the oxygen content has dropped to <10% and the nitrogen content is nearly 20%. For the tops of all allylOH/allylNH plasma-treated scaffolds, the oxygen content is lower than that found in native PCL. The cross sections of the scaffold reveal a significantly different elemental composition than the external surface, with the oxygen content more closely resembling that of untreated PCL and having < 5% nitrogen incorporated, even with the 100% allylNH system.

Figure 8.7 shows O/C and N/C ratios for the tops of plasma treated scaffolds as a function of the allylNH content in the gas feed. For freshly treated scaffolds, the O/C ratios decrease linearly ($R^2$=0.94) as a function of the allylNH content in the gas feed for 0-75% allylNH plasmas and before stabilizing for 100% allylNH plasmas. This trend continues to be observed as the scaffolds age for 3 weeks. In contrast, the N/C ratio of the tops of freshly treated scaffolds treated in 0-75% allylNH plasmas increases linearly ($R^2$=0.98) as a function of allylNH in the gas feed before stabilizing for allylNH concentrations ≥75%. Based on these data, a maximum N/C ratio of ~0.25 is achieved on the top of the scaffolds using gas feed compositions of ≥75% allylNH.

The O/C and N/C ratios for the cross-sections of scaffolds treated in allylOH/allylNH plasmas are shown in Figure 8.8 as a function of allylNH in the gas feed. In sharp contrast to the external surface of the scaffolds, there are no distinct trends in the O/C and N/C ratios for the cross sections of aged scaffolds, and thus makes predicting the level of N incorporation throughout the scaffold network less straightforward. For freshly treated samples, the O/C of the cross sections for scaffolds treated in 100% allylOH (0% allylNH) and 25% allylNH plasmas are similar at ~0.32, Fig. 8.8a. As the allylNH content in the feed is increased to 50% and 75%, the O/C ratio drops to ~ 0.25 and then rises to ~ 0.29 for the scaffold treated in a 100% allylNH

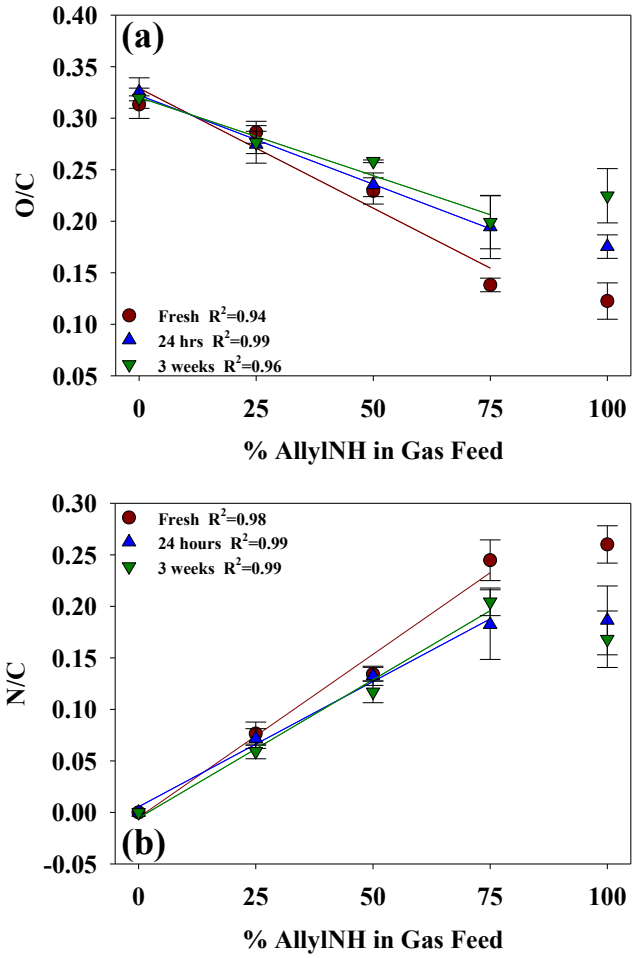


**Figure 8.7.** O/C and N/C content of the tops of scaffolds treated in allylOH/allylNH pulsed plasmas (50 W, 5% d.c., 100 mTorr) as a function of gas feed composition. The linear portion of the data were fit with a line of best fit and $R^2$ values are reported in the figure legend.

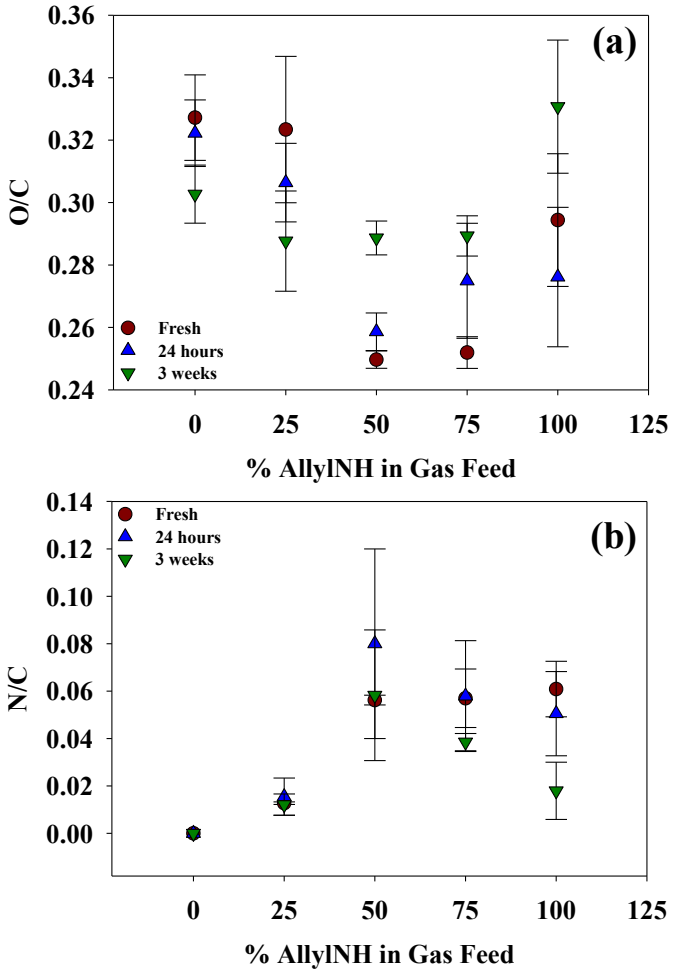


**Figure 8.8.** O/C and N/C content of the cross sections of scaffolds treated in allylOH/allylNH pulsed (50 W, 5% d.c., 100 mTorr) plasmas as a function of gas feed composition.

plasma. Within error, the scaffolds do not oxidize after 24 h of aging, but some do exhibit evidence of oxidation after 3 weeks, most notably for those treated with plasmas containing higher levels of allylNH. Upon aging for 3 weeks, the O/C ratio for scaffolds is the same, within experimental error, for all of the deposition systems. The N/C ratios in the cross-section of scaffolds treated in 25%, 50%, and 75% allylNH plasmas are the same within a given plasma system, Fig. 8.8b. Only a slight decrease in nitrogen content is observed for the cross sections of scaffolds treated in 100% allylNH plasmas and aged for 3 weeks.

One additional point with these data should be clarified. As mentioned in Chapter 7 and alluded to in section 8.2.1, cross-sectioning the scaffolds exposes a significant portion of the untreated bulk material. The relatively large error associated with the O/C and N/C elemental data for scaffold cross-sections presented in Figure 8.8 could result from variations in the contributions to the signal from the untreated polymer overlapping with signal from surfaces coated with deposited film. Furthermore, inconsistent deposition within the cross-section could also be a factor in these analyses. Indeed, Intranuovo and others[2,18,19] have theorized that lower N incorporation within a scaffold cross-section from plasma deposition processes could be the result of nonuniform film coatings caused by a lack of diffusion of gaseous species through the scaffolds' porous network.[1,2,4,9]

To further explore what surface functionalities are present on the scaffold, high-resolution $C_{1s}$ XPS data are shown in Figure 8.9a-c for scaffolds treated in allylOH/allylNH plasmas. Notable peaks in all three spectra include the large C-OH/C-OR binding environment at 286.5 eV and the –COOH peak at 289.1 eV, which occurs in all three spectra to a greater or lesser degree depending on the amount of allylOH in the feed gas. Binding environments in the 100% allylNH treated scaffold include a strong C-N/C=O peak at 286.0 eV, as well as an

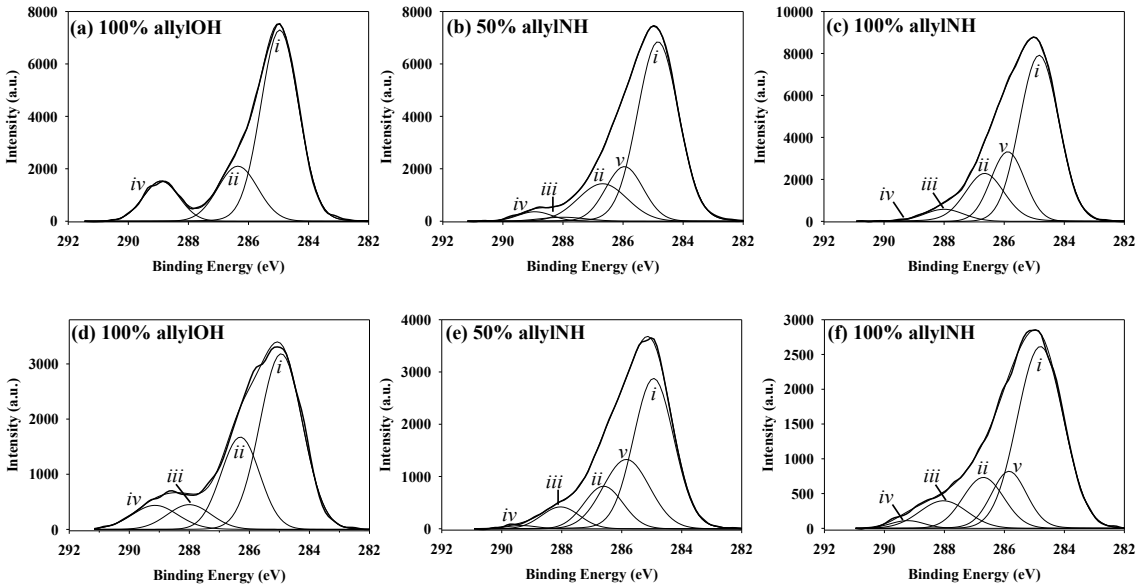


**Figure 8.9** High resolution $C_{1s}$ XPS spectra for freshly treated (a-c) PCL scaffolds and then aged 3 weeks (d-f) after plasma treatment in (a,d) 100% allylOH, (b,c) 50/50 mixtures of allylOH and allylNH, and (c,f) 100% allylNH pulsed plasmas (50 W, 5% d.c., 100 mTorr). The binding environments correspond to (*i*) C-C/C-H, (*ii*) C-OH/C-OR, (*iii*) C=O/N-C=O, (*iv*) O-C=O/ COOH, and (*v*) N-C/C-COOH

increase in the C-N/C=O peak at 288.0 eV. Markedly, the carboxyl binding environment is substantially reduced for scaffolds treated in 100% allylNH plasmas. It should be noted that the peaks located ~286.6 and ~289.1 eV likely contain contributions from the underlying PCL scaffold. Figure 8.9d-f contains high-resolution $C_{1s}$ XPS data for allylNH/allylOH plasma treated scaffolds and aged 3 weeks. Notable changes from freshly scaffolds include the reduction of the C-N peak for 100% allylNH treated scaffolds, and the increase in C-OR/C-OH environment for all of the plasma treated scaffolds, supporting the XPS compositional data that suggest oxidation of these materials occurs upon aging.

High resolution $N_{1s}$ XPS data for scaffolds treated in allylNH/OH plasmas are presented in Fig. 8.10 and analyzed similarly to Fig. 8.4. Scaffolds freshly treated in 100% (Fig. 8.10a) and 50% (Fig. 8.10c) allylNH plasmas contain ~85% N-C and ~15% N-C-O binding. Upon aging, the amount of N-C-O binding dramatically increases to ~57% for scaffolds treated in a 100% allylNH plasma, while the N-C-O binding only increases to ~38% for scaffolds treated in 50% allylNH plasmas. As outlined in Chapter 5, *pp*-allylNH oxidizes on Si substrates through a mechanism whereby oxygen is incorporated into the film's structure such that N-C-O functionality is formed. Thus, this data suggest that the allylNH films deposited on the PCL scaffolds undergo similar aging mechanisms. In contrast, the data presented in Section 8.2.1 indicate that the oxidation of the plasma modified scaffolds is primarily associated with the C-O environments rather than the N-C-O functionality.

The water absorption properties of the scaffolds were measured as a function of gas feed composition during plasma processing, Figure 8.11. Scaffolds freshly treated in 0% (100% allylOH) and 25% allylNH plasmas absorbed water at an initial rate of ~43 $\mu$L/s. Scaffolds treated in 50% allylNH plasmas have initial water absorption rates of ~12.5 $\mu$L/s, whereas

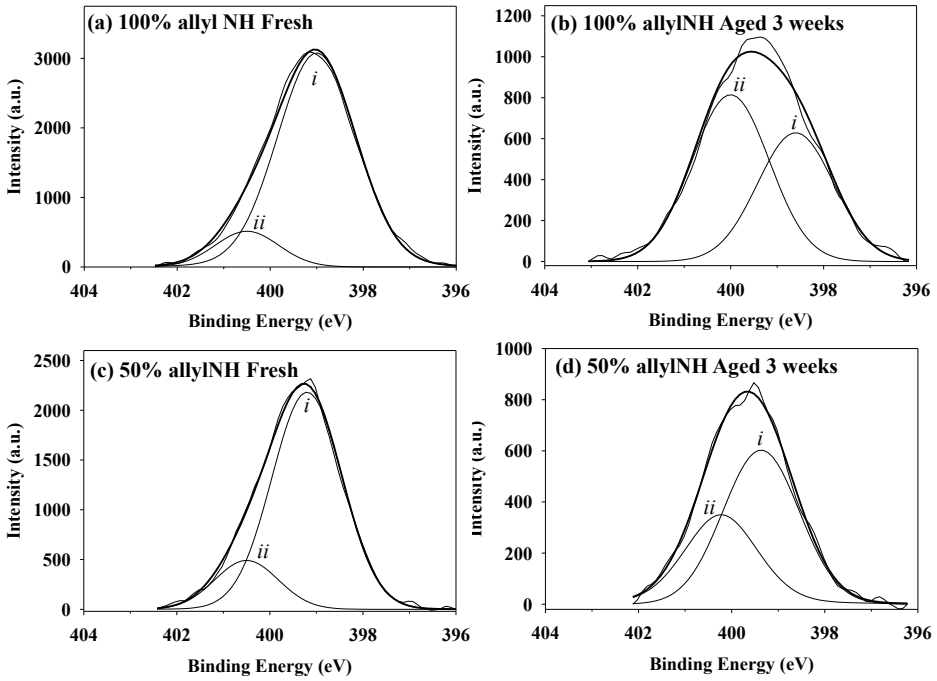


**Figure 8.10.** High-resolution $N_{1s}$ XPS data for scaffolds (a) freshly treated in 100% allylNH pulsed plasmas and then (b) aged 3 weeks; (c) freshly treated in 50/50% allylNH/allylOH plasmas and then (d) aged 3 weeks. Binding environments correspond to (*i*) N-C and (*ii*) N-C-O functionality. Scaffolds were treated in 50 W, 100 mTorr pulsed plasmas (5% d.c.) for 15 min.

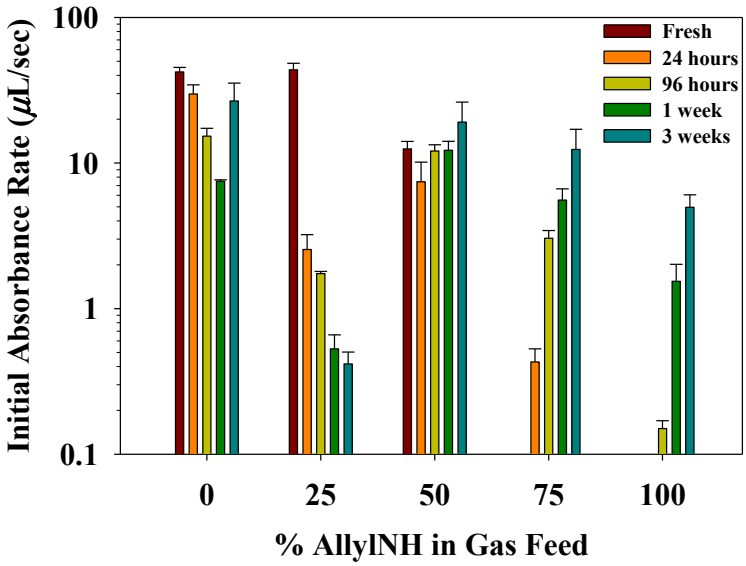


**Figure 8.11.** Initial water absorption rate as a function of allylNH in the gas feed for scaffolds freshly treated in allylOH/allylNH copolymerization systems. Data for freshly treated as well as scaffolds aged 1 day to 3 weeks after plasma treatment are shown.

scaffolds freshly treated in 75 and 100% allylNH plasmas did not absorb water. During the first 24 of aging, the absorption rate for scaffolds treated in 0, 25, and 50% allylNH plasmas decreased to ~29, 2.5, and 7.5 $\mu$L/s, respectively. After 96 hours, the absorption rate dropped to 15 and 1.5 $\mu$L/s for scaffolds treated in 0% and 25% allylOH plasmas, respectively, and the absorption rate increased to ~12 $\mu$L/s for scaffolds treated in a 50% allylNH plasma. Interestingly, after 4 hours, scaffolds treated in 75% allylNH plasmas began absorbing water at a relatively slow rate of 0.4 $\mu$L/s and rose to 3 $\mu$L/s after 96 hours of aging. Similarly, the absorption rate of scaffolds treated in a 100% allylNH plasma increased to 0.2 $\mu$L/sec after 96 hours. Scaffolds treated in 75% and 100% allylNH plasmas continued to increase in hydrophilicity and after 3 weeks of aging, all scaffolds exhibited absorption rates similar to or greater than those observed immediately after treatment using plasmas with lower concentrations of allylNH. The one exception to this comes from scaffolds treated in 25% allylNH plasmas, which consistently exhibited the highest initial absorption rates immediately after treatment.

It is not surprising that scaffolds treated in allylOH plasmas absorbed water immediately after plasma treatment, as literature and this dissertation show that *pp*-allylOH films exhibit hydrophilic wetting properties.[5,16,17,20] It is understandable then that copolymerized allylOH/allylNH films are also hydrophilic, regardless of sample age. More intriguing, however, is that the films deposited from high allylNH content plasmas actually become more hydrophilic as they age. As outlined in the literature, and discussed in Chapter 6, *pp*-allylNH films tend to incorporate oxygen in the form of alcohol functionality as the films age.[18,19] As these groups are more polar than the amine functionality contributed from the allylNH monomer, it follows that the films will become more hydrophilic as more alcohol groups are formed in the *pp*-allylNH network. The observation that this trend, observed for allylOH/allylNH films deposited on Si

wafers (Chapter 6) holds for films deposited on the 3D PCL scaffold substrates described here suggests that the underlying substrate does not significantly influence the deposition process.

Although the scaffolds treated under film deposition conditions have lower water absorption rates than those treated under surface modification (i.e. functional group implantation) conditions, the nitrogen content is significantly higher on the external surface and in the cross section of the scaffolds. Scaffolds treated under deposition conditions, however, had lower N incorporation in the cross section, which could prove problematic for cell growth applications.[5,20] Since Park and coworkers suggest that the N content plays a larger role in cell growth than wettability,[14,20] cell growth studies need to be conducted on the scaffolds to correlate functionality of the cross sections to cell colonization.

As with the surface modification studies, we also verified that the porous 3D structure of the scaffolds was not physically altered through plasma deposition. SEM images of the external surface and cross section of scaffolds treated in a 100% allylNH plasma are shown in Figure 8.12. As with the CW plasma treatments discussed in Chapter 6, the plasma treatment does not appreciably change the porous network of the scaffold, as the pores remain intact, which is true for scaffolds treated in all of the mixed-gas deposition systems.

These experiments show that the plasma deposition methods impart significantly more N onto the external surface of the scaffolds than the plasma modification methods, however there is still N incorporation throughout the scaffold interior. The 50% allylNH plasma systems have the most consistent water absorption properties, although they contain ~1% N in the interior. It is necessary that future research in this area include cell proliferation studies to determine the efficacy of these plasma treatments on cell growth and how it relates to the wettability and N content of the scaffold interior.

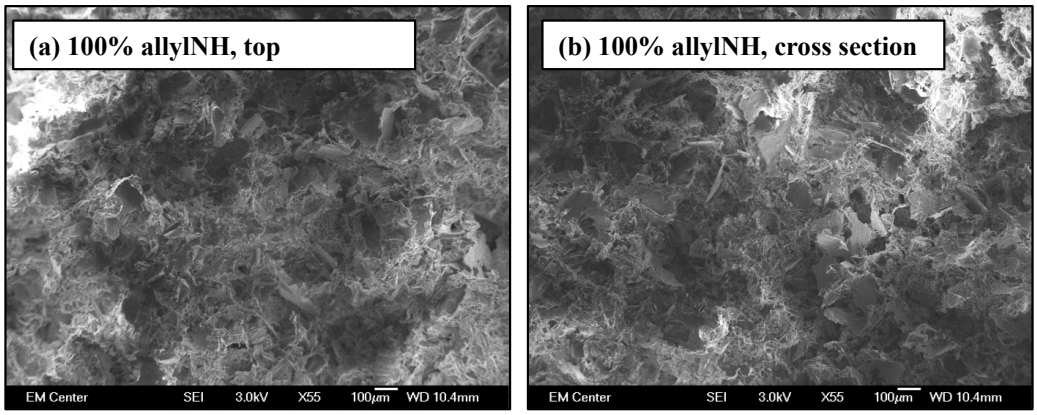


**Figure 8.12.** Scanning electron microscopy images for scaffolds treated in a 100% allylNH plasma. Images shown are representative of all plasma modified scaffolds discussed in this chapter.

## 8.3 Summary

This study reports on the plasma treatment of PCL polymeric scaffolds in non-depositing $NH_3/H_2O$ plasmas and in allylOH/allylNH copolymerization plasmas. Both systems successfully increased the oxygen and nitrogen functionality on both the external surface and throughout the cross section of the scaffolds. The plasma modification systems produced dramatically faster water absorption rates, especially immediately after plasma treatment. Interestingly, scaffolds treated in allylOH/allylNH deposition systems with high allylNH content initially had no or very low adsorption rates that ultimately increased substantially after 3 weeks. Although the work presented here clearly shows how the surface properties of the scaffolds can vary with plasma treatment, additional studies need to be conducted to determine individual contributions from surface chemistry, surface roughness, and water absorption characteristics.

REFERENCES


[1] F. Intranuovo, E. Sardella, R. Gristina, M. Nardulli, L. White, D. Howard, K. M. Shakesheff, M. R. Alexander, and P. Favia, Surface & Coatings Technology **205**, S548 (2011).

[2] F. Intranuovo, D. Howard, L. J. White, R. K. Johal, A. M. Ghaemmaghami, Pietro Favia, S. M. Howdle, K. M. Shakesheff, and M. R. Alexander, Acta Biomaterialia **7**, 3336 (2011).

[3] J. J. A. Barry, D. Howard, K. M. Shakesheff, S. M. Howdle, and M. R. Alexander, Adv. Mater. **18**, 1406 (2006).

[4] J. J. A. Barry, M. M. C. G. Silva, K. M. Shakesheff, S. M. Howdle, and M. R. Alexander, Adv. Funct. Mater. **15**, 1134 (2005).

[5] T. Jacobs, R. Morent, N. Geyter, P. Dubruel, and C. Leys, Plasma Chem Plasma Process **32**, 1039 (2012).

[6] M. L. Steen, A. C. Jordan, and E. R. Fisher, Journal of Membrane Science **204**, 341 (2002).

[7] K. R. Kull, M. L. Steen, and E. R. Fisher, Journal of Membrane Science **246**, 203 (2005).

[8] T. Pompe, K. Keller, G. Mothes, M. Nitschke, M. Teese, R. Zimmermann, and C. Werner, Biomaterials **28**, 28 (2007).

[9] R. Di Mundo, R. Gristina, E. Sardella, F. Intranuovo, M. Nardulli, A. Milella, F. Palumbo, R. d'Agostino, and P. Favia, Plasma Processes Polym. **7**, 212 (2010).

[10] N. M. Mackie, N. F. Dalleska, D. G. Castner, and E. R. Fisher, Chem. Mater. **9**, 349 (1997).

[11] C. Yen, H. He, Z. Fei, X. Zhang, L. J. Lee, and W. S. W. Ho, International Journal of Polymeric Materials **59**, 923 (2010).

[12] T. R. Gengenbach, X. Xie, R. C. Chatelier, and H. J. Griesser, Journal of Adhesion Science and Technology **8**, 305 (n.d.).

[13] E. D. Yildirim, R. Besunder, D. Pappas, F. Allen, S. Güçeri, and W. Sun, Biofabrication **2**, 014109 (2010).

[14] F. Renò, D. D'Angelo, G. Gottardi, M. Rizzi, D. Aragno, G. Piacenza, F. Cartasegna, M. Biasizzo, F. Trotta, and M. Cannas, Plasma Processes Polym. **9**, 491 (2012).

[15] F. Fally, C. Doneux, J. Riga, and J. J. Verbist, J. Appl. Polym. Sci. **56**, 597 (1995).

[16] J. C. Shearer and E. R. Fisher, Nanosci Nanotechnol Lett **4**, 358 (2013).

[17] V. Kearns, A. Mistry, S. Mason, Y. Krishna, C. Sheridan, R. Short, and R. L. Williams, J Mater Sci: Mater Med **23**, 2013 (2012).

[18] J.-C. Ruiz, A. St-Georges-Robillard, C. Thérésy, S. Lerouge, and M. R. Wertheimer, Plasma Processes Polym. **7**, 737 (2010).

[19] J. Friedrich, R. Mix, G. Kühn, I. Retzko, A. Schönhals, and W. Unger, Composite Interfaces **10**, 173 (2003).

[20] H. Park, J. W. Lee, K. E. Park, W. H. Park, and K. Y. Lee, Colloids and Surfaces B: Biointerfaces **77**, 90 (2010).

# CHAPTER 9

# RESEARCH SUMMARY AND PERSPECTIVES

Using plasma surface modification and plasma deposition strategies to enhance the functionality of biologically relevant surfaces is summarized here. Emphasis is placed on the applicability of this work to the broader plasma and biological communities. The chapter is concluded with thoughts on future directions of this work, particularly in the field of biomaterials.

## 9.1 Research Summary

Plasma processing methods have been used for several decades to deposit pinhole-free, highly functionalized films onto a variety of surfaces. In fact, the field of plasma processing is becoming a staple in the modification and fabrication of biomaterials because of its unique ability to implant functional groups, impart hydrophilicy, and deposit films on complex surfaces without appreciably changing the underlying material.[1] However, plasma processing is very sensitive to changes of any number of adjustable parameters. As such, it is necessary to independently study each unique plasma/substrate system to elucidate the details of each modification or deposition system. The research in this dissertation offers contributions to improved surface functionalization methods. Plasma modification and deposition systems were applied to new materials to create a range of surface functionalities. Furthermore, new plasma hardware was developed for the modification of 3D materials.

The overarching theme of this dissertation focuses on the functionalization of nanoparticles and 3D polymeric scaffolds using plasma processing methods. This problem was

approached by using $N_2$, $H_2O$, and $NH_3$ to graft oxygen and nitrogen containing functional groups on the surface of materials, and by using HMDSO, allylOH, allylNH, and HexylAm to deposit thin films on the surface of materials. A variety of surface analysis techniques were utilized to quantify changes in the surface properties of the resultant materials, namely XPS, FTIR, contact angle goniometry, and SEM. Plasma parameters were optimized to ensure a high level of functionalization.

Composite $TiO_2$ supported nanoparticle substrates were created by the plasma deposition of $SiO_2$ and HexAm thin films and the the dispersion properties of the new composite materials were examined with UV/vis spectroscopy. The plasma coated materials exhibited enhanced dispersion properties than uncoated materials. Composite $Fe_2O_3$ supported nanoparticles were created by the plasma deposition of allylOH thin films. The duty cycle of the plasma was adjusted such that OH-rich films were deposited. The gas-phase chemistry of the these allylOH plasmas was studied by AOES and showed that the initial decomposition products present in CW allylOH plasmas further decompose during the off cycle of pulsed plasmas before they are replenished by the next plasma pulse.

Although these supported nanoparticle substrates have specific applications in industries such as solar cell research, we extended our plasma deposition studies to individual nanoparticles. A rotating drum plasma reactor was designed to functionalize the surface of nanoparticles using plasma deposition methods. This reactor was specifically designed as an adaptation of current plasma hardware so that alternating between rotating and non-rotating experiments could be accomplished without much effort. Initial experiments showed that CW and pulsed allylOH plasmas behave similarly inside the rotating drum as they do in the standard tubular glass reactors in our lab. Therefore, extending known chemistries to nanoparticles in the

rotating reactor will be more straightforward. Furthermore, XPS and SEM analyses indicate that the majority of the nanoparticle surface is being coated with a *pp*-allylOH film, and thus being "encapsulated" with OH functionality.

Typically, single monomer plasma deposition techniques introduce a single type of functional groups. However, some applications might require a range of different surface functionalities.[1] Plasma copolymerization of allylOH and allylNH were used to deposit films containing alcohol, carboxyl, and amine functionality. The film composition was studied as a function of plasma gas-feed composition and sample age. The oxygen and nitrogen content of the films varied directly with the allylOH and allylNH content of the gas feed, respectively. The wettability of the films was found to be higher for copolymerized films deposited under pulsed plasma conditions.

The second major aspect of this work is focused on the surface modification of PCL scaffolds for the enhancement of cell growth. PCL scaffolds were treated with $N_2$ and $H_2O$ vapor plasmas in a translating electrode capactively coupled plasma reactor system. The nitrogen content within the scaffold increased with increasing $N_2$ in the gas feed, and scaffolds exhibited N incorporation throughout the scaffolds' porous network. Additionally, scaffolds retained their absorption properties throughout a one-week aging period. Enhanced Saos-2 osteoblast growth was observed for plasma treated scaffolds, independent of the plasma gas feed composition.

Nitrogen and oxygen functionality was also implanted on PCL scaffolds using $NH_3/H_2O$ plasma modification and allylOH and allylNH copolymerization systems. Both plasma systems successfully increased the functional group presence on scaffolds, implanting N and O functionality on both the external surface and in the cross sections. Although plasma

modification systems produced dramatically faster water absorption rates, scaffolds treated in allylOH/allylNH deposition systems had higher absorption rates after being aged for 3 weeks. Future investigations involving cell growth on these materials should yield valuable insight into the relationship between cell growth and surface chemistry.

## 9.2 Future Directions

The work discussed in this dissertation can be used to create biologically relevant surfaces for a variety of applications. Specifically, the design of the rotating drum plasma reactor will allow for the uniform treatment of polymeric scaffolds for cell growth experiments. The study of functional group implantation on these polymeric scaffolds has opened up substantial opportunities for research that will contribute to plasma processing and biomaterial literature. For example, cell growth mechanisms rely heavily on the surface charge of the substrate.[1] Chu and coworkers treated polymers with $NH_3$ plasmas and implanted amine and amide groups on the surface.[2] They theorized that the amine groups interact with acidic groups present on the surface of the cell membrane. As seen in this dissertation, the copolymerization of allylOH and allylNH on a scaffold's surface creates a range of chemistries which undoubtedly have a varying degree of surface charge, and could dramatically impact cell growth mechanisms.

To that end, our lab has extensively studied the surface charge of oxynitride surfaces on Si and determined that varying plasma parameters of $NH_3$ and $H_2O$ plasmas produce surfaces with different isoelectric points[3]. New instrumentation obtained by the Fisher labs will allow for straightforward calculations of surface charge. Since the film deposition on flat substrates is comparable to that on PCL scaffolds, data on flat substrates could be used to predict a relative measure of a scaffold's surface charge. Performing cell growth experiments on these

copolymerized systems would provide information about how surface charge, surface functionality, and surface wettability affect cell growth in copolymerized systems.

Extending our plasma treatments to a variety of other scaffold materials will also prove beneficial. For example, the fabrication of NO releasing materials has become very important in disease treatment and drug delivery, as NO deficiencies have been linked to a number of diseases.[4] While most of this work focuses on flat polymeric surfaces, Chen and Hezi-Yamit have extended this research to Teflon-like polymers functionalized with NO releasing functional groups.[5] Our lab could effectively create a Teflon-like scaffold by coating PCL scaffolds with thin films using known HFPO plasma chemistry.[6] NO releasing functional groups could then be implanted onto the Teflon coating, creating a multi-layer 3D material with a variety of properties.

The future directions of this work are far reaching. Having the ability to specifically tailor surface functionality dramatically improves the body of literature for biomaterial applications. Furthermore, conducting cell experiments will provide a real-time diagnostic on the effectiveness of specific plasma surface treatments on cell growth. Having a thorough body of literature on a variety of plasma processes on many different biologically relevant surfaces will undoubtedly advance biomaterials research. This dissertation has sought to offer efforts toward this end.

REFERENCES


[1] T. Jacobs, R. Morent, N. Geyter, P. Dubruel, and C. Leys, Plasma Chem Plasma Process **32**, 1039 (2012).

[2] C. F. Chu, A. Lu, M. Liszkowski, and R. Sipehia, Biochim. Biophys. Acta **1472**, 479 (1999).

[3] K. J. Trevino, J. C. Shearer, P. R. McCurdy, S. E. Pease-Dodson, C. C. Okegbe, and E. R. Fisher, Surf. Interface Anal. **43**, 1257 (2010).

[4] D. A. Riccio and M. H. Schoenfisch, Chem. Soc. Rev. **41**, 3731 (2012).

[5] M. Chen and A. Hezi-Yamit, WO Patent WO/2010/114,669 (2010).

[6] C. I. Butoi, N. M. Mackie, L. J. Gamble, D. G. Castner, J. Barnd, A. M. Miller, and E. R. Fisher, Chem. Mater. **12**, 2014 (2000).

# APPENDIX A

# INSTRUCTIONS FOR PREPARING POLYMERIC SCAFFOLDS

This appendix contains instructions for preparing the PCL scaffolds used for experiments in Chapters 7 and 8. The protocols were written by Eloisa Sardella and revised by Ellen R. Fisher and me.

## A.1 Creation of Polymer Solution

Mass 1 g of PCL pellets in a sealable container (e.g. specimen jar). Add 2.7 mL of chloroform (20/80 w/w) and reseal the container. *It is important to add the chloroform quickly as to minimize evaporation.* Seal the container tightly, wrapping with parafilm to ensure minimal evaporation of $CHCl_3$. Although the solution can be agitated to assist with dissolution of the PCL pellets, it is acceptable to allow it to sit for several hours or overnight to dissolve the PCL and form a clear, viscous solution. If solution is allowed to sit overnight, it should be stored in a refrigerator to minimize chloroform evaporation.

## A.2 Preparation of porogen

Sieve the porogen, (i.e. as-received sodium chloride), using three stainless steel fine test sieves, with aperture size diameters of 500 μm, 300 μm, and 150 μm (Sigma Aldrich). *The fine test sieves should be stacked with the largest diameter on the top and the smallest at the bottom to allow for simultaneous sieving of the porogen.* Any NaCl remaining in the 500 μm sieve (i.e. diameter >500 μm) can be ground with a mortar and pestle and re-sieved through the 500 μm sieve to achieve smaller crystal sizes. For 300-500 μm pore sizes, collect the material making it

through the top sieve (i.e. the 500 μm one), but remaining in the middle (the 300 μm sieve) one. For pore sizes ranging from 150 to 300 μm, collect the material passing through the middle sieve, but remaining in the bottom (i.e. the 150 μm sieve) one. Again, any material remaining in the 500 μm sieve can be reground in the mortar and then resieved to achieve smaller size crystals.

*Note: This step can be done while the PCL is dissolving in the chloroform, or done ahead of time and stored in containers labelled with the appropriate size distributions.*

### A.3 Creating and casting scaffold mixture

**Note: Read through this section carefully before beginning.** Working quickly, add the sieved porogen (NaCl) to the viscous PCL solution in a 5/95 w/w PCL/porogen ratio. For example, when using NaCl as a porogen, 19 g of NaCl should be used per 1 g PCL. To create a uniform polymer/salt blend, it is important to work as quickly as possible and to vigorously stir the mixture using a metal spatula/spoon to ensure an even distribution of salt throughout the polymer matrix. In general, the mixture will be very granular and sticky.

Once you have mixed the porogen thoroughly, cast into Teflon molds using a spoonula or spatula. In placing the material into the wells of each mold, it is important to get a uniform distribution and to ensure the holes are compactly filled. Thus, it is important to firmly press down vertically on each well and not scrape the material across the well. It is best to take small amounts of the polymer/salt blend out of the jar at a time, *being sure to reseal the jar each time*. For this part of the process, it is good to use a broad, flat spatula along with the one used to stir the mixture. It helps to use two utensils in tandem. You want to avoid scraping or placing additional material on top of already dried/drying material as both actions will ultimately create

incomplete or irregular constructs. Do not worry about excess material around the edges of the wells, as it can be useful as "tags" for pinching with tweezers during the removal process.

*Rinsing and Drying of Scaffolds* Air dry the filled Teflon molds 1 hour under the hood. Loosely cover the molds with a paper towel to prevent contaminants from falling onto the scaffolds. After drying for 1 hour, immerse the molds in absolute ethanol, for 3 hours, to allow phase separation and evaporation of the chloroform. At this stage, remove the scaffolds from the Teflon molds (or they can be left in the molds for the first stage of the leaching process). The leaching process involves soaking the constructs overnight in bidistilled water to leach out the porogen, ultimately forming a water-insoluble polymer foam. If the scaffolds are left in the molds for the first stage, they should be removed the following day. Removal from the molds entails the use of tweezers and care should be taken not to puncture or tear the constructs. Once removed from the mold, place the scaffolds in bidistilled water to continue the leaching process. Ideally, the water should be replaced 2-3 times daily, for a total of 2-3 days, to ensure complete leaching of the incorporated salt. It is not critical for the water to be changed every day as they have been allowed to sit in the same water over the course of an entire weekend, for example. Following the leaching process, the scaffolds were left to dry for 2 days and were then stored in a desiccator until ready for use.

# APPENDIX B

# PROTOCOLS FOR BIOLOGICAL EXPERIMENTS AND ANALYSES

This appendix contains cell splitting protocols and detailed procedures for samples preparation for the various biological analyses discussed in Chapters 6 and 7. The protocols were written by Roberto Gristina, Ellen R. Fisher, or me and edited by Ellen R. Fisher and me.

## B.1 Procedure for Splitting Cells

1. Wash hands w/soap and then ethanol (and/or put on gloves).
2. Warm media and PBS solution to 37° (take out of fridge – usually done first thing in the morning).
3. Turn on the hood. Turn the knob (with the key) two stages to the right, flip the middle switch and the switch on the far right, holding the latter one on until the light goes orange (sash goes up until it is ok), then flip the first switch back one notch.
4. Take trypsin out of the fridge. Trypsin should warm toward room temp at least 5-10 minutes before use.
5. Put everything you will need into the hood. This includes the following:
    a. Trypsin in rack (wash bottom of rack with ethanol before putting in hood).
    b. Centrifuge tube for cells
    c. PBS (wash bottom of container)
    d. Media (wash bottom of container)
    e. Pipette tips – small and large, glass and plastic disposable ones (1 mL and micro)
    f. Micropipetter and larger pipetter

g. Pipettes (5 mL and 10 mL)

6. You will also need a Pasteur pipette attached to the aspirator. Pipette tips are in the aluminum foil pouch in back left of hood (make sure the masking tape has black slashes indicating sterile). Turn the aspirator pump on.
7. To count the cells, you need to use the Thoma cellometer– a cell counting device (the Buerker is another one). The Thoma chamber must be cleaned with detergent, water, ethanol prior to use. The same must be done with the cover slip that will be used. Check for cleanliness under the microscope. Once the cover slip and the cellometer are clean, seal the cover slip on the cellometer using a small (~10 μL) of water along the edge of the grooved area. Cover slip should be located in the middle of the chamber, so that it covers both of the counting areas. Check for cleanliness again and choose the side of the device that is the cleanest. Be sure to arrange the Thoma cell such that you know which side you will be using for the counting.
8. Take flasks with cells out of the oven and aspirate the media off of the cells. Wash with ~4 mL of PBS. Aspirate again, removing all liquid. Wash each flask 2 or 3 times (we've been doing 2 times). **Note**: This is to wash away any extra proteins in the solution that the trypsin might consume preferentially to the proteins that attach the cells to the flask.
9. Put 1 mL of trypsin in each flask, making sure it goes everywhere on the flask. This works to detach the cells from the flask. Gently swish the solution around and then lightly bang on the flask to detach the cells. Check in microscope to see if cells are detached. If not, bang lightly again.
10. To stop the trypsin action on the cells and combine all cells together, place ~2 mL of media in each flask. With Flask 1, rinse the surfaces of the flask with a 5 mL pipette,

then collect all of the liquid and put it in Flask 2. Repeat the washing action and then collect all of the liquid and put it in Flask 3. At this stage, it is important to work quickly and to collect as much as possible. The next stage also includes a "wash", so it is not so important to be precise at this stage. Change pipette (to 10 mL); wash; put all of the liquid into a centrifuge tube. Alternatively, you can use a 10 mL pipette initially and then keep that one to transfer everything to the centrifuge tube.

11. To collect any remaining cells (important on last day before seeding scaffolds), with a new 5 mL pipette, take 3-4 mL of media (you need to check how much you can use, based on the total volume of the centrifuge tube—do not go above 15 mL of solution in centrifuge tube) and put it in Flask 1. Wash the flask using the pipette and then transfer everything to Flask 2. Repeat with Flask 2, washing and transferring liquid to Flask 3. Wash Flask 3 and then transfer everything to the centrifuge tube.
12. Turn the centrifuge on (rear, lower right). Put the centrifuge tube containing the cells in the centrifuge, using the appropriate counter weight tube (i.e. 13 mL of cell solution means you need a centrifuge tube with 13 mL in it). Close the lid, and check to make sure it is set for 1500 rpm and 5 min cycle (pressing the up arrow near the time readout will show the timing and speed). Adjust speed and time (and acceleration, far left readout) as needed using the up and down arrow buttons under each. Press the "play" button (right pointing triangle). Note that for Soas 2 cells, it is ok to run the centrifuge step twice if you are not ready for the cells. **Not true for other cell types**.
13. After the centrifuge step, take the tube out, aspirate the supernatant off of the cell pellet, leaving a small amount of the supernatant in the bottom of the tube. Add 1 mL of the medium with a glass pipette. Then use a μ-pipette tip to homogenize the cells into

solution. The aim is to create a homogeneous solution without creating too many bubbles in the solution.

14. Once the cellometer is ready (see step 7 above) and the cells are resolubilized into a homogeneous solution, take 10 μL of the cell solution and place it between the coverslip and the Thoma.
15. To count cells: Using the counter, count the number of cells appearing in the 16 space grid (4x4) on the Thoma cellometer. Take the number counted and multiply by $10^4$ and that is the number of cells per mL of cell solution. For example, on one of the days we counted, we counted ~215 cells in the grid. That means we had 215 x $10^4$ or 2.15 x $10^6$ cells/mL of solution. If you wanted to put 0.5 x $10^6$ cells/flask, then you would need to put ~230 μL of the cell solution into each flask [(0.5 x $10^6$ cells)/(2150 cells/μL)]. In calculating the number of cells you want to put into each flask, it is important to consider the number of days between passages. (e.g. 2 or 3). You do not want the cells to become overcrowded before you can split them again. Thus, you can always do an "extra" flask or two with a slightly lower number of cells if it is going to be a longer time between passages (i.e. 4 or 5 flasks instead of 3).
16. Flasks should be prepared that provide the following information: Passage number, date, cell type. (i.e. "Soas-2, III, 3 Oct 2012", where III is the passage number)
17. After deciding how many cells there are and how many cells you want in each flask, make sure you again have everything you need in the hood, including your prepared flasks. Put ~10 mL of media in each flask before you put the cells in. Once the flasks are prepared with the media, pipette the requisite amount of the cell solution (i.e. 230 μL in the above example – note we used a bit more just to be sure) into each of the flasks. Mix

cell solution a bit in the flask and put under the microscope to check to see if the cells are there.

### B.2 Conducting the MTT colorimetric assay

This procedure needs to be done in a fume hood. Gloves should be worn when handling MTT solubilization solution.

1. To prepare the 48-well plate for incubation, clearly label each row based on the experiment (i.e. $N_2$, $H_2O$, $N_2/H_2O$, untreated). You will have 3 scaffolds per experiment (for stats purposes).
2. For our experiment, we prepared 8 wells (3 without scaffolds, 3 with scaffolds, and 2 extra in case of a mistake).
3. In a centrifuge tube, place 500 $\mu$L of media *per well* that is being prepared. In our experiment, we placed 4 mL of media in the tube.
4. To the tube, place enough cell solution to yield 50,000 cells per well and mix thoroughly to homogenize cells in this new solution.
5. Dispense 500 $\mu$L of the new cell solution into 8 wells.
6. Place one scaffold each into 3 wells. Make sure that the scaffolds are orientated correctly (right side up – in our case the "top" as placed in the plasma reactor) in the wells.
7. At this stage, you should have:
    a. Wells 1-3: 1 scaffold + 500 $\mu$L of cell solution (prepared in step 4)
    b. Well 4 and 8: 500 $\mu$L of cell solution to be used as extra wells
    c. Well 5-7: 500 $\mu$L of cell solution to be used as control
8. Let the cells proliferate for 48 hours (or the time of your choosing) in an incubator.

After Incubation

1. In the 48-well plate, we have scaffolds we want to analyze after 48 hours of cell proliferation, and scaffolds we want to analyze after 5 days.
    a. For the scaffolds we are analyzing after 5 days
        i. In a sterile 48-well plate, place 500 $\mu$L of media into 3 wells. Transfer 3 scaffolds from the 48-hour aged plate to the new plate, and place back into incubator.
        ii. **NOTE:** Never micropipette directly out of media bottle. Transfer ~10 mL of media to a centrifuge tube with a 10 mL sterile pipet.
2. For scaffolds that we are testing today (after 48 hours of aging), put 500 $\mu$L of media into 4 new wells (3 will be for scaffolds, 1 for a control). The volume of media added should equal the volume of media that you initially added when preparing the well plate (step 3 in Section 1). Keep in mind that the total volume of each well is 1 mL.
3. To this, add 50 $\mu$L (**10% of the media volume**) of MTT solution and then mix thoroughly with a 1 mL micropipette tip.
4. Transfer scaffolds to 3 of the new wells, making sure that you keep the scaffolds right side up.
5. Aspirate the remaining solution out of the wells where the scaffolds were, and add 50 $\mu$L of MTT solution + 500 mL of media and mix.
6. At this point, you should have:
    a. Wells 1-3 (where the scaffolds originated): 50 $\mu$L of MTT solution + remaining solution after scaffolds were removed

b. Wells 4-6 (where the scaffolds are now): 50 $\mu$L of MTT solution + 500 $\mu$L of media

c. Well 7 (control): 50 $\mu$L of MTT solution + 500 $\mu$L of media.

7. Put plate back into oven and let incubate for 2-4 hours. During this incubation, the mitochondria within the cells will reduce the MTT solution to formazan crystals, creating a purple color that can be analyzed with a spectrophotometer. The cells will appear dark black (color is from formazan) when viewed under a transmission optical microscope.
8. Turn spectrophotometer on and allow to warm for ~10 mins.
9. While the spectrophotometer is warming up, dissolve the formazan crystals.
    a. Add 500 $\mu$L of MTT solubilization solution in wells 4-7 (you can also add this to wells 1-3, but in theory there should not be cells in these wells) and mix, not disposing of your pipette tips.
    b. The solution should turn from a light yellow color to a darker green color as the formazan is dissolving. You need to be more rigorous when mixing so that all of the formazen is dissolved.
    c. Transfer the solutions to cuvettes for analysis.
10. Spectrophotometric analysis will occur at two different wavelengths: 570 nm and 690 nm. The formazen absorbs at 570 nm, and other background material absorbs at 690 nm, so the difference in absorbances should yield the absorbance of formazen. (i.e. $A_{690}$-$A_{570}$ = $A_{formazin}$)

### B.3. Preparation of Scaffolds for Fluorescence Microscopy using Alexa Fluor 546 Phallodin Dye

1. Scaffolds should be in PFA solution at 4 $^{\circ}$C.

2. Aspirate PFA solution out of the wells, then wash scaffolds with PBS 4-5 times. Be careful when washing (i.e. be sure to pipette the PFA onto the walls of each well and not directly on the scaffold) to avoid cell disturbance.
3. Once scaffolds are washed, cover each scaffold with Triton-X solution and let sit for 20 minutes. This is known as the "permeation step", and although the exact mechanism is unknown, the Triton-X is theorized to create micropores in the cell membrane so that the dye can penetrate the cell wall and enter the cell.
4. After 20 minutes, aspirate the Triton-X out of the wells, and wash with PBS 4-5 times.
5. *For the following steps, always work in the lowest light possible to avoid photobleaching of the dye.*
6. Mix a 1:10 solution of Alexa Fluor 546 to PBS. This is expensive, so use as little as possible. For each scaffold, you just need enough solution to cover. So, in each well, you will have a solution of 5 $\mu$L dye and 500 $\mu$L PBS (*1:10*). For large quantities, mix in a centrifuge tube before pipetting into well tray. It is important to rinse the pipette tip used for the dye with the PBS solution a few times to ensure that all dye made it into the PBS.
7. Let the scaffolds soak in the PBS/dye solution for ~35 min. Be sure to cover the well trays with Al foil to ensure a dark environment. Let this stand at room temp.
8. Aspirate the PBS/dye solution out of the wells, and rinse with PBS 2-3 times. Fill the wells with PBS (enough to cover scaffolds). When not in use, the scaffolds should be stored at 4 $^{\circ}$C to prevent rapid degradation of the dye.

## B.4. Staining Cells on Flat Substrates with Coomassie Blue for Optical Transmission Microscopy

1. At the beginning of this procedure, cells should be growing in Petri dishes.
2. Take Petri dishes out of the oven and aspirate media out of the dishes.
3. Add enough PFA (4% in PBS solution) to cover the surface, and wait for 20 min (or up to 10 days) while the PFA fixes the cells (i.e. kills the cells and "freezes them in time").
4. Aspirate the PFA out of the Petri dishes and wash 2 times with PBS.
5. Add just enough Coomassie Blue to cover the bottom of the Petri dish and stain for 3 min.
6. Aspirate solution out of dishes and wash with PBS until wash solution is clear.
7. Using a transmission optical microscope, image cells. Make sure you are *not* in phase contrast mode.

# LIST OF ABBREVIATIONS

| | |
|---|---|
| allylNH | allyl amine |
| allylOH | allyl alcohol |
| AOES | actinometric optical emission spectroscopy |
| CA | contact angle goniometry |
| CCP(s) | capacitively coupled plasma(s) |
| CW | continuous wave |
| d.c. | duty cycle |
| DI | deionized |
| fnp(s) | free, unsupported nanoparticle(s) |
| FTIR | Fourier-transform infrared spectroscopy |
| HexAm | hexylamine |
| HMDSO | hexamethyldisiloxane |
| ICP(s) | inductively coupled plasma(s) |
| OES | optical emission spectroscopy |
| np(s) | nanoparticle(s) |
| $P$ | power |
| *Pp* | plasma polymerized |
| $P_T$ | total system pressure |
| PCL | polycaprolactone |
| PECVD | plasma enhanced chemical vapor deposition |
| *pp* | plasma polymerized |
| rf | radio frequency |

| | |
|---|---|
| SEM | scanning electron microscopy |
| $T_S$ | substrate temperature |
| UV/vis | ultraviolet/visible spectroscopy |
| WCA(s) | water contact angle(s) |
| XPS | x-ray photoelectron spectroscopy |